HISTOTRIPSY FOR PEDIATRIC CARDIAC APPLICATIONS

by

Ryan M. Miller

A dissertation submitted in partial fulfillment
of the requirements of the degree of
Doctor of Philosophy
(Biomedical Engineering)
in the University of Michigan
2014

Doctoral Committee:

Assistant Professor Zhen Xu, Co-Chair
Assistant Professor Gabe E. Owens, Co-Chair
Professor Charles A. Cain
Professor J. Brian Fowlkes
Assistant Research Scientist Timothy L. Hall

Dedication

To my wife, Mary Ann

Acknowledgement

First and foremost, I would like to express my sincere gratitude to my advisor and mentor, Dr. Zhen Xu, for her gracious support and guidance through my time in graduate school. I feel very fortunate for her to have taken me on as her student, as I consider her patience and knowledge to have been essential to my reaching this point. I would also like to thank Drs. Gabe Owens, Charles Cain, Brian Fowlkes, and Timothy Hall, for their insight, guidance, and assistance. It has always been a comfort knowing the depth and breadth of knowledge and experience I have available to me through you all. It has been an unexpected joy to have worked for such genuinely kind and helpful people.

I would also like to thank the current and former members of the Histotripsy lab, including Dr. Adam Maxwell, Dr. Tzu-Yin Wang, Dr. Yohan Kim, Dr. Kuang-Wei Lin, Dr. Jonathan Sukovich, Eli Vlaisavljevich, Xi Zhang, Alex Duryea, Steven Allen, Simone Park, Hedieh Tamaddoni, and Yige Li. I would like to especially thank Yohan, who joined the lab on the same day that I did so many years ago. He has always been the first person I ask any question, and as a result has taught me a great many things about hydrophones, transducer design, amplifiers, and more. I would like to thank Adam as well, your knowledge and understanding of acoustics and cavitation was a great help to me. Eli has always been a pleasure to work with, and your knowledge of biology and physiology has been a terrific resource. I'd like to thank Tzu-Yin for her help with the Verasonics, tissue preparation, and histology processing. Xi, your help with the Doppler project will always be appreciated. Kuang-Wei, Alex, Jonathan, Steven, Simone,

Hedieh, and Yige, thank you all for never being too busy for a question and for being a part of the friendly, helpful group dynamic that I have enjoyed all these years.

I wish to thank my colleagues in Radiology and Urology, Drs. Kimberly Ives, Oliver Kripfgans, and William Roberts. Kim, thank you particularly for your help in all the animal experiments, your pleasant company and assistance was a terrific help. Oliver, thank you for sharing your wonderful camera and machine shop with me.

Last, but certainly not least, I would like to thank my family. I could never express in just a few words what you all mean to me, but a few simple thank you's will hopefully convey a small part of it. To my wife, Mary Ann, thank you for supporting me in all my choices, it hasn't been easy but we're getting there. Dad, thank you for everything, I've always known I could do great things because of the potential you saw in me. Mom, your kindness and love are with me always. JoAnn, your support and assistance have been wonderful, thank you so much. To all my siblings, thank you for all the support and encouragement, you all inspire me with your hard work and accomplishments. And finally, my babies! Jacob and Allison, you bring so much happiness to my life, you make it all worthwhile.

Ann Arbor, Michigan

March, 2014

Table of Contents

List of Figures

List of Tables

Abstract

Medicine continues to move towards less invasive techniques for many cardiac conditions, especially for high-risk patients that may not tolerate the alternative, more invasive approach. For instance, patients born with the congenital heart defect hypoplastic left heart syndrome often require emergent creation of a perforation through the atrial septum for survival prior to palliative surgery. However, most approaches are catheter based, still invasive, and continue to have significant challenges, limitations, and complications. A completely non-invasive technique such as histotripsy may provide the same result in a faster, safer, and more efficient manner. Using high-pressure ultrasound pulses applied outside the body and focused to the targeted tissue, histotripsy generates a cluster of micro-bubbles and the energetic growth and collapse of these micro-bubbles results in fractionation of the target tissue. Histotripsy has been demonstrated successful for non-invasive tissue fractionation in various organs. The goal of this work is to investigate the safety and efficacy of histotripsy for neonatal cardiac applications. To aid in this goal, therapy guidance and monitoring techniques are developed, and an integrated histotripsy therapy system, optimized for the human neonate with congenital heart disease, was designed and constructed.

In this dissertation, histotripsy is first demonstrated to be capable of generating targeted intra-cardiac communications when positioned outside the body in an intact neonatal animal model with minimal collateral damage or systemic side-effects. Moreover, further study showed no intermediate-term clinical, pathologic, and systemic effects of these intra-cardiac

communications created by histotripsy. Second, to mitigate the possibility of unintended injury due to heart motion, real-time motion correction using ultrasound imaging is developed and integrated into a histotripsy therapy system. This motion correction is developed specifically for the high-speed motions present in a beating heart. The performance of the motion correction is quantified *in vitro* and a validated in a single *in vivo* experiment. Third, to maximize therapy efficacy, novel bubble-induced color Doppler feedback is developed to monitor the degree of tissue damage during histotripsy treatment. Strong correlations existed between the quantitative metrics derived from the bubble-induced color Doppler and the degree of tissue fractionation as examined with histology, demonstrating the feasibility of using this technique as quantitative, real-time feedback for histotripsy treatments. Finally, a histotripsy therapy transducer with appropriate physical dimensions and acoustic parameters to precisely ablate cardiac tissue non-invasively in a human neonate is developed and integrated into an ultrasound guided histotripsy therapy system. The data and the integrated system accomplished from this dissertation form the essential foundation to a pioneering clinical trial for histotripsy cardiac therapy in infants, which will position histotripsy for application on a broad range of cardiac disorders in patients of all ages.

Chapter 1
Introduction

The main goal of this study is to develop an ultrasound image guided histotripsy system optimized for safe and effective neonatal cardiac intervention. The safety and effectiveness of cardiac histotripsy will be demonstrated in a live animal model. To aid in this goal, therapy guidance and monitoring techniques are developed in parallel. These techniques are: (1) a real-time motion correction system to lock the therapy focus onto the intended target as it is displaced by both cardiac and respiratory motion and (2) a method to capture real-time Doppler information during therapy to monitor and assess therapy progression. Finally, a histotripsy therapy transducer with appropriate physical dimensions and acoustic parameters to precisely ablate cardiac tissue non-invasively in a human neonate is developed and integrated into a complete ultrasound guided histotripsy therapy system. We anticipate that these studies will lead to the first clinical trial for histotripsy cardiac therapy in infants, positioning histotripsy to transform non-invasive therapy for a broad range of cardiac disorders in patients of all ages. Some examples of potential cardiac applications include: de-bulking obstructive tissues like those found in patients with Hypertrophic Cardiomyopathy (HCM), the induction of coronary artery thrombolysis, and the ablation of cardiac arrhythmias. This would effectively revolutionize the clinical arsenal available for cardiac intervention, which is the ultimate goal of this line of research.

This chapter will first give a brief overview of histotripsy therapy and its application on cardiac tissues. This will be followed by an overview of the targeted clinical application of this work, the non-invasive creation of an atrial septal defect (ASD) in neonatal patients born with the congenital heart defect hypoplastic left heart syndrome (HLHS). The significance of this work will then be discussed, specifically the broad range of cardiac disorders with treatments that could potentially be enabled by this research. This chapter will then be concluded with an outline of the dissertation, including an overview of each chapter.

1.1 Histotripsy Therapy

Histotripsy is a form of cavitation-based ultrasound therapy that precisely fractionates and removes tissue [1-3], which can be used as a non-invasive alternative to the surgical removal of unwanted tissue for high-risk surgical patients with a wide variety of cardiac conditions. Histotripsy produces and controls a dense cluster of cavitation micro-bubbles ("bubble cloud") [4-6] using specific ultrasound pulse sequences [7-9] to create pressures that exceed the cavitation threshold [10], causing mechanical cellular disruption at the focus [1-3, 11]. The process is typically guided and monitored in real-time using ultrasound imaging [2, 12], and has been shown capable of creating an ASD *in vivo* [13].

Extra-cardiac high intensity focused ultrasound (HIFU) has previously been used to generate thermal lesions to treat arrhythmia, where the HIFU transducer is placed directly outside the heart wall to produce lesions in cardiac tissue [14-16]. For example, the Epicor Cardiac Ablation System has been demonstrated to be a less invasive and effective alternative to treat human patients with atrial fibrillation (AF) [14, 17]. However, currently there are no

completely non-invasive techniques, apart from pharmacotherapy, for the treatment of congenital or acquired heart disease.

Unlike HIFU thermal therapy, histotripsy precisely produces and controls a cavitation bubble cloud to fractionate tissue to liquid-appearing acellular homogenate [1, 18], which can be reabsorbed and eliminated by the body to achieve effective tissue remodeling and removal [11-13]. Using microsecond long, high amplitude, shockwave ultrasound pulses separated by long intervals, cavitation bubble dynamics are controlled, while thermal injury to surrounding and intervening tissue can be avoided [7]. As bubbles are readily detected acoustically, the entire process is monitored and guided by real-time ultrasound imaging. In comparison to thermal therapy, histotripsy is more resistant to the aberration effect from bone and can be used to generate precise lesions through bone obstructions and over long intervening tissue paths [19]. A non-invasive approach like histotripsy has the potential to not only eliminate the risks and complications associated with conventional cardiopulmonary bypass, cardiac surgery and invasive catheterization but also improve overall outcome by providing a new clinical tool with unique applications. From the fetus to the adult, non-invasive tissue perforation, discrete lesion creation, and/or bulk tissue removal would be revolutionary and transform clinical care for cardiac diseases.

1.2 Targeted Clinical Application

Medicine continues to move towards less invasive techniques for many cardiac conditions, especially for high-risk patients that may not tolerate the alternative, more invasive approach. However, most approaches are catheter based, still invasive, and continue to have significant challenges, limitations, and complications. A completely non-invasive technique

such as histotripsy may provide the same result in a faster, safer, and more efficient manner. For instance, patients born with HLHS and an intact atrial septum require emergent creation of a perforation through the atrial septum (ASD) for survival prior to palliative surgery, and have increased risk (mortality 50-80%) compared to those born with an ASD [20-22]. Unfortunately, secondary to anatomic considerations and hemodynamic instability, current procedures are associated with very high morbidity and mortality, creating a clinical need for an entirely non-invasive approach [21-23]. This high-risk population is well suited to establish the safety and therapeutic efficacy of histotripsy for cardiac applications.

Current approaches to ASD creation in this patient group are fraught with challenges, limitations, and complications dictated by the clinical instability of these patients and their complicated anatomy (i.e. thick atrial septum and small left atrium), hence revealing a clinical need for an alternative approach [21, 24]. Because it permanently removes tissue, does not require vascular access (limits risk of infection, etc.) or fluoroscopy, and could potentially be done at the bedside, histotripsy would provide safer and timelier therapy thereby improving outcomes. Based on this unmet clinical need, the overwhelming enthusiasm of this application within the Pediatric Cardiology community, and an optimal subcostal acoustic window (free of rib obstruction to a relatively immobile atrial septum) [13], we will first prepare histotripsy for non-invasive ASD creation in patients with HLHS. Since the patient population is small and very high risk, histotripsy will qualify for designation as a Humanitarian Use Device making progression through external and internal regulatory approval and eventually into clinical use more efficiently and timely, especially compared to other applications.

1.3 Clinical Significance and Implications

Once the clinical efficacy and safety of the technique are demonstrated in this initial pediatric population, the applications of histotripsy can be broadened through the technical advancements developed here to numerous other cardiac conditions in children and adults, validating it as an innovative clinical resource. There are a number of common cardiac conditions in which ultrasound-mediated tissue removal or remodeling may have important applications. Below are just a few diseases that may benefit from histotripsy therapy.

Patients with hypertrophic cardiomyopathy (HCM), a condition that affects 1 in 500 adults, often have significant obstruction below the aortic valve caused by excess muscle [25-29]. For patients deemed poor operative candidates due to other cardiac or non-cardiac conditions, alcohol septal ablation (which requires an infusion of alcohol into the coronary artery to create a septal infarction) [25, 30] has been used to remodel the tissue and relieve obstruction. Unfortunately, this less invasive approach has a relatively high frequency of serious complications including coronary artery perforation, complete heart block and ventricular arrhythmias [31, 32]. Non-invasive removal of tissue using histotripsy may prove to be a substantial advance for HCM patients who are poor candidates for surgery.

Atrial fibrillation (AF) is a common condition affecting nearly 2 million people in the US [33-35]. Catheter-based procedures such as radiofrequency-mediated isolation of the pulmonary veins are associated with significant risk of atrial perforation or pulmonary venous obstruction [36]. Concurrent visualization and tissue modification using histotripsy may lead to comparable rates of success with lower risk of complications.

Pulmonary hypertension (PHTN) is a less common but devastating condition that consists of high blood pressure in the lungs and failure of the right side of the heart. Despite improved

medical therapy some patients progress to need either lung transplantation (a high risk procedure with poor survival), or ASD creation (which can help maintain cardiac output and improve symptoms but has a significant surgical risk) [37, 38]. In this high-risk patient group, non-invasive creation of a permanent ASD using histotripsy may be a low-risk, non-invasive way to significantly improve symptoms. A non-invasive approach to create an ASD also has important implications for another congenital heart condition, d-transposition of the great arteries (d-TGA) [39-41]. This condition often requires augmented mixing of blood at the atrial level (through the creation or enlargement of an ASD) prior to surgical repair. Furthermore, creation of new intra-cardiac pathways in the developing fetus has exciting potential to lessen the severity of selected severe congenital cardiac defects such as HLHS. Current invasive approaches have had success in creating new pathways and modifying disease severity but are associated with a high risk of fetal demise [24, 42, 43].

1.4 Outline of this Dissertation

This dissertation is organized in seven chapters to establish and improve the safety and efficacy of histotripsy for pediatric cardiac applications.

Chapter 1 introduces histotripsy and its potential to become a transformative treatment option for a broad range of cardiac disorders. Specifically, it establishes the objective of this dissertation, to develop an ultrasound image guided histotripsy system optimized for safe and effective neonatal cardiac intervention in patients with HLHS.

Chapter 2 investigates the potential of histotripsy to generate targeted intra-cardiac communications when positioned outside the body in an intact neonatal animal model to

establish the feasibility of this technique to create similar lesions in human neonates with congenital heart disease.

Chapter 3 expands on this to determine the intermediate-term clinical, pathologic, and systemic effects of these intra-cardiac communications created by histotripsy in an intact neonatal animal model in an effort to address the safety profile of this technique as we continue to advance histotripsy toward clinical application for congenital heart disease.

Chapter 4 presents a histotripsy-based cardiac therapy system integrated with real-time 1D motion correction and treatment monitoring using ultrasound imaging. This motion correction is developed specifically for the high-speed motions present in a beating heart. The performance of the motion correction is quantified *in vitro* and a validated in a single *in vivo* experiment.

Chapter 5 investigates potential therapy progress feedback metrics gathered from precisely timed color Doppler velocity measurements of the focal region immediately following histotripsy pulses. The correlation to the fractionation progress is established *in vitro* using tissue mimicking phantoms and *ex vivo* porcine liver tissue.

Chapter 6 details the development of a histotripsy therapy transducer optimized for the pediatric cardiac application. The integration of this transducer into a complete ultrasound guided histotripsy therapy system is then detailed and a finished, functional prototype is presented.

Chapter 7 summarizes the findings and contributions of this dissertation, and discusses the future work necessary to transition the project into the first clinical trial for non-invasive ASD creation in neonatal patients with congenital heart disease.

1.5 References

[1] J. E. Parsons, C. A. Cain, G. D. Abrams, and J. B. Fowlkes, "Pulsed Cavitational Ultrasound Therapy For Controlled Tissue Homogenization," *Ultrasound in Medicine and Biology,* vol. 32, pp. 115-129, January 2006.

[2] W. W. Roberts, T. L. Hall, K. Ives, J. S. Wolf, Jr, J. B. Fowlkes, and C. A. Cain, "Pulsed Cavitational Ultrasound: A Noninvasive Technology for Controlled Tissue Ablation (Histotripsy) in the Rabbit Kidney," *The Journal of Urology,* vol. 175, pp. 734-738, February 2006.

[3] Z. Xu, A. Ludomirsky, L. Y. Eun, T. L. Hall, B. C. Tran, J. B. Fowlkes, and C. A. Cain, "Controlled Ultrasound Tissue Erosion," *IEEE Transactions on Ultrasonics, Ferroelectrics, and Frequency Control,* vol. 51, pp. 726-736, June 2004.

[4] Z. Xu, J. B. Fowlkes, E. D. Rothman, A. M. Levin, and C. A. Cain, "Controlled ultrasound tissue erosion: The role of dynamic interaction between insonation and microbubble activity," *The Journal of the Acoustical Society of America,* vol. 117, pp. 424-435, 2005.

[5] Z. Xu, M. Raghavan, T. L. Hall, C.-W. Chang, M.-A. Mycek, J. B. Fowlkes, and C. A. Cain, "High Speed Imaging of Bubble Clouds Generated in Pulsed Ultrasound Cavitational Therapy—Histotripsy," *IEEE Transactions on Ultrasonics, Ferroelectrics, and Frequency Control,* vol. 54, pp. 2091-2101, October 2007.

[6] Z. Xu, M. Raghavan, T. L. Hall, M.-A. Mycek, J. B. Fowlkes, and C. A. Cain, "Evolution of Bubble Clouds Induced by Pulsed Cavitational Ultrasound Therapy—Histotripsy," *IEEE Transactions on Ultrasonics, Ferroelectrics, and Frequency Control,* vol. 55, pp. 1122-1132, May 2008.

[7] K. Kieran, T. L. Hall, J. E. Parsons, J. S. Wolf, Jr, J. B. Fowlkes, C. A. Cain, and W. W. Roberts, "Refining Histotripsy: Defining the Parameter Space for the Creation of Nonthermal Lesions With High Intensity, Pulsed Focused Ultrasound of the In Vitro Kidney," *The Journal of Urology,* vol. 178, pp. 672-676, August 2007.

[8] Z. Xu, J. B. Fowlkes, and C. A. Cain, "A New Strategy to Enhance Cavitational Tissue Erosion Using a High-Intensity, Initiating Sequence," *IEEE Transactions on Ultrasonics, Ferroelectrics, and Frequency Control,* vol. 53, pp. 1412-1424, August 2006.

[9] Z. Xu, T. L. Hall, J. B. Fowlkes, and C. A. Cain, "Effects of Acoustic Parameters on Bubble Cloud Dynamics in Ultrasound Tissue Erosion (Histotripsy)," *The Journal of the Acoustical Society of America,* vol. 122, pp. 229-236, July 2007.

[10] Z. Xu, J. B. Fowlkes, A. Ludomirsky, and C. A. Cain, "Investigation of Intensity Threshold for Ultrasound Tissue Erosion," *Ultrasound in Medicine and Biology,* vol. 31, pp. 1673-1682, December 2005.

[11] T. L. Hall, K. Kieran, K. Ives, J. B. Fowlkes, C. A. Cain, and W. W. Roberts, "Histotripsy of Rabbit Renal Tissue In Vivo: Temporal Histologic Trends," *Journal of Endourology,* vol. 21, pp. 1159-1166, October 2007.

[12] T. L. Hall, J. B. Fowlkes, and C. A. Cain, "A Real-Time Measure of Cavitation Induced Tissue Disruption by Ultrasound Imaging Backscatter Reduction," *IEEE Transactions on Ultrasonics, Ferroelectrics, and Frequency Control,* vol. 54, pp. 569-575, March 2007.

[13] Z. Xu, G. Owens, D. Gordon, C. A. Cain, and A. Ludomirsky, "Noninvasive Creation of an Atrial Septal Defect by Histotripsy in a Canine Model," *Circulation,* vol. 121, pp. 742-749, February 2010.

[14] J. Ninet, X. Roques, R. Seitelberger, C. Deville, J. L. Pomar, J. Robin, O. Jegaden, F. Wllens, E. Wolner, C. Vedrinne, R. Gottardi, J. Orrit, M.-A. Billes, D. A. Hoffmann, J. L. Cox, and G. L. Champsaur, "Surgical Ablation of Atrial Fibrillation with Off-Pump, Epicardial, High-Intensity Focused Ultrasound: Results of a Multicenter Trial," *The Journal of Thoracic and Cardiovascular Surgery,* vol. 130, pp. 803.e1-803.e8, September 2005.

[15] R. Otsuka, K. Fujikura, Y. Abe, K. Okajima, T. Pulerwitz, D. J. Engel, R. Muratore, J. A. Ketterling, A. Kalisz, R. Sciacca, C. Marboe, G. Yi, J. Wang, and S. Homma, "Extracardiac Ablation of the Left Ventricular Septum in Beating Canine Hearts Using High-Intensity Focused Ultrasound," *Journal of the American Society of Echocardiography,* vol. 20, pp. 1400-1406, December 2007.

[16] S. A. Strickberger, T. Tokano, J.-U. A. Kluiwstra, F. Morady, and C. A. Cain, "Extracardiac Ablation of the Canine Atrioventricular Junction by Use of High-Intensity Focused Ultrasound," *Circulation,* vol. 100, pp. 203-208, July 1999.

[17] S. Mitnovetski, A. A. Almeida, J. Goldstein, A. W. Pick, and J. A. Smith, "Epicardial High-intensity Focused Ultrasound Cardiac Ablation for Surgical Treatment of Atrial Fibrillation," *Heart, Lung, and Circulation,* vol. 18, pp. 28-31, February 2009.

[18] Z. Xu, Z. Fan, T. L. Hall, F. Winterroth, J. B. Fowlkes, and C. A. Cain, "Size Measurement of Tissue Debris Particles Generated from Pulsed Ultrasound Cavitational Therapy – Histotripsy," *Ultrasound in Medicine & Biology,* vol. 35, pp. 245-255, 2009.

[19] Y. Kim, T.-Y. Wang, Z. Xu, and C. A. Cain, "Lesion Generation Through Ribs Using Histotripsy Therapy Without Abherration Correction," *IEEE Transactions on Ultrasonics, Ferroelectrics, and Frequency Control,* vol. 58, pp. 2344-2343, November 2011.

[20] A. M. Atz, J. A. Feinstein, R. A. Jonas, S. B. Perry, and D. L. Wessel, "Preoperative Management of Pulmonary Venous Hypertension in Hypoplastic Left Heart Syndrome With Restrictive Atrial Septal Defect," *The American Journal of Cardiology,* vol. 83, pp. 1224-1228, April 15 1999.

[21] J. P. Cheatham, "Intervention in the Critically Ill Neonate and Infant with Hypoplastic Left Heart Syndrome and Intact Atrial Septum," *Journal of Interventional Cardiology,* vol. 14, pp. 357-366, 2001.

[22] V. L. Vida, E. A. Bacha, A. Larrazabal, K. Gauvreau, R. Thiagaragan, F. Fynn-Thompson, F. A. Pigula, J. E. Mayer, Jr, P. J. del Nido, W. Tworetsky, J. E. Lock, and A. C. Marshall, "Hypoplastic Left Heart Syndrome With Intact or Highly Restrictive Atrial Septum: Surgical Experience From a Single Center," *The Annals of Thoracic Surgery,* vol. 84, pp. 581-586, August 2007.

[23] R. J. Holzer, A. Wood, J. L. Chicolm, S. L. Hill, A. Phillips, M. Galantowicz, and J. P. Cheatham, "Atrial Septal Interventions in Patients With Hypoplastic Left Heart Syndrome," *Catheterization and Cardiovascular Interventions,* vol. 72, pp. 696-704, November 1 2008.

[24] A. P. Vlahos, J. E. Lock, D. B. McElhinney, and M. E. van der Velde, "Hypoplastic Left Heart Syndrome With Intact or Highly Restrictive Atrial Septum : Outcome After Neonatal Transcatheter Atrial Septostomy," *Circulation,* vol. 109, pp. 2326-2330, May 2004.

[25] B. J. Maron, M. S. Maron, E. D. Wigle, and E. Braunwald, "The 50-Year History, Controversy, and Clinical Implications of Left Ventricular Outflow Tract Obstruction in Hypertrophic Cardiomyopathy From Idiopathic Hypertrophic Subaortic Stenosis to Hypertrophic Cardiomyopathy," *Journal of the American College of Cardiology,* vol. 54, pp. 191-200, July 2009.

[26] B. J. Maron, E. E. Peterson, M. S. Maron, and J. E. Peterson, "Prevalence of Hypertrophic Cardiomyopathy in an Outpatient Population Referred for Echocardiographic Study," *The American Journal of Cardiology,* vol. 73, pp. 577-580, March 1994.

[27] B. J. Maron, P. Spirito, M. J. Roman, M. Paranicas, P. M. Okin, L. G. Best, E. T. Lee, and R. B. Devereux, "Prevalence of Hypertrophic Cardiomyopathy in a Population-Based Sample of American Indians Aged 51 to 77 Years (the Strong Heart Study)," *The American Journal of Cardiology,* vol. 93, pp. 1510-1514, June 2004.

[28] M. S. Maron, J. J. Finley, M. Bos, T. H. Hauser, W. J. Manning, T. S. Haas, J. R. Lesser, J. E. Udelson, M. J. Ackerman, and B. J. Maron, "Prevalence, Clinical Significance, and Natural History of Left Ventricular Apical Aneurysms in Hypertrophic Cardiomyopathy," *Circulation,* vol. 118, pp. 1541-1549, October 2008.

[29] M. S. Maron, I. Olivotto, A. G. Zenovitch, M. S. Link, N. G. Pandian, J. T. Kuvin, S. Nistri, F. Cecchi, J. E. Udelson, and B. J. Maron, "Hypertrophic Cardiomyopathy Is Predominantly a Disease of Left Ventricular Outflow Tract Obstruction," *Circulation,* vol. 114, pp. 2232-2239, November 2006.

[30] B. J. Maron, "Role of Alcohol Septal Ablation in Treatment of Obstructive Hypertrophic Cardiomyopathy," *The Lancet,* vol. 355, pp. 425-426, February 2000.

[31] J. Veselka, "Alcohol Septal Ablation for Hypertrophic Obstructive Cardiomyopathy: Is it Safe?," *Catheterization and Cardiovascular Interventions,* vol. 73, pp. 520-521, June 2009.

[32] J. Veselka, D. Zemanek, P. Tomasov, S. Homolova, R. Adlova, and D. Tesar, "Complications of Low-Dose, Echo-Guided Alcohol Septal Ablation," *Catheterization and Cardiovascular Interventions,* vol. 75, pp. 546-550, March 2010.

[33] W. B. Kannel, P. A. Wolf, E. J. Benjamin, and D. Levy, "Prevalence, Incidence, Prognosis, and Predisposing Conditions for Atrial Fibrillation: Population-Based Estimates," *The American Journal of Cardiology,* vol. 82, pp. 2N-9N, October 1998.

[34] D. M. Lloyd-Jones, T. J. Wang, E. P. Leip, M. G. Larson, D. Levy, R. S. Vasan, R. B. D'Agostino, J. M. Massaro, A. Beiser, P. A. Wolf, and E. J. Benjamin, "Lifetime Risk for Development of Atrial Fibrillation : The Framingham Heart Study," *Circulation,* vol. 110, pp. 1042-1046, August 2004.

[35] P. A. Wolf, R. D. Abbott, and W. B. Kannel, "Atrial fibrillation as an independent risk factor for stroke: the Framingham Study," *Stroke,* vol. 22, pp. 983-988, August 1991.

[36] A. Takahashi, T. Kuwahara, and Y. Takahashi, "Complications in the Catheter Ablation of Atrial Fibrillation: Incidence and Management," *Circulation Journal,* vol. 73, pp. 221-226, February 2009.

[37] R. J. Allcock, J. J. O'Sullivan, and P. A. Corris, "Atrial septostomy for pulmonary arterial hypertension," *Heart,* vol. 89, pp. 1344-1347, November 2003.

[38] P. A. Corris, "Atrial Septostomy and Transplantation for Patients with Pulmonary Arterial Hypertension," *Seminars in Respiratory and Critical Care Medicine,* vol. 30, pp. 493-501, August 2009.

[39] B. G. Baylen, M. Grzeszczak, M. E. Gleason, S. E. Cyran, H. S. Weber, J. Myers, and J. Waldhausen, "Role of Balloon Atrial Septostomy Before Early Arterial Switch Repair of Transposition of the Great Arteries," *Journal of the American College of Cardiology,* vol. 19, pp. 1025-1031, April 1992.

[40] R. A. Hurwitz and D. A. Girod, "Percutaneous Balloon Atrial Septostomy in Infants with Transposition of the Great Arteries," *American Heart Journal,* vol. 91, pp. 618-622, May 1976.

[41] W. J. Rashkind and W. W. Miller, "Creation of an Atrial Septal Defect Without Thoracotomy. A Palliative Approach to Complete Transposition of the Great Arteries.," *The Journal of the American Medical Association,* vol. 196, pp. 991-992, June 1966.

[42] D. B. McElhinney, W. Tworetzky, and J. E. Lock, "Current Status of Fetal Cardiac Intervention," *Circulation,* vol. 121, pp. 1256-1263, March 2010.

[43] A. Mizrahi-Arnaud, W. Tworetzky, L. A. Bulich, L. E. Wilkins-Haug, A. C. Marshall, C. B. Benson, J. E. Lock, and D. B. McElhinney, "Pathophysiology, Management, and Outcomes of Fetal Hemodynamic Instability During Prenatal Cardiac Intervention," *Pediatric Research,* vol. 62, pp. 325-330, September 2007.

Chapter 2
Therapeutic Ultrasound to Non-Invasively Create Intra-Cardiac Communications in an Intact Animal Model

A majority component of this chapter has been published in *Catheterization and Cardiovascular Interventions* © 2011 Wiley. Reprinted, with permission, from [1].

2.1 Introduction

Several forms of congenital heart disease benefit from the creation or enlargement of an intra-cardiac communication such as an atrial septal defect (ASD) to ensure appropriate delivery of oxygenated blood to essential organs [2-13]. ASDs and less commonly ventricular septal defects (VSDs) are typically created in the fetus or neonate using cardiac catheterization or surgery with the associated risks of thrombo-embolic complications, cardiac perforation, and occasionally death. Previous work has demonstrated that histotripsy can create clearly demarcated perforations in excised porcine atrial and ventricular tissues using appropriate acoustic parameters [14]. In an open-chest canine model, histotripsy using an epicardial transducer position, accurately and efficiently generated ASDs without significant collateral damage or systemic clinical side effects [15].

The objective of this study was to determine if histotripsy could generate targeted intra-cardiac communications when positioned outside the body in an intact neonatal animal model. Safe creation of a targeted lesion in this manner, through multiple tissues layers including bone

that may interfere with ultrasound propagation, should address the feasibility of this technique to create similar lesions in human neonates with congenital heart disease. Because vertical orientation of the heart in pigs limits ultrasound access to the atrial septum, the interventricular septum was targeted in this study.

2.2 Methods

The procedures described here have been reviewed and approved by the University Committee on Use and Care of Animals at the University of Michigan. Nine healthy neonatal (2-3 weeks) pigs weighing 3-5kg comparable, in size to the human neonate or infant, underwent percutaneous transthoracic histotripsy of the antero-apical muscular interventricular septum to avoid the conduction system.

The animals were pre-anesthetized with Telazol (6mg/kg, IM) and Xylazine (2.2mg/kg IM), intubated and maintained on Isoflurane (1-3%) inhalation anesthesia, and paralyzed with pancuronium (0.1mg/kg) for the duration of the procedure. Heparin (200units/kg) was administered prior to the procedure and every hour thereafter if necessary. During the histotripsy procedure, the pig was submerged neck deep in a semi-upright position (Figure 2-1a) in degassed water, which ensures ultrasound propagation into the animal without forming cavitation in the propagation pathway. Each animal was monitored with pulse oximetry.

2.2.1 Histotripsy Apparatus

Ultrasound pulses for histotripsy treatment were generated by an external high power ultrasound therapy transducer. The transducer was placed in a degassed water filled cylinder covered by a thin plastic membrane that was acoustically transparent. The cylinder was then

placed into the warm degassed water bath that contained the submerged pig. This ensured continued ultrasound coupling from transducer, to water, through plastic membrane, to water and then to the chest wall (Figure 2-1a). An 8MHz imaging transducer (S8, SONOS 7500, Philips Healthcare, Andover, MA) was placed through the center hole of the therapy transducer (Figure 2-1b) and coupled to the neonatal pig in the same manner.

The therapy transducer was designed in our laboratory and fabricated by Imasonic, S.A., Besançon, France. The circular transducer has a center frequency of 1 MHz, a geometric focal length of 90 mm, an outer diameter of 100 mm, and a 40 mm inner hole for housing an ultrasound imaging probe (Figure 2-1b). Ultrasound pressure waveforms of this therapy transducer were previously measured in degassed water using a fiber optic probe hydrophone [16]. The peak negative and positive pressures used in the following experiment were 16 MPa and 32 MPa, respectively. Taking into account the attenuation caused by the approximately 1.5 cm thick chest wall tissue in the pathway, the peak negative pressure reaching the ventricular septum was estimated to be 13 MPa, resulting in a mechanical index of 13 [17]. The ultrasound pulses were 5 μs in duration (5 cycles at 1MHz) and separated by 1 ms (i.e., pulse repetition frequency = 1 kHz).

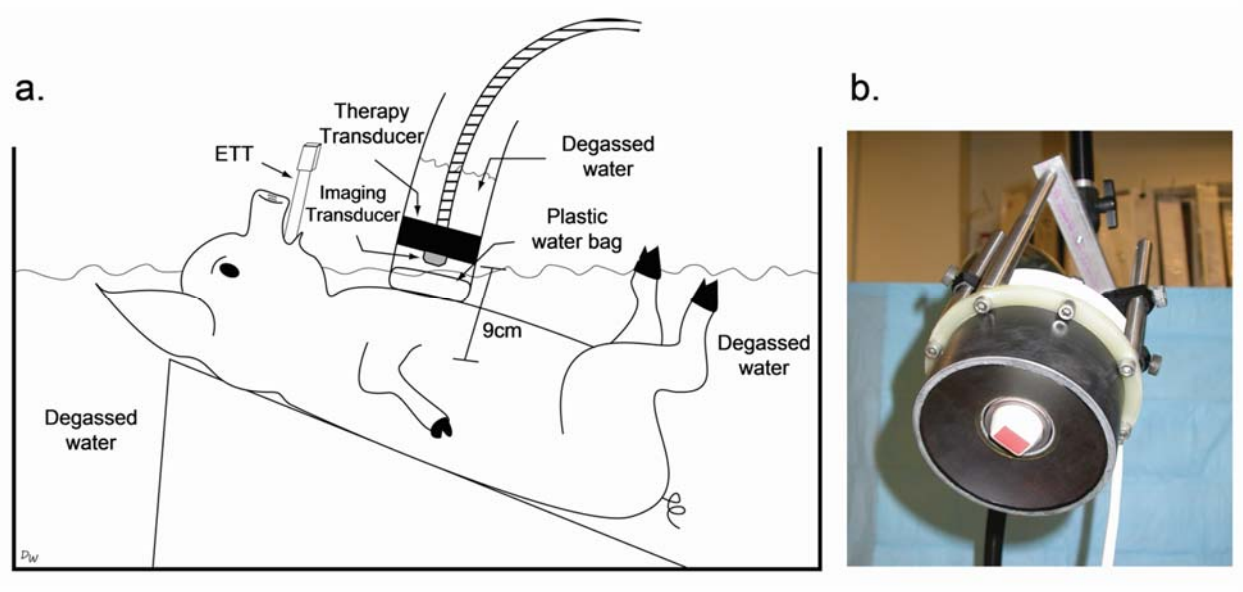

Figure 2-1: Histotripsy setup. a) The neonatal pig is placed in a water bath. The therapy and imaging transducers are placed into a cylinder filled with degassed water and coupled to the pig's chest by a plastic membrane filled with water. b) Close-up view of 1MHz therapy transducer with an imaging transducer protruding through center opening.

2.2.2 Histotripsy Treatment

Prior to the procedure, histotripsy pulses were applied to a water bath, producing a bright (hyperechoic) zone on a 2-dimensional ultrasound image. The front center of the hyperechoic zone was marked as the focal position (Figure 2-2a). The bubble cloud generated in the water for identifying focal location is larger than that in the tissue or blood. During the treatment, the bubble zone visualized by ultrasound was measured to be approximately 2-4 mm wide.

An 8 or 12 MHz phased array imaging probe was used on the chest wall to identify a window which provided imaging of the anterior ventricular septum in the axial resolution without substantial overlying lung. The therapeutic transducer was then moved by a 3-axis positioning system (Parker Hannifin, Rohnert Park, CA, USA) to align the focus marker on the ventricular septum (Figure 2-2b). The entire histotripsy procedure was guided by ultrasound

imaging using an 8 MHz phased array probe inserted into the central hole of the therapy transducer.

To verify the targeting accuracy, a small number of pulses were applied to produce a bubble cloud on the RV portion on the muscular interventricular septum, usually anterior to the moderator band (Figure 2-2c). Once the targeting was accomplished, respirations were held (in 1 minute intervals) and histotripsy treatment was applied to the ventricular septum. Ultrasound exposures were delivered in 1 minute intervals or until a hypoechoic (dark) channel was visualized through the ventricular septum. The area was interrogated with color Doppler to confirm the creation of a VSD.

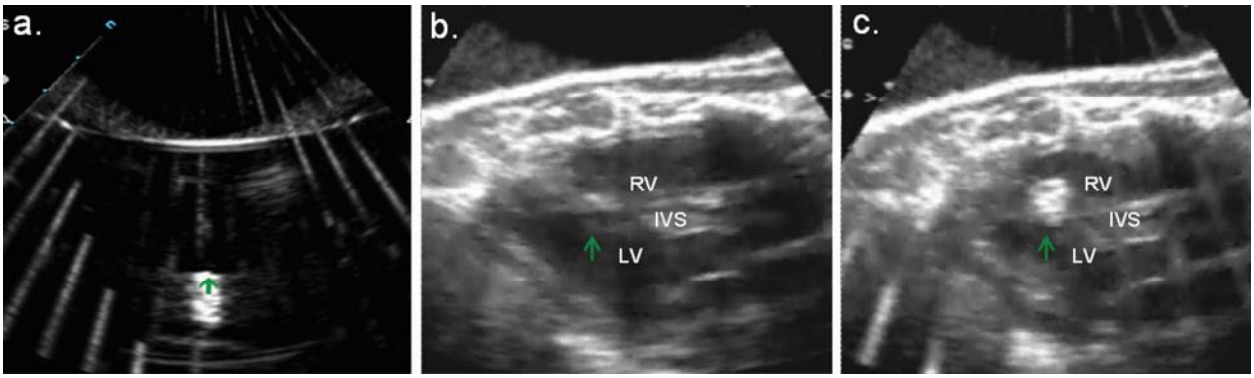

Figure 2-2: Generation of a cavitation bubble cloud. a) Prior to treatment, a cavitation bubble cloud is formed in degassed water to mark the focal point, seen by inserted arrow. b) The marked point is then positioned over the interventricular septum (IVS). c) Histotripsy is started and a hyperechoic bubble cloud is formed on the right ventricular (RV) side of the ventricular septum. LV (left ventricle)

2.2.3 Post-treatment Process

Within 2 hours after VSD creation, 6 of 9 animals were euthanized with a lethal dose of Pentobarbitol IV (100 mg/kg). In 3 animals, euthanasia was deferred for 2-3 days to evaluate sub-acute cellular changes related to histotripsy therapy and VSD creation. After euthanasia, the heart and lungs were extracted and fixed in a 10% formalin solution and dissected after a week

of fixation. The organs were first examined by gross evaluation and then processed with standard hematoxylin and eosin (H&E), phosphotungstic acid-hematoxylin (PTAH), and Gomori staining for pathological evaluation.

2.3 Results

Histotripsy applied extracorporeally propagated through multiple tissues layers including skin, bone, and portions of lung, and created a VSD in all 9 animals within 20 seconds to 4 minutes of therapy (Table 2-1).

Table 2-1: Summary of Histotripsy Treatments and Results

Case	Tx time (min)	Echo VSD size center (mm)	Path VSD size center (mm)	Flanking injury RV side (mm)	Flanking injury LV side (mm)	Complications
			Immediate euthanasia			
1	1.3	2.5	4	3.2	3.4	None
2	0.5	2.5	2.7	4.1	2.8	None
3	4	2	3.5	4.4	3.8	Bradycardia*
4	1.8	3.3	2.7	3.7	2.7	None
5	0.33	4.2	4.4	3.3	2.7	Bradycardia*
6	3	6.5	5.2	1.2	1.1	None
Mean	**1.8**	**3.5**	**3.7**	**3.3**	**2.8**	
STD	**1.4**	**1.7**	**0.7**	**1.1**	**0.9**	
			Delayed euthanasia			
7	1.6	3.3	2.8	0.6	0.9	None
8	1.7	4	NA	1.9	1.1	None
9	2.4	2	3.1	1.3	1.6	None
Mean	**1.9**	**3.1**	**3.0**	**1.3†**	**1.2†**	
STD	**1.2**	**1.4**	**1.3**	**1.4**	**1.1**	

Echo VSD size center column represents measurements of the center of VSD from two-dimensional imaging. Path VSD size center is a measurement of the VSD on H&E slides measured at the center of the defect. Measurement for animal 8 is not available (NA) secondary to tissue processing. Flanking injury RV (right ventricle) and LV (left ventricle) side are measurements from H&E slides of flanking injury from the border of acellular debris/VSD to the outermost border of myocyte damage taken from both sides of the created defect at the RV and LV surfaces respectively, and then averaged. STD (standard deviation) Tx (therapy).
* both animals recovered after a single dose of epinephrine
† $p < 0.05$ by 2 tailed T-test when compared to immediate euthanasia group

VSD creation was confirmed with 2-dimensional imaging, color flow Doppler (Figure 2-3), and pathologic evaluation.

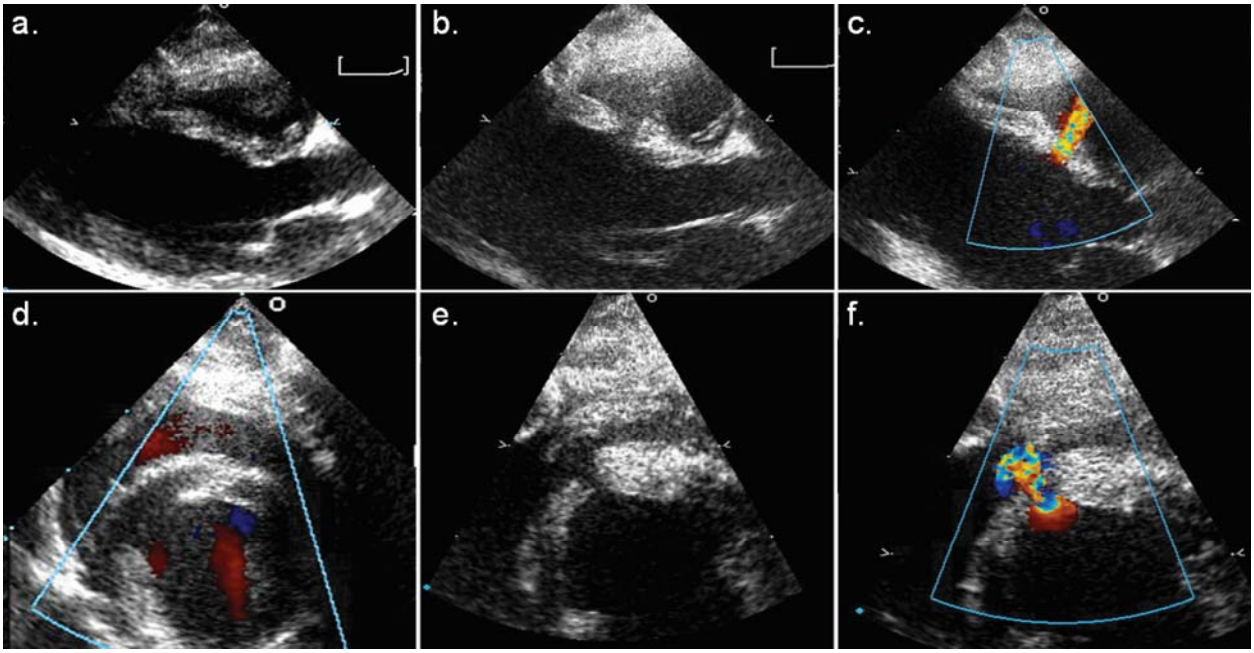

Figure 2-3: Creation of VSDs by histotripsy. a) Image of the ventricular septum in long axis prior to treatment. b) After treatment a VSD is seen on 2 dimensional ultrasound imaging, and (c) shunting is seen across the ventricular septum with color flow Doppler. Another example of a created VSD is seen in short axis with images prior to treatment (a), post treatment (b) and with color flow Doppler (c).

The size of created VSDs was variable (2-6.5 mm). All animals tolerated the procedure. Minor complications including transient hypoxia and ventricular ectopy were self-limited to the time during treatment. Seven animals received no intervention while 2 animals required epinephrine therapy for bradycardia. There were no major acute complications defined as pericardial effusion, sustained arrhythmia, or death. Two animals had mild unintended damage to the RV free wall due to its close proximity to the therapeutic focus. In the 3 animals, where euthanasia was deferred for 2-3 days post VSD creation, no changes in behavior, gait, appetite, vital signs, or other general characteristics were observed suggesting no global or neurologic effects from

histotripsy treatment. VSD size also remained the same in these animals, although a surrounding rim of increased echogenicity was apparent, likely resulting from inflammation and/or edema (Figure 2-4).

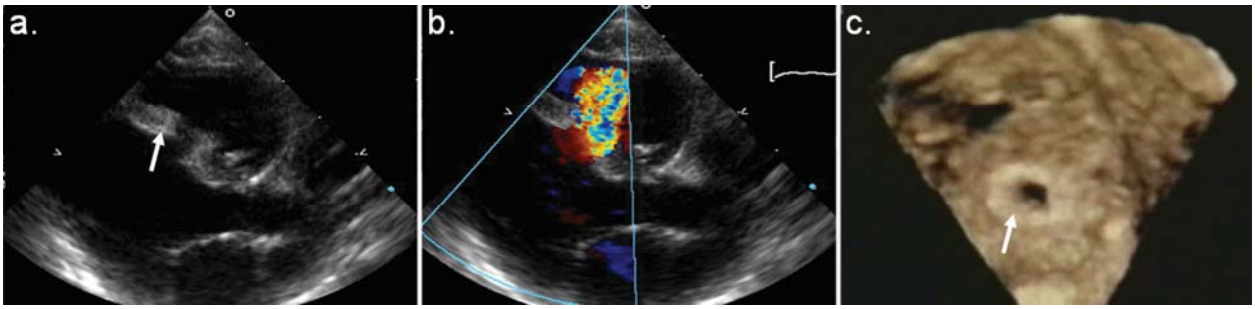

Figure 2-4: VSD two days after histotripsy therapy. a-b) Parasternal long axis view of VSD two days after creation in 2D and with color flow Doppler. c) 3-dimensional representation of same VSD shown in a modified apical four chamber view showing persistence of the septal defect. Note the hyperechoic (bright) rim surrounding the defect marked by white arrows.

Evaluation of function prior to histotripsy therapy and immediately before euthanasia (either acute or after 2-3 days) revealed no overt differences in global ventricular contractility, although regional wall motion abnormalities could not be thoroughly evaluated in this acute study. Two dimensional and color flow Doppler analysis of the heart after treatment revealed no significant changes in valve function post procedure.

2.3.1 Gross Morphology

In all 9 neonatal pigs studied, the epicardial surfaces appeared intact (Figure 2-5a-c). Seven animals had intact endocardial surfaces except for the created VSDs. In 2 animals where the bubble cloud did appear very close to the right ventricular anterior free wall, minor discoloration of the endocardial surface was visualized. No other unintended damage was visualized on gross examination.

Cardiac dissection of the 6 animals euthanized immediately post-procedure revealed demarcated damage in the ventricular septum**.** The VSD and surrounding hemorrhage indicated by dark colorization was observed on both sides of ventricular septum (Figure 2-5d). In the 3 animals with delayed euthanasia, the lumen of the VSD was more demarcated with smooth walls and the flanking hemorrhage appeared less substantial (Figure 2-5e).

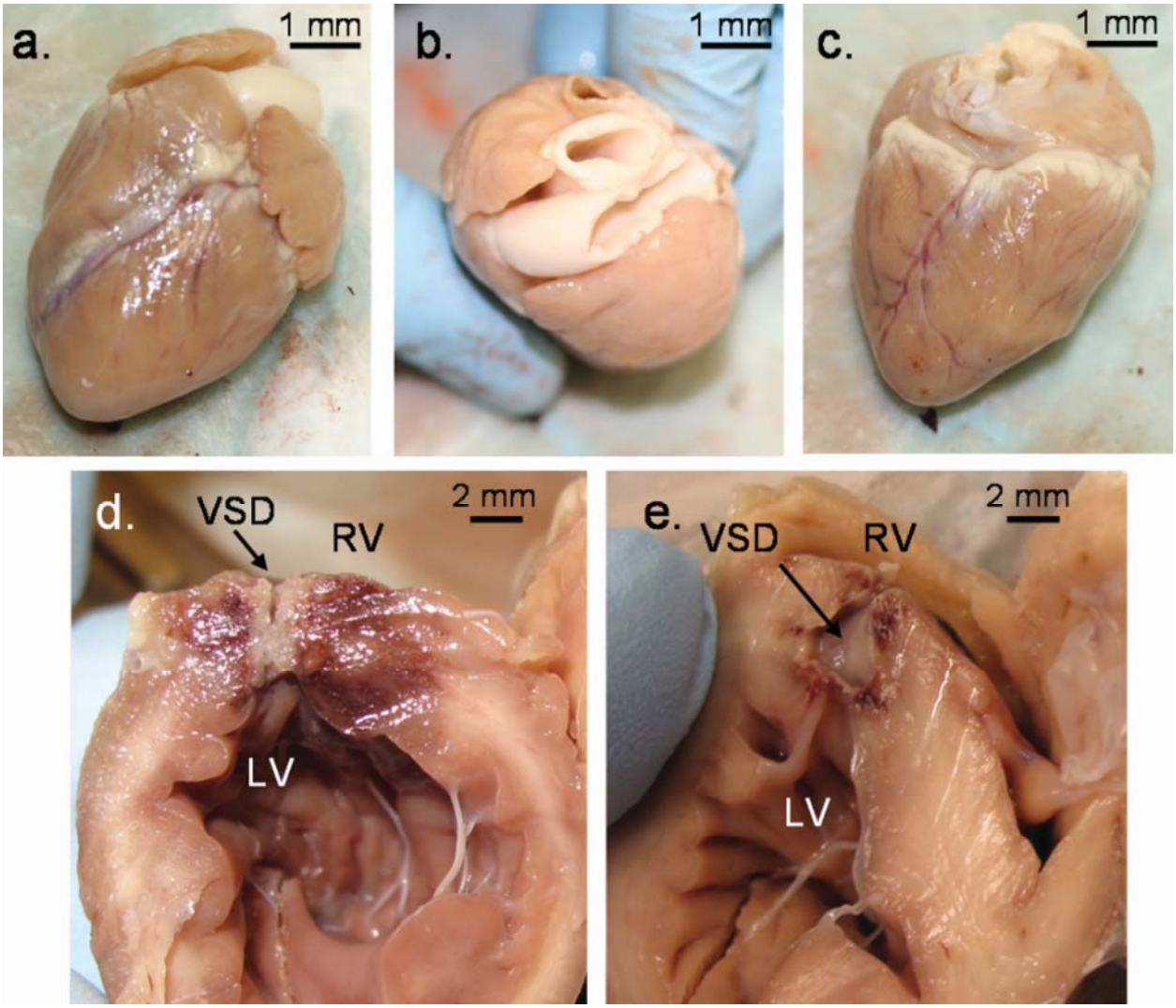

Figure 2-5: Cardiac pathology after histotripsy treatment. Gross pathology of the heart revealed no damage to the epicardial surface on the anterior (a), basilar (b), or posterior regions (c). Dissection revealed demarcated damage across with ventricular septum with flanking zones of hemorrhage in immediately euthanized animals (d). e) Similar lesions were observed in animals with delayed euthanasia but with smoother borders and less apparent flanking hemorrhage and/or damage.

Gross evaluation of the lungs revealed normal appearing lungs in 5 animals and very mild areas of congestion and focal hemorrhage in 4 comprising < 5% of lung tissue. No evidence of pulmonary embolus was found in the lungs on gross pathology in either the acute or sub-acute setting (Figure 2-6a). The ribs and overlying tissue in the ultrasound pathway were also examined. No visible damage was observed.

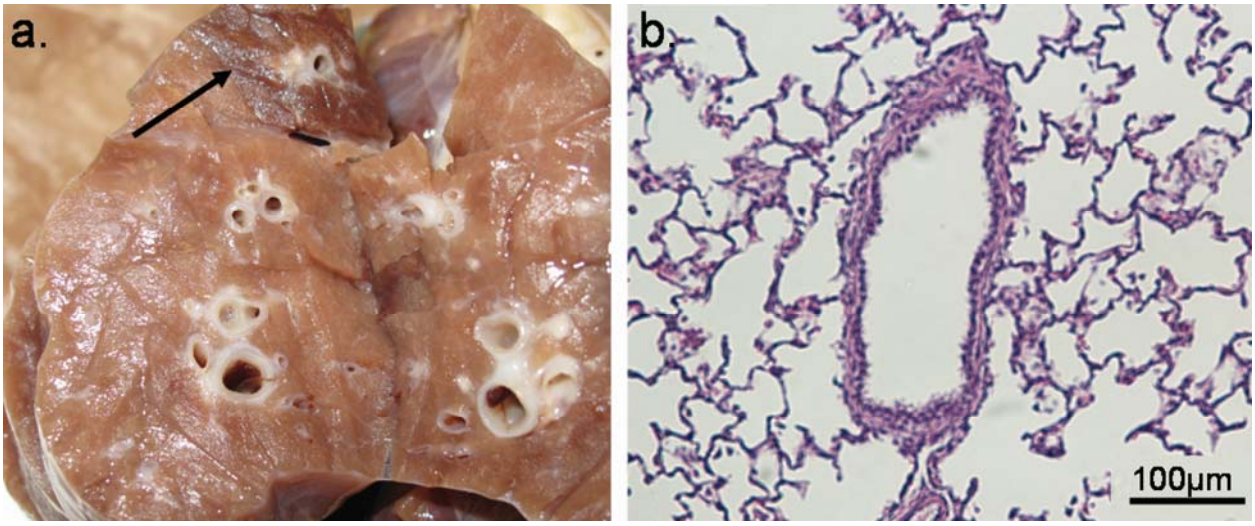

Figure 2-6: Lung pathology. a) Gross evaluation of the lungs revealed mostly healthy appearing tissue with only focal areas of hemorrhage or congestion (arrow). On histological analysis (b) no microscopic evidence of thrombo-embolic events were visualized.

2.3.2 Pathology

On H&E stained slides from animals immediately sacrificed, the central damage zone of the VSD contained acellular debris and platelet/fibrin deposits (Figure 2-7a-b). The average zone of necrosis in the center of the VSD was measured to be 3.7±0.7 mm (Table 2-1). VSDs from animals with delayed euthanasia had substantially less acellular debris (Figure 2-7c) but were similar in size with a mean of 3.0±1.3 mm (Table 2-1).

Immediately outside the acellular zone in acutely euthanized animals was a rim of hemorrhage and structurally intact myocytes with a more eosinophilic hue and contracted nuclei

in comparison to normal myocytes (Figure 2-7b). These myocytes were likely affected by histotripsy. The width of hemorrhage (measured from the acellular zone border to distal portion of flanking injury on both sides of defect in multiple tissue slices and then averaged to provide a circumferential report of flanking injury) on the right ventricular side was 3.3±1.1 mm and on the left ventricular side 2.8±0.9 mm (Table 2-1). Beyond this rim of damaged cells were normal appearing myocytes with no further discernable damage (Figure 2-7b). In the animals allowed to survive 2-3 days, evaluation of the lesion revealed a clear lumen compared to the acutely sacrificed animals and the flanking region contained activated fibroblasts and occasional inflammatory cell invasion suggesting progression of an inflammatory remodeling process (Figure 2-7c-d). The extent of flanking injury and/or inflammation was significantly less (1.3 mm vs. 3.3 mm on RV side and 1.2 mm vs. 2.8 mm on the LV side) comparing animals with delayed euthanasia to those with acute sacrifice (Table 2-1).

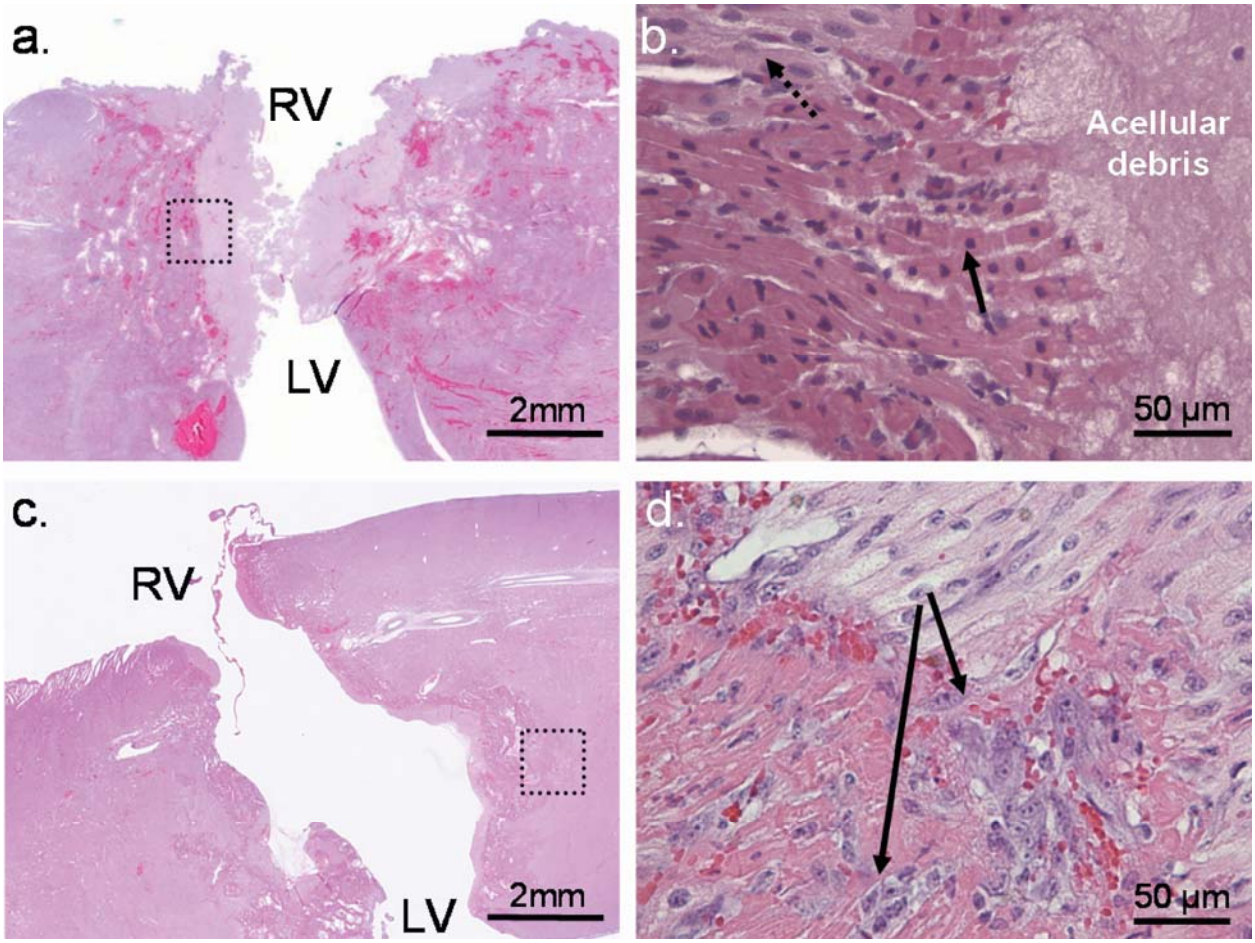

Figure 2-7: Histology of ventricular septum. a) Histological analysis revealed a central area of acellular debris and necrosis and flanking areas of contraction necrosis with hemorrhage in immediately sacrificed animals. (b) High power imaging of this border reveals tight demarcation of necrosis and myocyte injury (solid arrow) with normal appearing myocytes in the top left of image (dashed arrow). c) In animals with delayed euthanasia, the VSD is more clearly demarcated without acellular debris and d) there is evidence of cellular remodeling with presence of activated fibroblasts (arrows).

The areas of discoloration found in the right ventricular free wall in 2 animals described above corresponded to minor areas of contraction necrosis and hemorrhage suggesting the tissue was mildly affected by the histotripsy therapy. There were no areas of acellular debris or platelet/fibrin deposits. No other damage was noted in the heart on histological evaluation.

Histological evaluation of the lung revealed mostly normal appearing lung tissue with focal areas of congestion and hemorrhage (Figure 2-6b). There was no evidence for thrombo-embolic events and no debris from tissue fractionation was seen as evaluated by Gomori trichrome and PTAH staining.

2.4 Discussion

Therapeutic creation of cardiac septal defects in necessary for the palliation of several forms of congenital heart disease [2-5, 7, 9-11, 13] and is typically performed invasively with surgical or cardiac catheterization techniques [3, 7, 8]. This study demonstrates feasibility of "non-invasive" creation of an intra-cardiac defect by percutaneous pulsed cavitational ultrasound or histotripsy. Nine VSDs were created in 9 intact neonatal pigs with minimal collateral damage or systemic side-effects.

The size of created VSDs was variable (2-6.5 mm), likely related to varying aberration of ultrasound energy from intervening bones and tissue, as well as motion and consistency of the targeted ventricular septum. However, no correlations could be definitively made between amount of overlying tissue (range 14-17 mm) or septal motion (range 2.6-5 mm) on VSD size. Flanking injury, comparable to that seen in ASD creation in the open-chest canine model [15], was also observed and likely related to some of the same factors. These variables should be de-emphasized with an unobstructed acoustic window, such as the subcostal approach in human neonates (or other non-human primates), targeting of the thinner and less mobile atrial septum, as well as with improved transducer design allowing for motion tracking, ECG gating, and improved targeting (by decreasing focal distance and improving imaging resolution).

The pathologic evaluation of the animals allowed to survive 2-3 days after treatment revealed persistence in the size of VSD and less flanking injury with evidence of cellular remodeling (activated fibroblasts and inflammatory cell invasion), suggesting that some of the early flanking injury may be salvageable if not reversible. Further delineation of this inflammatory response, lesion maturation, and any systemic complications is currently under investigation in long-term studies.

No thrombo-embolic events were observed, consistent with prior demonstrations that particles created by histotripsy are largely < 6 μm (the size of a red blood cell) [18], a size unlikely to cause harm [19]. Still, more robust evaluation of end-organ complications such as thrombo-embolic events are currently being investigated by utilizing transcranial Doppler during treatment and diffusion MRI to evaluate brain and other end-organs after therapy. Preliminary MRI data have revealed no evidence of cerebral lesions up to 1 month after defect creation.

2.5 Conclusion

These data in combination with previous data demonstrating effective creation of ASDs in an open-chest dog model suggest that "non-invasive" creation of both atrial and ventricular septal defects via histotripsy is potentially feasible in the human neonate. Further investigation into potential side effects (embolic risk, maturation of lesions, and longer follow-up), improved transducer focusing and size optimization, and refinement of the approach are underway and necessary to develop the clinical potential of histotripsy for congenital heart disease and other applications.

2.6 References

[1] G. E. Owens, R. M. Miller, G. Ensing, K. Ives, D. Gordon, A. Ludomirsky, and Z. Xu, "Therapeutic ultrasound to noninvasively create intracardiac communications in an intact animal model," *Catheterization and Cardiovascular Interventions,* vol. 77, pp. 580-588, 2011.

[2] R. M. Aiyagari, A. P. Rocchini, R. T. Remenapp, and J. N. Graziano, "Decompression of the left atrium during extracorporeal membrane oxygenation using a transseptal cannula incorporated into the circuit," *Critical Care Medicine,* vol. 34, pp. 2603-2606, 2006.

[3] R. J. Holzer, A. Wood, J. L. Chicolm, S. L. Hill, A. Phillips, M. Galantowicz, and J. P. Cheatham, "Atrial Septal Interventions in Patients With Hypoplastic Left Heart Syndrome," *Catheterization and Cardiovascular Interventions,* vol. 72, pp. 696-704, November 1 2008.

[4] R. A. Hurwitz and D. A. Girod, "Percutaneous Balloon Atrial Septostomy in Infants with Transposition of the Great Arteries," *American Heart Journal,* vol. 91, pp. 618-622, May 1976.

[5] C. C. Lenox and J. R. Zuberbuhler, "Balloon septostomy in tricuspid atresia after infancy," *The American Journal of Cardiology,* vol. 25, pp. 723-726, 1970.

[6] J. Meadows, F. Pigula, J. Lock, and A. Marshall, "Transcatheter creation and enlargement of ventricular septal defects for relief of ventricular hypertension," *The Journal of Thoracic and Cardiovascular Surgery,* vol. 133, pp. 912-918, 2007.

[7] T. A. O'Connor, G. J. Downing, L. L. Ewing, and R. Gowdamarajan, "Echocardiographically guided balloon atrial septostomy during extracorporeal membrane oxygenation (ECMO)," *Pediatric Cardiology,* vol. 14, pp. 167-168, July 1993.

[8] W. J. Rashkind, "The complications of balloon atrioseptostomy," *The Journal of Pediatrics,* vol. 76, pp. 649-650, April 1970.

[9] W. J. Rashkind and W. W. Miller, "Creation of an Atrial Septal Defect Without Thoracotomy. A Palliative Approach to Complete Transposition of the Great Arteries.," *The Journal of the American Medical Association,* vol. 196, pp. 991-992, June 1966.

[10] T. Sato, H. Onoki, I. Kano, T. Horiuchi, T. Ishitoya, T. Abe, S. Ishikawa, S. Tanaka, and Y. Okada, "Balloon Atrial Septostomy in an Infant with Tricuspid Atresia," *The Tohoku Journal of Experimental Medicine,* vol. 101, pp. 281-288, 1970.

[11] P. M. Seib, S. C. Faulkner, C. C. Erickson, S. H. Van Devanter, J. E. Harrell, J. W. Fasules, E. A. Frazier, and W. R. Morrow, "Blade and balloon atrial septostomy for left heart decompression in patients with severe ventricular dysfunction on extracorporeal membrane oxygenation," *Catheterization & Cardivascular Interventions,* vol. 46, pp. 179-186, February 1999.

[12] V. L. Vida, E. A. Bacha, A. Larrazabal, K. Gauvreau, R. Thiagaragan, F. Fynn-Thompson, F. A. Pigula, J. E. Mayer, Jr, P. J. del Nido, W. Tworetsky, J. E. Lock, and A. C. Marshall, "Hypoplastic Left Heart Syndrome With Intact or Highly Restrictive Atrial Septum: Surgical Experience From a Single Center," *The Annals of Thoracic Surgery,* vol. 84, pp. 581-586, August 2007.

[13] A. P. Vlahos, J. E. Lock, D. B. McElhinney, and M. E. van der Velde, "Hypoplastic Left Heart Syndrome With Intact or Highly Restrictive Atrial Septum : Outcome After Neonatal Transcatheter Atrial Septostomy," *Circulation,* vol. 109, pp. 2326-2330, May 2004.

[14] Z. Xu, A. Ludomirsky, L. Y. Eun, T. L. Hall, B. C. Tran, J. B. Fowlkes, and C. A. Cain, "Controlled Ultrasound Tissue Erosion," *IEEE Transactions on Ultrasonics, Ferroelectrics, and Frequency Control,* vol. 51, pp. 726-736, June 2004.

[15] Z. Xu, G. Owens, D. Gordon, C. A. Cain, and A. Ludomirsky, "Noninvasive Creation of an Atrial Septal Defect by Histotripsy in a Canine Model," *Circulation,* vol. 121, pp. 742-749, February 2010.

[16] J. E. Parsons, C. A. Cain, and J. B. Fowlkes, "Cost-effective Assembly of a Basic Fiber-optic Hydrophone for measurement of High-Amplitude Therapeutic Ultrasound Fields," *Journal of the Acoustical Society of America,* vol. 119, pp. 1432-1440, March 2006.

[17] F. A. Duck, *Physical Properties of Tissue: A Comprehensive Reference Book*: Academic Press Ltd., 1990.

[18] Z. Xu, Z. Fan, T. L. Hall, F. Winterroth, J. B. Fowlkes, and C. A. Cain, "Size Measurement of Tissue Debris Particles Generated from Pulsed Ultrasound Cavitational Therapy – Histotripsy," *Ultrasound in Medicine & Biology,* vol. 35, pp. 245-255, 2009.

[19] M. K. Eskandari, "Cerebral Embolic Protection," *Seminars in Vascular Surgery,* vol. 18, pp. 95-100, 2005.

Chapter 3

Intermediate-term Effects of Intra-cardiac Communications Created Non-invasively by Therapeutic Ultrasound (Histotripsy) in a Porcine Model

A majority component of this chapter has been published in *Pediatric Cardiology* © 2011 Springer. Reprinted, with permission, from [1].

3.1 Introduction

Clearly demarcated perforations have been created previously by histotripsy in excised porcine cardiac tissue [2]. In addition, histotripsy has created atrial septal defects (ASDs) in an open-chest canine model [3] and was able to create ventricular septal defects (VSDs) through the intact chest of a neonatal pig without significant acute complications. These findings suggest that histotripsy has the potential to become a novel, noninvasive clinical tool not only for intracardiac communication creation but also for other applications involving tissue removal or destruction.

This study aimed to determine the intermediate-term clinical, pathologic, and systemic effects of intracardiac communications created by histotripsy in an intact neonatal animal model in an effort to address the safety profile of this technique as we continue to advance histotripsy toward clinical application for congenital heart disease. VSDs were targeted in this study as well because of the poor acoustic window to the atrial septum in neonatal pigs secondary to a different heart/lung orientation in the chest compared with humans.

3.2 Materials and Methods

The procedures described in this report have been reviewed and approved by the University Committee on Use and Care of Animals at the University of Michigan. For this study, six pigs weighing 3–5 kg underwent histotripsy-mediated VSD creation and were allowed to survive 1 month to provide intermediate-term data on lesion maturation and systemic effects. They then were compared with nine pigs that previously had undergone histotripsy-mediated VSD creation [4]. Thus, 15 pigs were evaluated in this study.

A detailed description of the VSD creation procedure has been reported previously [4]. We created VSDs because of the poor acoustic window to the atrial septum in this neonatal model. Briefly, the animals were preanesthetized with intramuscular Telazol (6 mg/kg) and xylazine (2.2 mg/kg), intubated, maintained on isoflurane (1–3%) inhalation anesthesia, and paralyzed with pancuronium (0.1 mg/kg). Heparin (200 U/kg) was administered before the procedure and every hour thereafter if necessary. During the histotripsy procedure, the pig was submerged neck deep in a semi-upright position in degassed water, which allowed ultrasound coupling and ensured propagation into the animal. Each animal was monitored with pulse oximetry and ultrasound imaging.

3.2.1 Histotripsy Therapy

The therapy transducer was designed in our laboratory and fabricated by Imasonic, S.A. (Besançon, France). The circular transducer has a center frequency of 1 MHz, a geometric focal length of 90 mm, an outer diameter of 100 mm, and a 40-mm inner hole to house an ultrasound imaging probe (S8, SONOS 7500; Philips Healthcare, Andover, MA, USA) for real-time monitoring during therapy. The ultrasound pressure waveforms of this therapy transducer were

measured previously in degassed water using a fiberoptic probe hydrophone [5]. The following experiment used a peak negative pressure of 16 MPa and a positive pressure of 32 MPa. Taking into account the attenuation caused by the approximately 1.5 cm-thick chest wall tissue in the pathway, the peak negative pressure reaching the ventricular septum was estimated to be 13 MPa [6]. This resulted in a mechanical index (MI) of 13, significantly higher than the maximum MI for diagnostic ultrasound of 1.9 [7]. The ultrasound pulses were 5 μs in duration (5 cycles of 1 MHz each) and separated by 1 ms (i.e., a pulse repetition frequency of 1 kHz). Before therapy, histotripsy pulses were applied to a water bath, producing a bright (hyperechoic) zone on a two-dimensional ultrasound image from the imaging transducer in-line with therapy. The front center of the hyperechoic zone was marked as the focal position. The therapeutic and in-line imaging transducers then were moved by a three-axis positioning system (Parker Hannifin, Rohnert Park, CA, USA) to align the focus on the ventricular septum. The best acoustic window, minimizing lung and bone obstruction, in the right parasternal position was chosen.

Once the ultrasound transducers were in position, a small number of pulses were applied to produce a bubble cloud (approximately 2–4 mm wide) on the right ventricular side of the muscular interventricular septum, usually anterior to the moderator band, to confirm targeting accuracy. Respirations then were held (in 1-min intervals), and histotripsy treatment was applied to the ventricular septum. Ultrasound exposures were delivered until a hypoechoic (dark) channel was visualized through the ventricular septum. The area was interrogated with color Doppler to confirm the creation of a VSD.

3.2.2 Post-treatment Process

As described previously [4], six animals (acute) were killed with a lethal dose of pentobarbitol (100 mg/kg) administered intravenously within 2 h of VSD creation, and three animals (subacute) were killed 2 to 3 days after VSD creation for evaluation of subacute cellular changes. The six animals from this study were killed 1 month (intermediate term) after VSD creation and monitored clinically during this time.

After the animals were killed, the heart and lungs were extracted, fixed in a 10% formalin solution, and dissected after a week of fixation. The organs were first examined by gross evaluation and then processed with standard hematoxylin and eosin (H&E) staining for pathologic evaluation.

The six intermediate-term animals had echocardiograms at the time they were killed for evaluation of ventricular function. They also were evaluated by magnetic resonance imaging (MRI) for any cerebral ischemic events. The MRI was performed at least 2 weeks after VSD creation on a 2T Varian Unity/Inova (Agilent, Santa Clara, CA) small animal imaging system. The piglets were placed in a specially built animal holding device, and the brain was imaged with the aid of a home-built radiofrequency probe. Multislice, spin-echo imaging (repetition time [TR] = 3 s, echo time [TE] = 60 ms) was performed using a slice thickness of 3 mm and an in-plane resolution of 600 lm. Images were acquired with and without diffusion-encoding gradients (b = 420 s/mm^2) to identify possible regions of ischemia.

3.3 Results

Histotripsy therapy propagated through multiple tissue layers including skin, bone, and portions of lung and created a VSD in 15 animals during 20 s to 13 min of therapy (mean, 3.1 ±

3.2 min). All the animals survived until scheduled to be killed. Minor complications including transient hypoxia and ventricular ectopy were self-limited to the time during treatment. There were no persistent arrhythmias or pericardial effusions. The VSDs, confirmed by color-flow Doppler (Figure 3-1), ranged in size from 2 to 6.5 mm (mean, 3.7 ± 1.6 mm). All VSDs persisted until the scheduled killing of the animals except for two initially small VSDs (2 and 2.5 mm) in the intermediate-term group, which spontaneously closed by 1 month. The remaining four VSDs in the intermediate-term group increased by an average of 1.0 ± 0.7 mm by the age of 1 month (Figure 3-1).

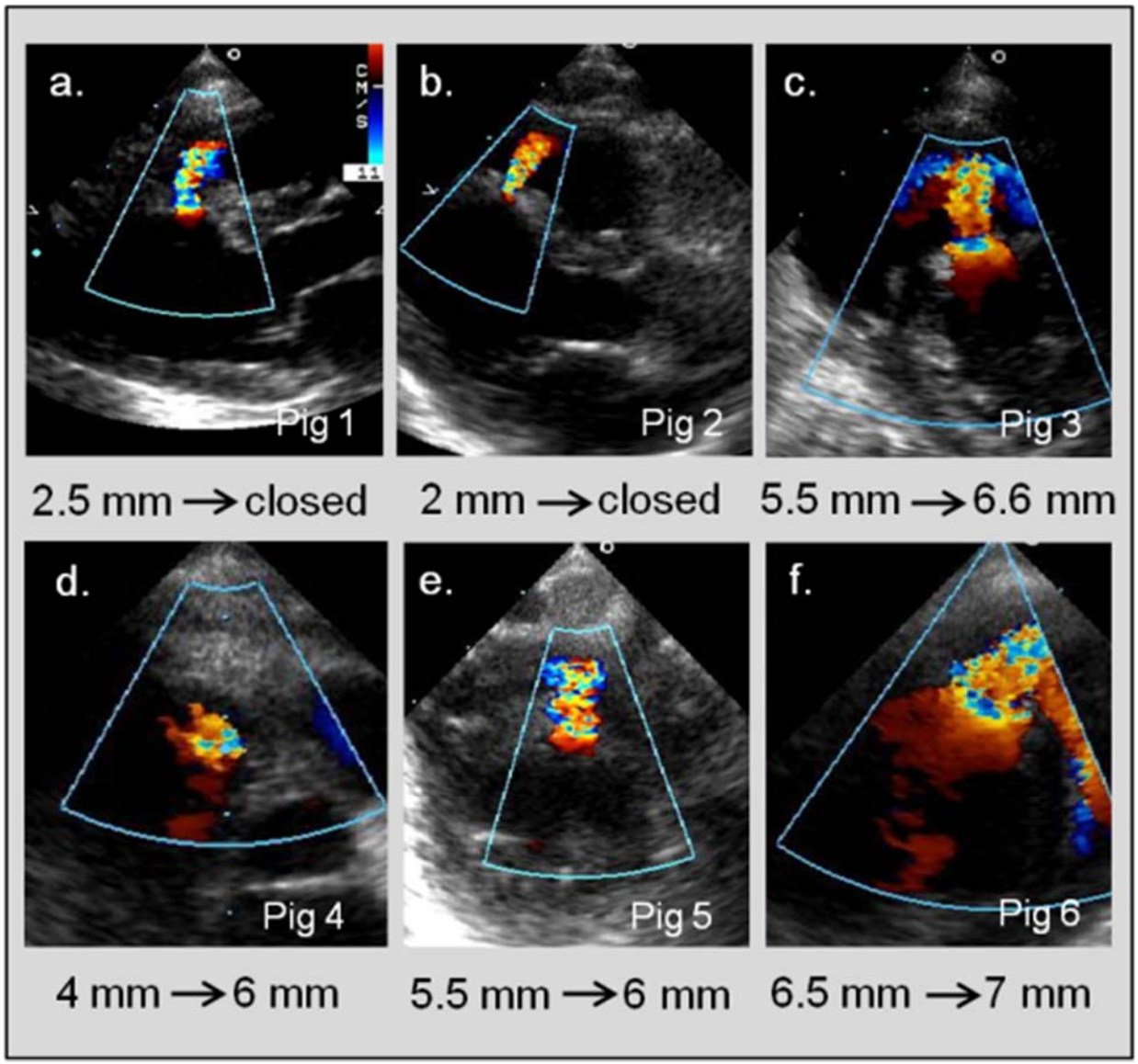

Figure 3-1: Color-flow Doppler echocardiogram images of VSDs created by histotripsy in animals allowed to survive for 1 month. Small lesions (a, b) spontaneously closed by 1 month, whereas larger initial lesions (c–f) had expanded by an average of 1 mm by the time the animals were killed.

Intermediate-term animals surviving 1 month experienced normal weight gain (Figure 3-2) and displayed no clinical evidence of untoward effects. Two animals in this group did have asymptomatic ascites seen on necropsy. These animals had the largest VSDs, suggesting a component of heart failure associated with the septal defect. The animal husbandry staff

observed no change in gait, activity, or affect. Echocardiograms performed before VSD creation and at the killing of the intermediate-term animals showed no global change in ventricular systolic function, as determined by two blinded interpreters.

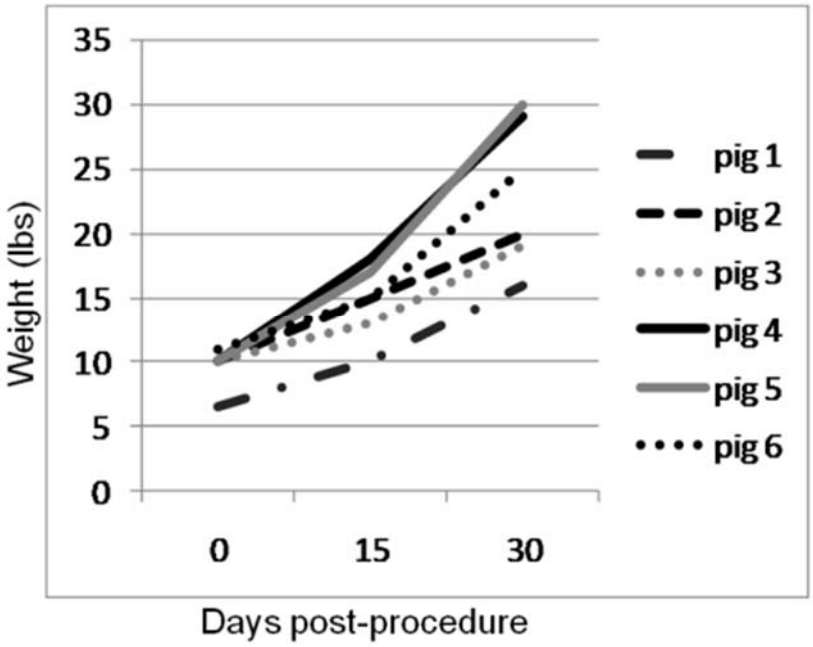

Figure 3-2: All the animals gained weight appropriately during the 1-month follow-up period.

3.3.1 Gross Morphology

No damage to intervening tissues was observed in any of the 15 neonatal pigs studied, and the epicardial surfaces appeared to be intact. In 13 of the animals, the endocardial surfaces were intact except for the created VSDs. Only 2 of the animals had minor discoloration of the endocardial surface of the right ventricular free wall. In these cases, the bubble cloud was in close proximity to this surface. No other unintended damage was visualized at gross examination.

Cardiac dissection showed demarcated damage in the ventricular septum of all the animals. In the acute animals (killed within 2 h), the VSD was filled with homogenized debris and flanked by hemorrhage and dark discoloration (Figure 3-3a, b). In 2 to 3 days (subacute), the

lumen of the VSD was clear, with improvement of the flanking hemorrhage and discoloration (Figure 3-3c, d). After 1 month of survival (intermediate term), no flanking injury or inflammation was observed, and the VSD was clearly demarcated with smooth borders (Figure 3-3e, f). In the two animals that had spontaneous VSD closure, fibrotic tissue was visualized at the previous defect without surrounding injury.

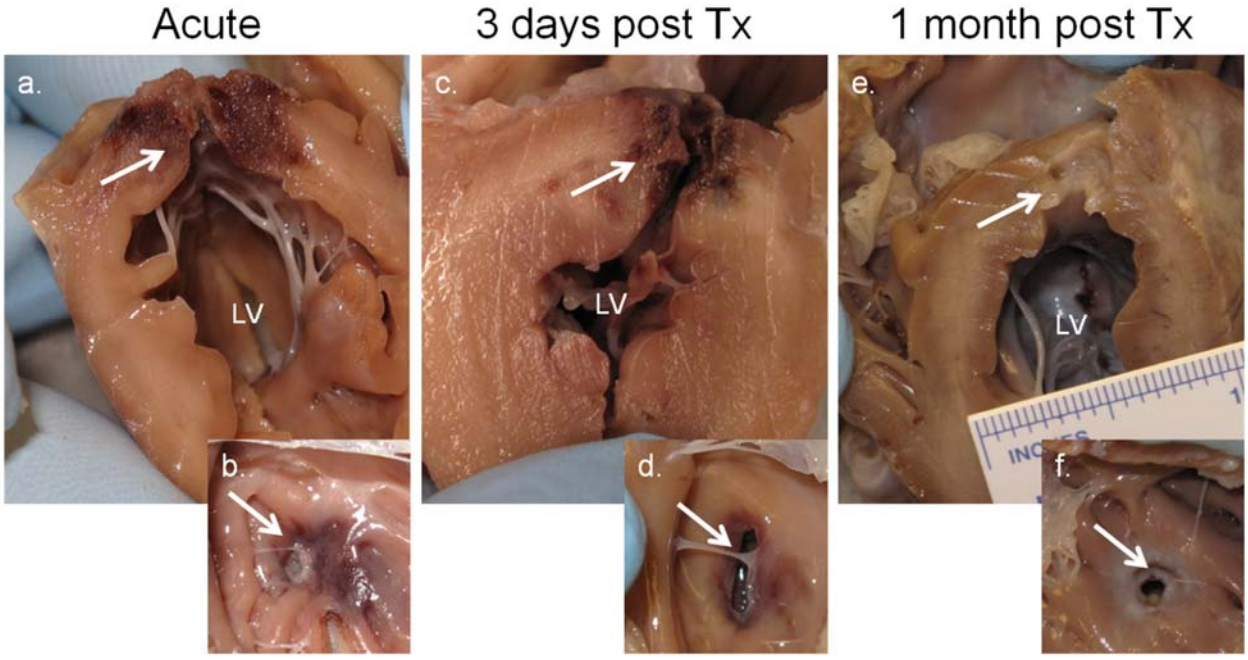

Figure 3-3: (a, b) Gross morphology of VSDs created by histotripsy therapy in animals killed acutely shows that the septal lesion was full of acellular fractionated debris and surrounded by hemorrhage. (c, d) By 3 days, flanking hemorrhage has improved, and the VSD lumen is clear without debris. (e, f) After 1 month, the myocardium appears to be healed, and a demarcated VSD is seen without evidence of surrounding hemorrhage or injury.

For four of the six acute animals, gross evaluation of the lungs showed very mild areas of congestion and focal hemorrhage comprising less than 5% of lung tissue. No evidence of hemorrhage or lung injury was observed by the pathologist (D.G) in the subacute or intermediate-term animals, and no evidence of pulmonary embolic events was observed in any animal of this series.

3.3.2 Pathology

In the acutely killed animals, histologic analysis showed VSDs consumed with acellular debris and platelet/fibrin deposits, with flanking hemorrhage and myocyte injury spanning approximately 3 mm from the VSD border (Figure 3-4a). In the subacute animals, the lumen of the VSD was clear, and the extent of flanking injury was less (1.3 mm), with infiltration of inflammatory/remodeling cells such as fibroblasts and macrophages (Figure 3-4b). By 1 month (intermediate term), the VSD was completely endothelized and surrounded by fibroblastic scar tissue immediately adjacent to the defect and then flanked by normal myocardium (Figure 3-4c).

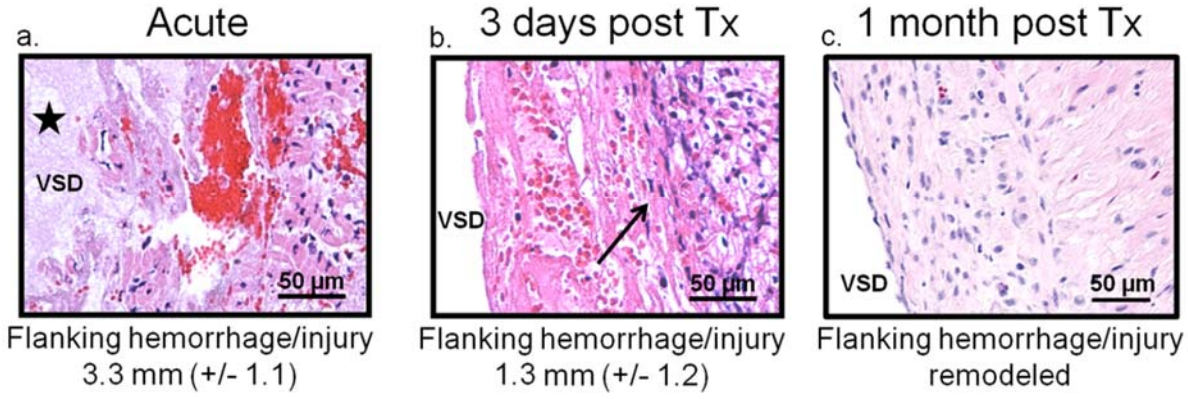

Figure 3-4: Histology of histotripsy-created VSDs. (a) Acutely, the VSD proper is consumed with acellular fractionated fibrin debris (star) flanked by hemorrhage and myocyte injury. (b) By 3 days, the VSD proper is clear, and cellular remodeling has begun with infiltration of fibroblasts (arrow) and an improvement in flanking hemorrhage. (c) After 1 month, an endothelial border exists surrounded by fibroblastic scar tissue immediately adjacent to normal-appearing myocardium.

3.3.3 Brain Imaging

All the intermediate-term animals underwent MRI of the brain a minimum of 2 weeks after VSD creation to evaluate for potential systemic embolic events. Diffusion weighted MRI showed no ischemic lesions.

3.4 Discussion

The ability to augment the structure or communications in the heart of an infant born with congenital heart disease, avoiding open heart surgery or invasive cardiac catheterization, could significantly advance the field of pediatric cardiology. Several congenital heart lesions require therapeutic creation of septal defects [8-13], which currently requires invasive procedures, thus identifying a clinical application for noninvasive ultrasound therapy. This study demonstrates the intermediate-term safety and effects of pulsed cavitational ultrasound (histotripsy) for the creation of intracardiac communications, building on previous reports of this technology.

A total of 15 VSDs (9 created previously and 6 created in this intermediate-term study) were created noninvasively using histotripsy therapy. All the animals survived the procedure, and the six animals killed after 1 month had no clinical symptoms and gained weight appropriately. In addition, ventricular systolic function was preserved, and no evidence of thromboembolic events was observed based on lung pathology and MRI of the brain. The lack of embolic events is consistent with *in vitro* data, showing that most particles created by histotripsy-induced tissue fractionation are less than 6 μm in size (size of a red blood cell) [14]. In all, although more robust evaluation of other distal tissues is necessary before clinical advancement, the aforementioned data suggest that histotripsy cardiac therapy is safe and that effects are

limited to the targeted region, similar to other reports of this technology used in different regions of the body [15-18].

Flanking hemorrhage and myocyte injury observed in the animals killed immediately after the procedure were completely resolved by 1 month, with some lesion expansion but suggesting that the unintentional damage was recoverable. However, in attempts to manipulate cardiac tissue, the smallest amount of acute unintentional damage, such as the mild right ventricular free wall damage seen in two acute animals, could be devastating. This damage likely resulted from the close proximity of the free wall to the target, the bubble cloud size, and motion. Thus, similar to attempts using other forms of therapeutic ultrasound [19-21], innovative efforts to incorporate ultrafast motion tracking, to decrease aberration from intervening tissues (i.e., bones), and to synchronize real-time color-Doppler feedback are underway to increase therapy accuracy further and decrease unintended injury.

The design of new therapeutic transducers with optimized focal distances allowing improved imaging quality represents another essential advancement necessary before clinical application. Acoustic coupling also requires improvement to prevent the need for water submersion used in these studies. Once these hurdles are surpassed and new optimized transducers with localized coupling ability are designed and tested, device exemption from the Food and Drug Administration will be obtained, paving the way for an inaugural clinical trial of histotripsy for congenital heart disease. Notably, transducer design for neonatal ASD creation can be simplified because of the optimal subcostal acoustic window free of intervening bone and the limited motion of the atrial septum in neonates [3], allowing earlier entry of histotripsy into the clinical realm.

Although others have used the thermal effects of high-intensity ultrasound for cardiac applications such as ablation of atrial fibrillation or other arrhythmias [22-24], no transcutaneous noninvasive ultrasound technique with the ability to create targeted cardiac perforations without acute or long-term sequelae has been reported. With further refinement and development, it is hoped that histotripsy may become an innovative clinical tool not only for noninvasive ASD creation but also for other lesions such as hypertrophic cardiomyopathy with obstruction, subaortic stenosis, membranous pulmonary atresia, and arrhythmias in which targeted tissue removal or destruction is required and may benefit from a noninvasive ultrasound approach. Furthermore, histotripsy also has been used noninvasively to create cardiac lesions in a fetal sheep model [11], suggesting that with further refinement and safety evaluation, histotripsy could play an exciting role in fetal cardiac intervention, further expanding its potential clinical applications.

3.5 Conclusion

Transcutaneous histotripsy is a safe and effective technique to create intra-cardiac communications non-invasively, without intermediate-term untoward effects. With further refinement and development, histotripsy has the potential to become an effective tool for palliation of congenital heart disease.

3.6 References

[1] G. Owens, R. Miller, S. Owens, S. Swanson, K. Ives, G. Ensing, D. Gordon, and Z. Xu, "Intermediate-Term Effects of Intracardiac Communications Created Noninvasively by Therapeutic Ultrasound (Histotripsy) in a Porcine Model," *Pediatric Cardiology,* vol. 33, pp. 83-89, 2012/01/01 2012.

[2] Z. Xu, A. Ludomirsky, L. Y. Eun, T. L. Hall, B. C. Tran, J. B. Fowlkes, and C. A. Cain, "Controlled Ultrasound Tissue Erosion," *IEEE Transactions on Ultrasonics, Ferroelectrics, and Frequency Control,* vol. 51, pp. 726-736, June 2004.

[3] Z. Xu, G. Owens, D. Gordon, C. A. Cain, and A. Ludomirsky, "Noninvasive Creation of an Atrial Septal Defect by Histotripsy in a Canine Model," *Circulation,* vol. 121, pp. 742-749, February 2010.

[4] G. E. Owens, R. M. Miller, G. Ensing, K. Ives, D. Gordon, A. Ludomirsky, and Z. Xu, "Therapeutic ultrasound to noninvasively create intracardiac communications in an intact animal model," *Catheterization and Cardiovascular Interventions,* vol. 77, pp. 580-588, 2011.

[5] J. E. Parsons, C. A. Cain, and J. B. Fowlkes, "Cost-effective Assembly of a Basic Fiber-optic Hydrophone for measurement of High-Amplitude Therapeutic Ultrasound Fields," *Journal of the Acoustical Society of America,* vol. 119, pp. 1432-1440, March 2006.

[6] F. A. Duck, *Physical Properties of Tissue: A Comprehensive Reference Book*: Academic Press Ltd., 1990.

[7] AIUM, *Acoustic Output Labeling Standard for Diagnostic Ultrasound Equipment: A Standard for How Manufacturers Should Specify Acoustic Output Data, Revision 1*. Laurel, MD: American Institute of Ultrasound in Medicine, 2008.

[8] J. P. Cheatham, "Intervention in the Critically Ill Neonate and Infant with Hypoplastic Left Heart Syndrome and Intact Atrial Septum," *Journal of Interventional Cardiology,* vol. 14, pp. 357-366, 2001.

[9] J. G. Gossett, A. P. Rocchini, T. R. Lloyd, and J. N. Graziano, "Catheter-based decompression of the left atrium in patients with hypoplastic left heart syndrome and restrictive atrial septum is safe and effective," *Catheter Cardiovasc Interv,* vol. 67, pp. 619-24, Apr 2006.

[10] R. J. Holzer, A. Wood, J. L. Chicolm, S. L. Hill, A. Phillips, M. Galantowicz, and J. P. Cheatham, "Atrial Septal Interventions in Patients With Hypoplastic Left Heart Syndrome," *Catheterization and Cardiovascular Interventions,* vol. 72, pp. 696-704, November 1 2008.

[11] Y. Kim, S. K. Gelehrter, C. G. Fifer, J. C. Lu, G. E. Owens, D. R. Berman, J. Williams, J. E. Wilkinson, K. A. Ives, and Z. Xu, "Non-invasive pulsed cavitational ultrasound for fetal tissue ablation: feasibility study in a fetal sheep model," *Ultrasound Obstet Gynecol,* vol. 37, pp. 450-7, Apr 2011.

[12] J. Meadows, F. Pigula, J. Lock, and A. Marshall, "Transcatheter creation and enlargement of ventricular septal defects for relief of ventricular hypertension," *The Journal of Thoracic and Cardiovascular Surgery,* vol. 133, pp. 912-918, 2007.

[13] W. J. Rashkind and W. W. Miller, "Creation of an Atrial Septal Defect Without Thoracotomy. A Palliative Approach to Complete Transposition of the Great Arteries.," *The Journal of the American Medical Association,* vol. 196, pp. 991-992, June 1966.

[14] Z. Xu, Z. Fan, T. L. Hall, F. Winterroth, J. B. Fowlkes, and C. A. Cain, "Size Measurement of Tissue Debris Particles Generated from Pulsed Ultrasound Cavitational Therapy – Histotripsy," *Ultrasound in Medicine & Biology,* vol. 35, pp. 245-255, 2009.

[15] A. P. Duryea, T. L. Hall, A. D. Maxwell, Z. Xu, C. A. Cain, and W. W. Roberts, "Histotripsy erosion of model urinary calculi," *Journal of Endourology,* vol. 25, pp. 341-344, February 2011.

[16] T. L. Hall, C. R. Hempel, K. Wojno, Z. Xu, C. A. Cain, and W. W. Roberts, "Histotripsy of the prostate: dose effects in a chronic canine model," *Urology,* vol. 74, pp. 932-937, October 2009.

[17] T. L. Hall, K. Kieran, K. Ives, J. B. Fowlkes, C. A. Cain, and W. W. Roberts, "Histotripsy of Rabbit Renal Tissue In Vivo: Temporal Histologic Trends," *Journal of Endourology,* vol. 21, pp. 1159-1166, October 2007.

[18] A. D. Maxwell, C. A. Cain, A. P. Duryea, L. Yuan, H. S. Gurm, and Z. Xu, "Noninvasive Thrombolysis Using Pulsed Ultrasound Cavitation Therapy – Histotripsy," *Ultrasound in Medicine & Biology,* vol. 35, pp. 1982-1994, 2009.

[19] L. Curiel, R. Chopra, and K. Hynynen, "In Vivo Monitoring of Focused Ultrasound Surgery Using Local Harmonic Motion," *Ultrasound in Medicine & Biology,* vol. 35, pp. 65-78, 2009.

[20] M. Pernot, M. Tanter, and M. Fink, "3-D Real-time Motion Correction in High-Intensity Focused Ultrasound Therapy," *Ultrasound in Medicine and Biology,* vol. 30, pp. 1239-1249, September 2004.

[21] M. Tanter, M. Pernot, J. F. Aubry, G. Montaldo, F. Marquet, and M. Fink, "Compensating for bone interfaces and respiratory motion in high-intensity focused ultrasound," *Int J Hyperthermia,* vol. 23, pp. 141-51, Mar 2007.

[22] S. Mitnovetski, A. A. Almeida, J. Goldstein, A. W. Pick, and J. A. Smith, "Epicardial High-intensity Focused Ultrasound Cardiac Ablation for Surgical Treatment of Atrial Fibrillation," *Heart, Lung, and Circulation,* vol. 18, pp. 28-31, February 2009.

[23] B. Schmidt, M. Antz, S. Ernst, F. Ouyang, P. Falk, J. K. R. Chun, and K.-H. Kuck, "Pulmonary vein isolation by high-intensity focused ultrasound: First-in-man study with a steerable balloon catheter," *Heart Rhythm,* vol. 4, pp. 575-584, 2007.

[24] R. Yu, C. Ma, J. Dong, X. Liu, and J. Kang, "Transesophageal high intensity focused ultrasound ablation of left atrium posterior wall: New method for treating atrial fibrillation," *Medical Hypotheses,* vol. 70, pp. 654-656, 2008.

Chapter 4
Histotripsy Cardiac Therapy System Integrated with Real-time Motion Correction

A majority component of this chapter has been published in *Ultrasound in Medicine & Biology*

4.1 Introduction

Histotripsy has been successful in creating intra-cardiac communication in an open chest canine heart model [2], an intact neonatal porcine model [3, 4], and an intact in utero fetal sheep model [5]. The perforations created in these studies generally have 1-4 mm of hemorrhage surrounding the perforation. During these experiments, the heart motion perpendicular to the direction of ultrasound therapy propagation was small (< 2mm), while the heart motion along the direction of therapy propagation was sufficiently large (up to 17 mm) to move the septum out of the focal zone, resulting in reduced treatment efficiency and the potential for collateral damage. Furthermore, in cardiac applications involving adult hearts, such as atrial fibrillation, the cardiac motion will likely be significantly larger in both perpendicular and parallel directions to the ultrasound propagation. As such, the improved accuracy and efficiency motion correction provides will be increasingly necessary in order to reliably administer histotripsy therapy in these future applications.

Several target motion estimation and correction algorithms have been explored in conjunction with high intensity focused ultrasound (HIFU) therapy. Respiratory gating has been used to synchronize with HIFU applications to switch off therapy during breaths [6, 7]. More sophisticated approaches have also been developed to adjust the therapy focus to follow the target position in real-time. For example, ultrasound speckle tracking was employed to adjust the therapy focus to track the respiration motion using correlations of pulse-echo sequences from a subset of the transducers of the therapy phased array [8, 9]. Optical flow image processing techniques have also been utilized on real-time 2D ultrasound images for motion compensation in HIFU application [10]. Motion compensation was also investigated for magnetic resonance imaging (MRI) guided HIFU, such as the use of periodic respiratory motion and statistical models [11-14] and tracking the target position in the image plane while compensating for the out-of-plane motion by dynamic slice tracking [15]. These motion correction methods showed improvement in treatment efficiency and collateral damage reduction, but were mostly focused on treating slower moving abdominal organs.

The addition of fast cardiac motion on top of large respiratory motions significantly increases the complexity of tracking targets in the heart as opposed to tracking in other organs. Many algorithms have been developed for tracking cardiac motion in ultrasound imaging to evaluate heart function. These methods include myocardial border segmentation using deformable models [16], myocardial motion and deformation estimation using phase shift estimation [17], spatio-temporal nonrigid registration with B-Spline interpolation [18], optical flow methods to compute local myocardial movements [19], and block motion estimation and speckle tracking techniques [20]. However, none have yet been combined to adjust the therapy focus in real-time for motion correction in an integrated ultrasound cardiac therapy system.

In this chapter, we present a histotripsy-based cardiac therapy system integrated with real-time motion correction and treatment monitoring using ultrasound imaging. For this system, the motion correction must run at high frame rates due to the fast heart motion, and be robust against direct and indirect acoustic and electromagnetic interference from the high intensity histotripsy pulses. To address these challenges, we developed an ultrasound image-based motion tracking algorithm that utilizes a fast block matching technique, with real-time filtering for estimation error reduction. This algorithm was chosen due to its low computational requirements and ease of integration with the ultrasound image-guided histotripsy therapy system. In addition to the motion tracking capability, this integrated system has ultrasound imaging as real-time treatment monitoring that is free from interference of the therapy pulses. This integrated system was tested by performing two dimensional (2D) motion tracking based on ultrasound images and applying the motion feedback to correct for the one dimensional (1D) motion along the therapy axis by steering the focus of the annular therapy array. In this initial study lateral motion correction was not performed based our previous experiments where communication through the atrial or ventricular septum (a membrane separating the two atria or ventricles) was generated for treatment of congenital heart diseases [2-4]. In those studies, the axial motion (along the direction of ultrasound propagation) was observed to be the main motion of the atrial/ventricular septum, with only small motion in other directions. Due to the limitations of the hardware, 2D instead of three dimensional (3D) motion tracking was tested for this initial feasibility study. The integrated system developed here could potentially be upgraded to 3D by replacing the annular therapy array with a 2D phased array and replacing the 2D imaging probe with a 3D imaging probe.

The performance of the current integrated system was evaluated in three steps *in vitro* followed by *in vivo* feasibility testing. First, to evaluate the tracking accuracy of the integrated system at different velocities, the actual movement path of the target was recorded by high speed optical images and compared with the estimated movement path from the algorithm. Second, to evaluate the treatment accuracy of the system, the size of the lesion created in moving tissue phantoms with the motion correction was compared to that produced without correction. Third, to investigate the efficiency of the system, the erosion rate produced with the motion correction in tissue phantoms and *ex vivo* porcine cardiac tissue was compared to that without correction. Finally, an *in vivo* feasibility experiment was conducted to determine the feasibility of integrating the algorithm into histotripsy therapy image guidance and targeting procedures.

4.2 Methods

4.2.1 Motion Tracking System Design

The motion tracking system we developed uses a custom algorithm to track a feature on ultrasound images using image processing techniques. This algorithm was integrated directly into the imaging sequence of an ultrasound imaging system. The imaging acquisition was synchronized with a 1 MHz histotripsy therapy array to minimize the interference of the therapy pulses on the ultrasound image. The imaging system's host computer processed the tracking algorithm and provided the results to the therapy array controller, updating the therapy focal position in real-time. Meanwhile, the treatment process was monitored through ultrasound imaging. The integrated system, consisting of the motion tracking algorithm, the ultrasound imaging system, and the histotripsy therapy system is described in detail below.

Ultrasound Imaging System

The ultrasound images were acquired by a Verasonics® Data Acquisition System (VDAS; Verasonics Inc., Redmond, WA, USA), interfaced with a Mac Pro desktop computer (Apple Inc., Cupertino, CA, USA), using an ATL HDI P7-4 (Philips, Andover, MA, USA), 5 MHz phased array imaging probe. This system was chosen for its high frame rate capabilities (by using a variable number of plane wave acquisitions) and flexible programmability allowing integration of processing algorithms within the imaging sequence.

To avoid interference from the histotripsy pulses, ultrasound image acquisitions were delayed 0.2 – 0.5 ms after the histotripsy pulses. Following this delay, image acquisition required 135 μs per steered plane wave acquisition (round-trip propagation time, which is dependent on the depth of the target). The number of plane wave acquisitions per image was chosen to balance sufficiently high image quality (spatial resolution) with a sufficiently high frame rate (temporal resolution). Though image quality could be improved by increasing the number of plane wave acquisitions per image, doing so reduced the overall frame rate. Therefore, while a single plane wave acquisition per image provided sufficient image quality and a higher average frame rate (62 Hz) for motion tracking *in vitro*, 5 steered plane wave acquisitions were necessary for tracking in the *in vivo* experiment to achieve adequate imaging quality through the increased overlying tissue, reducing the average frame rate (31 Hz). Because of the low duty cycle (< 1%) used in histotripsy therapy pulses; the period between adjacent histotripsy pulses was sufficiently long to allow imaging acquisitions. Figure 4-1 shows a timing diagram example to illustrate the synchronization.

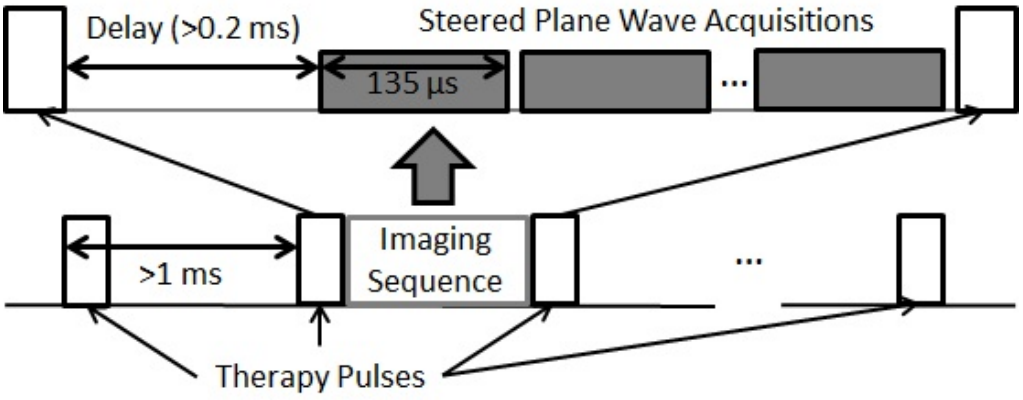

Figure 4-1: Timing diagram illustrating the synchronization and integration of the imaging sequence between therapy pulses with typical parameters.

Motion Tracking Algorithm

Our real-time motion-tracking algorithm is based on tracking a distinguishable target feature on ultrasound images by comparison with a reference sub-image containing that target feature (reference block). First, the location of a moving target is identified in the current ultrasound image frame by finding the best match of the reference block in the current ultrasound frame using a block matching method. A reference image of the target is captured before therapy, which contains unique features or borders that can be distinguished from other structures in its vicinity. This reference block can be located within the therapy target region or nearby, provided the target region and reference feature move in unison, allowing the flexibility to track a prominent tissue feature but treat in another nearby location. The best matching block in the current frame in comparison to the reference block is identified by minimization of the sum of absolute difference (SAD) criterion. The error for a given location is found by subtracting the reference image from a block of the current frame centered at this potential new target location, and the absolute values of these pixel errors were summed to obtain the SAD (Equation 4.1).

$$SAD(i,j) = \sum_{x=1}^{N_x}\sum_{y=1}^{N_y}\left|ref(x,y) - image\left(i + x - \left\lfloor\frac{N_x}{2}\right\rfloor, j + y - \left\lfloor\frac{N_y}{2}\right\rfloor\right)\right| \qquad \text{Equation 4.1}$$

In this equation, the reference block "$ref(\cdot,\cdot)$" of size (N_x, N_y) is compared to the same-sized block surrounding the point (i,j) in the current image frame "$image(\cdot,\cdot)$".

To accelerate the computation, diamond search technique [21] was used to minimize search time in the current frame using knowledge of the target's position in the previous frame. First, to establish the initial position estimate on the first ultrasound frame, a single coarse search is performed over the entire frame. In subsequent frames, the diamond search procedure starts at the estimate from the previous frame, computing the SAD error for this location and those in a large diamond search pattern (LDSP) around it (Figure 4-2). Re-centering at the location among these with the lowest error, it computes the necessary additional SAD values to cover another LDSP around this point. This continues until the center point maintains the lowest SAD value, at which time a small diamond search pattern (SDSP) around that location produces the final estimate of the target position. This approach remains accurate so long as the overall frame rate is fast enough to keep the target's frame to frame motion small, thus ensuring the local minimum SAD corresponds to the target's new position.

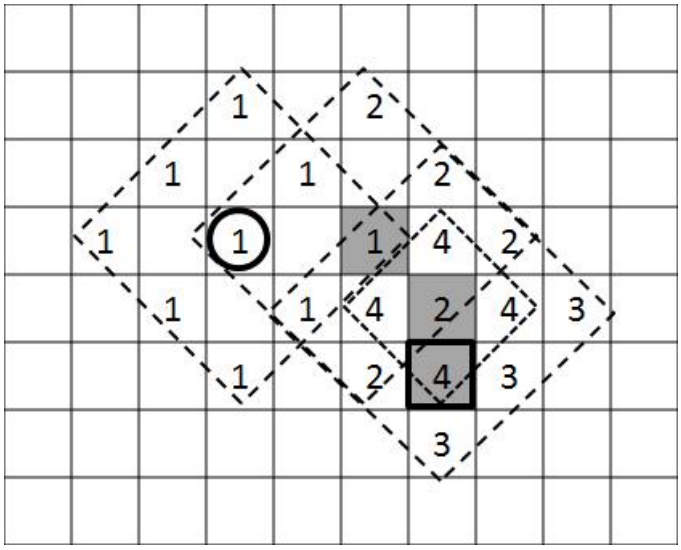

Figure 4-2: Illustration of the diamond search procedure: starting from the previous target position (bold circle), successive LDSP iterations (1-3) are computed with the best match of each shaded gray. Once the center location remains the best match (shaded "2" remained best match on iteration 3), the SDSP locations (4) are tested and the best match is the new estimate of the target's position (bold square).

The block matching estimate is filtered from frame to frame using a Kalman filter to reduce the interference of the noise on tracking. A need for filtering was based on early testing of the algorithm using ultrasound B-mode videos taken during *in vivo* experiments of two neonatal pigs and two fetal sheep. Without the Kalman filter, the estimated position within ultrasound videos was observed to jump around the actual position of the target rapidly. The addition of the Kalman filter removed this rapid fluctuation and improved tracking accuracy by an estimated 13%. Our implementation of the Kalman filter uses the horizontal and vertical positions ($h(n)$ and $v(n)$) and velocities ($h'(n)$ and $v'(n)$) as the current state, with the estimate of the current position equal to the previous position plus the previous velocity times the time interval between frames (Δt). The system is assumed to be driven by changes in the velocity corresponding to samples of a zero-mean Gaussian random variable, $u(n)$ whose variances, ($\sigma_{u,h}$ and $\sigma_{u,v}$) must

be estimated based on the expected target motion. The state equation for our Kalman filter is therefore:

$$\begin{bmatrix} h(n) \\ v(n) \\ h'(n) \\ v'(n) \end{bmatrix} = \begin{bmatrix} 1 & 0 & \Delta t & 0 \\ 0 & 1 & 0 & \Delta t \\ 0 & 0 & 1 & 0 \\ 0 & 0 & 0 & 1 \end{bmatrix} \cdot \begin{bmatrix} h(n-1) \\ v(n-1) \\ h'(n-1) \\ v'(n-1) \end{bmatrix} + \begin{bmatrix} 0 & 0 \\ 0 & 0 \\ 1 & 0 \\ 0 & 1 \end{bmatrix} \cdot u(n) \qquad \text{Equation 4.2}$$

$$u(n) \sim N\left(\begin{bmatrix} 0 \\ 0 \end{bmatrix}, \begin{bmatrix} \sigma_{u,h} & 0 \\ 0 & \sigma_{u,v} \end{bmatrix}\right)$$

Observation of the system is through estimates of the horizontal and vertical positions from our block matching algorithm ($\bar{h}(n)$ and $\bar{v}(n)$). These estimates are assumed to be accurate, but corrupted by zero-mean Gaussian noise, $w(n)$ whose variances, ($\sigma_{w,h}$ and $\sigma_{w,v}$) must be determined based on the current imaging quality. The observation equation for our Kalman filter is therefore:

$$\begin{bmatrix} \bar{h}(n) \\ \bar{v}(n) \end{bmatrix} = \begin{bmatrix} 1 & 0 & 0 & 0 \\ 0 & 1 & 0 & 0 \end{bmatrix} \cdot \begin{bmatrix} h(n) \\ v(n) \\ h'(n) \\ v'(n) \end{bmatrix} + w(n) \qquad \text{Equation 4.3}$$

$$w(n) \sim N\left(\begin{bmatrix} 0 \\ 0 \end{bmatrix}, \begin{bmatrix} \sigma_{w,h} & 0 \\ 0 & \sigma_{w,v} \end{bmatrix}\right)$$

For a given scenario, the variances of the driving force and observation noise are the only independent variables and must be tuned by analyzing video and tracking performance of the system in each individual treatment, before delivering histotripsy therapy. The Kalman filter recursion then produces the final estimate of the new target position based on a weighted average of the result of the search algorithm with an estimate of where the target should be based on its previous position and velocity. This final position estimate is then passed through a custom 1 MB/sec universal serial bus (USB) communication link (FT245BL, Future Technology Devices

International Ltd., Glasgow, UK) to the histotripsy therapy array controller to adjust the therapy focus to the target's new estimated position in less than 1 ms.

Histotripsy Therapy System

Histotripsy therapy was delivered by a 1 MHz high power ultrasound annular array transducer (Imasonic, SA, Besançon, France). This transducer is composed of 16 equal-area ring elements aligned confocally on a spherical segment, allowing axial focal steering. The transducer had a 100mm aperture and was geometrically focused at 90mm (f# = 0.9), with a 40mm central hole to accommodate an imaging probe. The annular array was driven by custom hardware, implemented on a field programmable gate array (FPGA, Cyclone II, Altera Corp., San Jose, CA, USA) with USB connectivity to control the ultrasound therapy output parameters in real-time. Focal patterns for axial foci between 80 and 100 mm with 0.5 mm spacing between adjacent foci were programmed and stored in the FPGA. During therapy, the therapy controller can then change the transducer focus position to any position within these pre-programmed locations in less than 1 ms. This driver output was then routed to custom high-power amplifiers built in-house and electronically matched to the load transducer.

In all *in vitro* experiments, the transducer was driven at the same input voltage level, corresponding to peak negative/positive pressures of -21.2/88.5 MPa in free field at the geometric focus. This was measured with a fiber optic probe hydrophone [22]. A pulse duration of 3 cycles was used for calibration to prevent cavitation at the fiber tip, while still achieving the same peak pressures as longer pulses since the transducer ring up period comprises 3 cycles. An example of measured pressure waveform is shown in Figure 4-3a. The effect of axial focus steering on the pressure is illustrated in Figure 4-3b, where the ratio of the peak negative

pressure level relative to that at the geometric focus (90mm) ranges from about 1.06 at 80 mm to 0.88 at 100 mm.

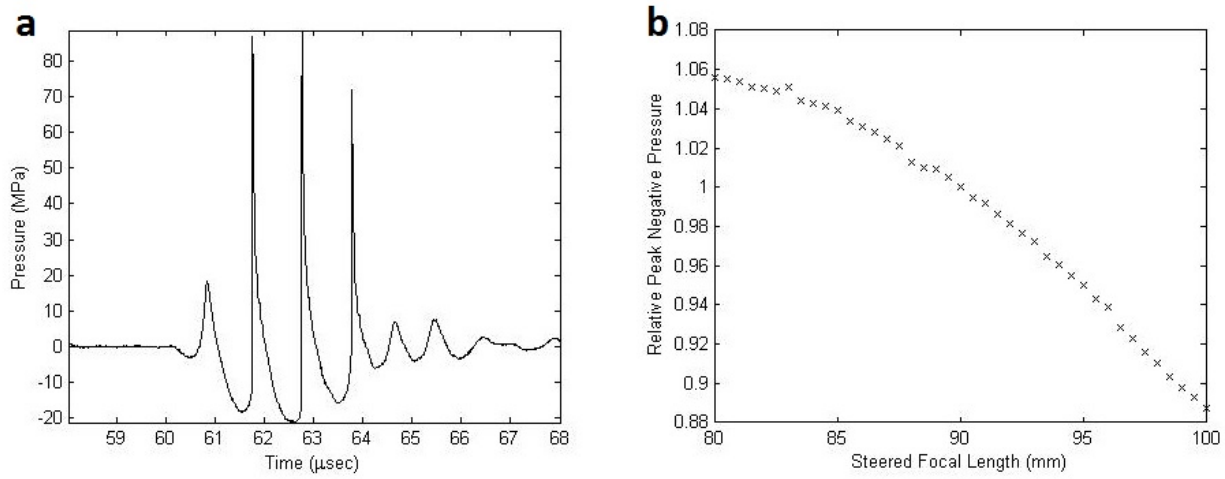

Figure 4-3: Pressure calibration plots for the therapy transducer. a) Pressure waveform for a 3-cycle pulse at the output pressure level used *in vitro* and measured at the geometric focus (90 mm). b) Peak negative pressure over the axial steering range relative to that at the geometric focus.

4.2.2 *In Vitro* Tissue Phantom Validation

This integrated histotripsy therapy system was then tested in three *in vitro* scenarios using tissue mimicking gel phantoms to measure the impact of the motion tracking algorithm on the accuracy and efficiency of histotripsy therapy. First, to evaluate the accuracy at different tracking velocities, the target position estimates from the algorithm were compared to the position of the target measured from optical images of the moving target during therapy. The optical images were taken at high resolution (30µm pixel size) with a short exposure (2 µs) to provide an accurate measurement of the target movement. Second, to evaluate the treatment accuracy and collateral damage reduction, the lesion dimensions created in moving phantoms with the tracking algorithm were compared to those produced without tracking. Third, to investigate the efficiency of the system, the erosion rate (defined as the thickness of the phantom

divided by the time required to perforate it) in tissue phantoms treated with the tracking algorithm enabled were compared to those treated without tracking enabled.

System Tracking Accuracy at Different Velocities

To quantify the motion tracking system accuracy, the path of the target was measured by imaging the target phantom location using a high speed camera (Phantom V210, Vision Research Inc., Wayne, NJ, USA). High resolution images of the target phantom's range of motion were captured through a telephoto lens assembly, resulting in a resolution of ~30 microns per pixel. These synchronized images were acquired 60 μsec after the therapy pulse firing to account for the acoustic propagation time. The images were then post-processed to produce the reference target path for error quantification by comparison with the estimated path stored in the therapy controller.

The target was a 0.18 mm diameter nylon line target embedded in a 1% agarose hydrogel inside an acetal housing. This phantom was moved using a Parker XRS positioning system (Parker Hannifin Corp., Mayfield Heights, Ohio, USA) over a 15 mm linear path along the therapy axis with constant acceleration magnitude of 400 mm/s2 and maximum velocities between 10 and 80 mm/s to test the upper limits of the tracking capabilities of the algorithm. Varying the pulse duration and pulse repetition frequency (PRF) over the typical histotripsy therapy ranges had no effect on the motion tracking frame rate, and therefore accuracy was tested only for a single pulse duration and PRF in this study. Histotripsy was delivered using 5 cycle pulse duration and 500 Hz PRF for 10 seconds at each of the tested velocities. The estimated path was downloaded after each experiment from the FPGA board. The difference between the estimated path and path recorded from the high speed images was computed as the tracking error.

System Treatment Accuracy – Lesion Size

To quantify the treatment accuracy of the system, the sizes of lesions generated in a moving tissue phantom with and without the motion tracking system as well as a stationary control phantom were measured and compared. The phantom was moved along the therapy axis, and histotripsy therapy was applied to the phantom both with and without motion correction. The initial resting position of the line target was aligned with the geometric focus of the therapy transducer. Motion was programmed using the Parker XRS positioning system, with constant acceleration of 60 mm/s2 over displacements of 5, 10, and 15 mm centered at the geometric focus of the therapy transducer. These corresponded to maximum velocities of approximately 24, 34, and 42 mm/s respectively. We could not reliably secure the gel phantom at higher accelerations and velocities because the phantom would slide out of its housing at higher velocities. The velocities tested here are sufficient to represent the majority of physiological organ motion ranges, and provide complementary data to the raw accuracy assessment described previously. Control experiments were conducted with no phantom motion and the target line placed at the geometric focus.

A tissue-mimicking agarose gel phantom with an embedded red blood cell (RBC) layer was used here to identify the lesion size, because it was shown to produce reliable estimates of the cavitation-induced damage zone. In this phantom, The RBC area lysed by histotripsy changed from opaque red to translucent pink [23], allowing direct visualization and evaluation of the lesion size. In this experiment, a 5% RBC layer in a 1% agarose gel phantom was made using the methods described in the paper. The lesions in the treated phantoms were photographed and post-processed to quantify the length and area of the lesion. The images were segmented using a local intensity threshold to distinguish the lighter treated lesion areas from the darker, intact red

blood cells surrounding the lesions. The length and area of the lesions generated with and without motion tracking were computed and normalized by the length and area of the corresponding control lesion to allow fair comparison between samples. The methods to segment the lesion and calculate the length and area of the lesion are detailed in [23].

In this experiment series, a line target was embedded perpendicular to the RBC layer to provide a distinguishable target in the otherwise acoustically uniform gel phantom. Histotripsy pulses at 10 cycle duration and 50 Hz PRF were applied for 2 minutes. This parameter combination was used because it has achieved effective fractionation in RBC phantoms in previous experiments [23].

System Treatment Efficiency – Erosion Rate

To evaluate the efficiency of the integrated system, the rate at which a moving gel phantom layer was perforated (erosion rate) using histotripsy with and without tracking was measured and compared (sample size = 3). To mimic an *in vivo* scenario where the perforation in the atrial or ventricular septum in the heart was generated using histotripsy a mobile tissue membrane phantom between two fluid chambers was developed. Agarose gel at 2.5% concentration by weight was formed into discs roughly 3-4 mm thick and 30 mm in diameter, with graphite embedded in the gel at 2% concentration to provide both ultrasound speckle and visualization of lesion generation. The gel disc was adhered over the center hole of a latex membrane sealing the top of a hollow cylindrical chamber (Figure 4-4), allowing direct fluid access on both sides of the gel disc. A pulsatile pump (Model 1423, Harvard Apparatus, Holliston, MA) was linked to the chamber to pump water into and out of the sealed cylinder, displacing the gel phantom, mimicking the *in vivo* cardiac tissue motion. The displacement and velocity could be tuned by adjusting the stroke volume and stroke rate of the pump, resulting in

movement strictly along the therapy axis between 3 and 12.5 mm at speeds up to 60 mm/s. Movements of 3, 5, 7, 10 and 12.5 mm at a maximum velocity of 40 mm/s were used.

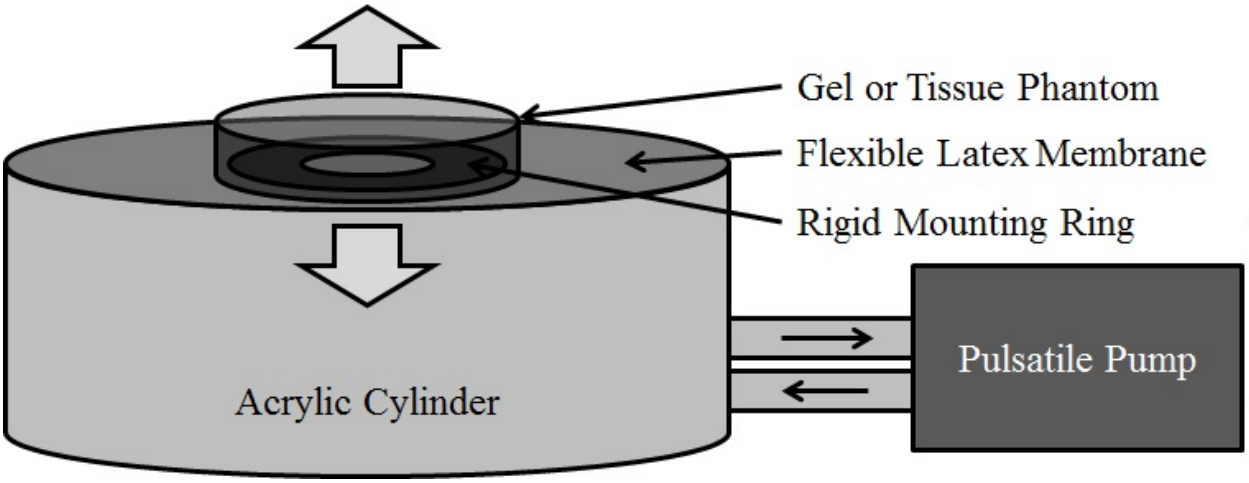

Figure 4-4: Diagram of the phantom apparatus used to evaluate erosion rates. Water was pumped into and out of an acrylic cylinder, flexing the latex membrane top, creating motion along the axis of the cylinder. A gel or tissue sample was adhered over the center hole of a rigid mounting ring in the center of the latex top.

To quantify erosion rate, the phantoms were treated with 5 cycle histotripsy pulses at 1 kHz PRF to mechanically erode the proximal surface of the gel phantom, expelling the fractionated gel and graphite fragments into the surrounding liquid, eroding a visible flow channel through the phantom. These parameters were chosen as they have been used to successfully generate perforation in the atrial or ventricular septum in the heart in our previous *in vivo* studies [3, 4]. The erosion rate was computed as the thickness of the gel membrane phantom divided by treatment time required to create a visible channel through the opaque gel phantom. Control experiments were performed with the same setup with no phantom motion. The erosion rates produced with and without motion correction were compared at identical displacements.

4.2.3 Ex Vivo Tissue Validation

To validate the *in vitro* erosion rate results, a proof of concept experiment was conducted with excised porcine atrial wall tissue. The tissue was harvested from fresh porcine hearts obtained from a local supplier on the day of the experiment. Four samples of approximately 10 by 20 mm were mounted to the same apparatus as the *in vitro* erosion rate experiment (Figure 4-4), with the pump stroke volume set to achieve a maximum motion displacement of 10 mm. Three locations (separated by 8 mm laterally) on each tissue sample were exposed to 5 cycle histotripsy pulses at 1 kHz PRF. Three scenarios were tested: control with no motion, motion without tracking, and motion with tracking. Histotripsy therapy was applied until perforation was achieved, with the treatment time and resulting erosion rate recorded.

4.2.4 *In Vivo* Validation

The procedures described here were reviewed and approved by the University Committee on Use and Care of Animals at the University of Michigan (UCUCA). For *in vivo* proof of feasibility, the system was tested on tracking and treating the atrial septum in a single animal open-chest canine heart model. Although the ultimate clinical application would be non-invasive (either transcostal or subcostal acoustic windows) and not require surgery, this animal model and setup were used previously [2] for atrial septal defect (ASD) creation (perforation through the atrial septum) using histotripsy and was suitable to test the motion tracking system. A motion range (5.2 to 17.1 mm axial displacement) was observed previously for the atrial septum. Therapy access to the heart was achieved through a midline sternotomy with retraction of the ribcage. The lungs were retracted laterally to prevent interference with ultrasound propagation and the pericardium was left intact. A temperature-controlled, degassed water bath enclosed in a thin

plastic bag was coupled to the pericardium with ultrasound gel. The coaxially mounted imaging and therapy transducers were submerged in the water bath outside the heart, and positioned under ultrasound guidance to center the geometric focus of the transducer over the approximate center of the atrial septum's motion path. A reference image of the atrial septum was acquired prior to the histotripsy therapy and used to set up initial motion tracking parameters. After the motion tracking algorithm and parameters were tuned, histotripsy pulses of 5 cycles at 1 kHz PRF were applied for 10 exposures at 3 different locations on the front, middle and back of the atrial septum, totaling 24 minutes of therapy.

4.3 Results

4.3.1 Motion Tracking System Performance

The integrated motion correcting histotripsy therapy system achieved a maximum frame rate of 62 Hz. The system is capable of tracking targets up to the highest velocity (80 mm/s) and highest acceleration (400 mm/s^2) tested. The status of the motion tracking was monitored by the operator in real-time through an overlay of the estimated target position on the ultrasound image. In two cases of the 15 erosion rate trials, and in three of 10 individual treatments in the *in vivo* study, the system encountered significant out-of-plane motion, imaging artifacts or other anomalies resulting in a loss of target tracking, in which cases the operator immediately halted therapy and reset the tracking to the intended target.

4.3.2 *In Vitro* Tissue Phantom Validation

System Accuracy vs. Tracking Velocity

Estimated paths from the motion tracking system and the measured paths taken from the high speed camera were collected at 500 Hz PRF therapy at a fixed acceleration magnitude of 400 mm/s^2 and velocities between 10 and 80 mm/s. The root mean squared (RMS) and maximum error between the two paths over 10 second captures for each scenario is presented in Table 1. The RMS accuracy for the motion tracking system over the tested velocity range was 0.52 mm, which is very close to the 0.5 mm step size of the therapy focus steering.

Table 4-1: RMS and Maximum Error versus Velocity

Maximum Velocity (mm/s)	Error (mm)	
	RMS	Maximum
10	0.25	0.65
20	0.31	1.05
30	0.41	1.74
40	0.51	1.75
50	0.58	2.18
60	0.63	2.04
70	0.64	2.26
80	0.66	2.96

An example plot of the estimated path versus the measured path is shown in Figure 4-5 for two velocity scenarios. At lower velocities error is dominated by the steering step size, as the transducer was only programed with foci at 0.5 mm separations, producing an RMS error less than 0.51 mm. This focal step size could be arbitrarily decreased to reduce this source of error, however this was not practically necessary since 0.5 mm is already small compared to the bubble cloud's axial extent (25 mm). At higher velocities, the error is above the 0.5 mm step size with RMS error up to 0.66 mm at 80 mm/s velocity, with the estimated position trailing the actual path in time. At these high velocities, the motion during the algorithm processing time latency (averaging 16 ms) between image acquisition and the resulting focal update becomes substantial, increasing tracking error.

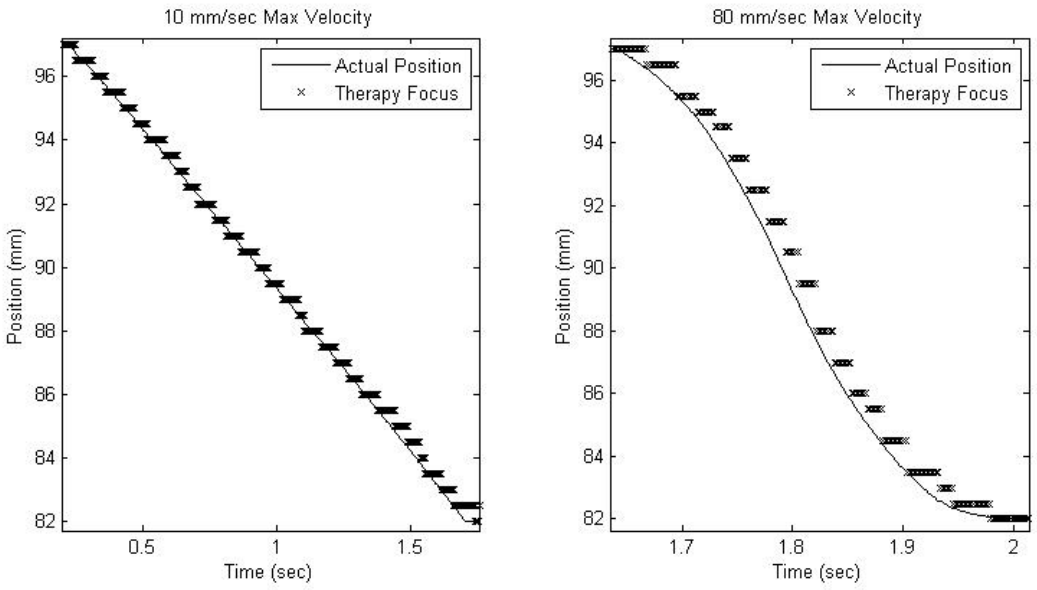

Figure 4-5: Plots of the estimated and actual motion paths for velocities of 10 and 80 mm/s.

System Accuracy - Lesion Size

The area and length of the lesions created by the histotripsy system in a moving gel phantom with and without using motion correction were measured. Lesion area and length data were collected for 3 samples at each of the displacements 5, 10, and 15 mm. The lesion images were segmented using local pixel intensity thresholds; an example image before and after segmentation is shown in Figure 4-6.

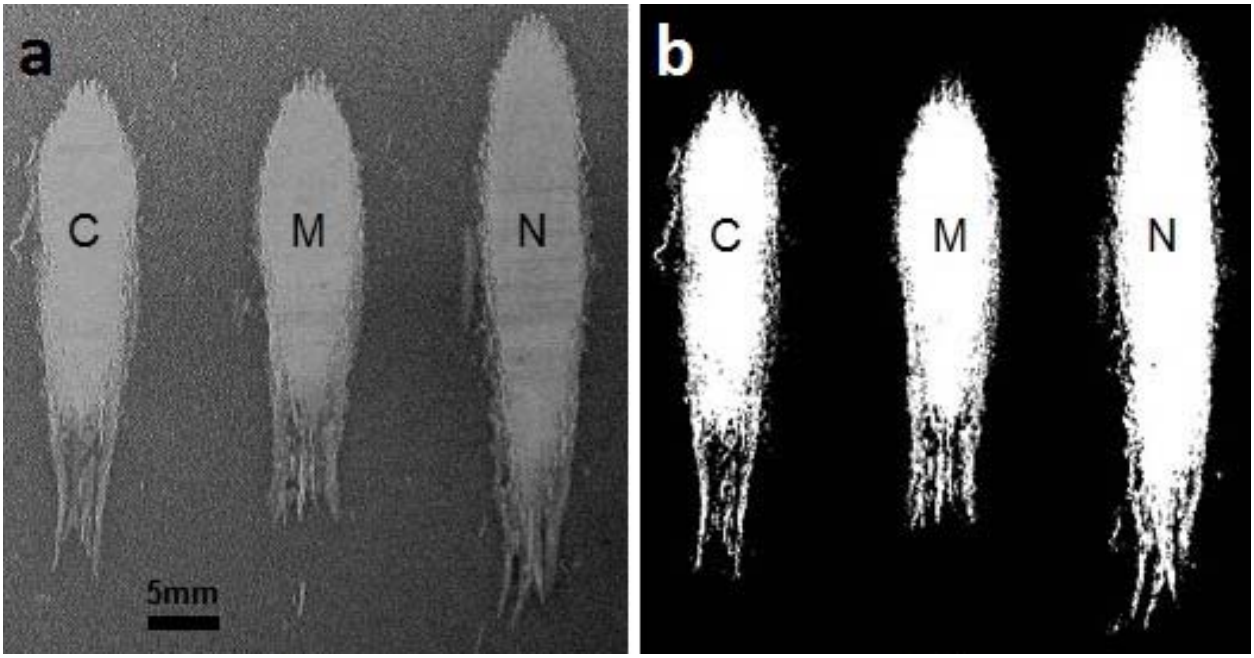

Figure 4-6: Lesion images before (a) and after (b) threshold image segmentation revealing, from left to right, control (C), motion tracking (M) and no tracking (N) lesions for a displacement of 5 mm.

From these segmented images, the area and length of motion tracking and no tracking lesions were computed as percentages of the dimensions relative to their corresponding control lesion (Figure 4-7). The area and length of the lesions generated in the moving targets using motion tracking were comparable to those generated with stationary targets. The mean percentages of the lesion areas with respect to the control lesion were 93.0%, 100.0% and 92.0% using motion tracking at displacements of 5, 10 and 15 mm, respectively. Similarly, the mean percentages of the lesion lengths with respect to the control lesion were 99.2%, 100.0% and 88.8% using motion tracking at displacements of 5, 10 and 15 mm, respectively. In comparison, the lesions generated without motion tracking were significantly larger, and the total lesion area and length increased with increasing displacement. The mean percentages of the lesion areas with respect to the control lesion were 128.5%, 166.5% and 194.1% without motion tracking at

displacements of 5, 10 and 15 mm, respectively. The mean percentages of the lesion lengths with respect to the control lesion were 137.9%, 166.7% and 197.6% without motion tracking at displacements of 5, 10 and 15 mm, respectively. The t-tests revealed that both the lesion area and length without motion tracking are significantly larger than their corresponding control lesion ($p < 0.05$), whereas lesion area and length with motion tracking are not significantly larger than their corresponding control lesion ($p > 0.3$).

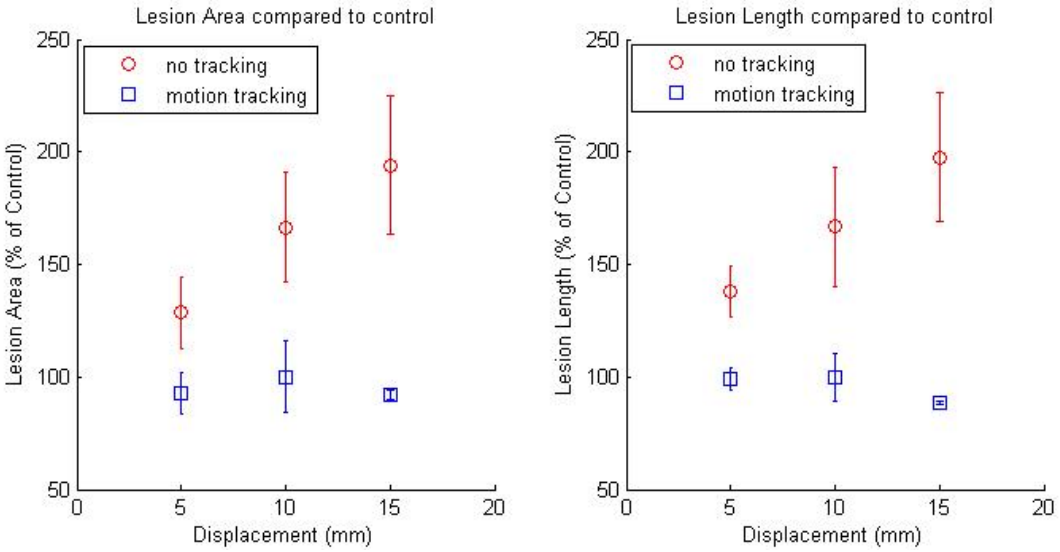

Figure 4-7: Lesion area and length compared with control (% of control) versus target displacement for lesions generated with motion tracking (square) and without motion tracking (diamond).

System efficiency - Erosion Rate

The erosion rate of a 2.5% agarose hydrogel membrane phantom was computed for each of the motion displacements 3, 5, 7.5, 10, and 12.5 mm with and without motion tracking (N = 3). Control experiments were conducted without motion (N = 3) resulting in an erosion rate of 3.03±0.14 mm/min, representing the maximum erosion rate for this scenario. A plot of erosion rate versus motion range is presented in Figure 4-8. A two-sample t-test shows that the erosion rate with motion tracking was significantly higher than the erosion rate without motion tracking

($p < 0.05$) for all displacements. Erosion rate with tracking for all displacements averaged 2.7±0.29 mm/min, or approximately 89.0% of the control rate ($p < 0.05$). Without tracking, erosion rate was substantially reduced to between 1.8±0.07 mm/min for the 3 mm displacement (61.6% of the control rate) and 0.91±0.14 mm/min for the 12.5 mm displacement (30.0% of the control rate) ($p < 0.05$). Differences in erosion rate among the individual displacements for the motion tracking case were not significant ($p > 0.05$), except between the 3 mm and 7.5 mm displacements ($p = 0.03$) due to a low observed variance in those specific samples.

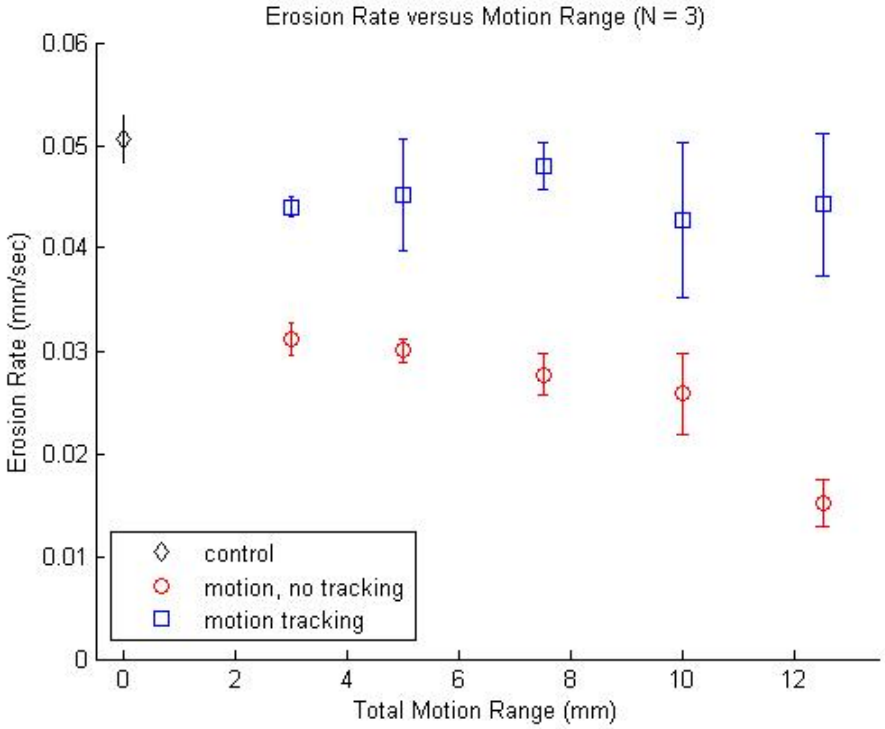

Figure 4-8: Erosion rate versus target phantom displacement for control without motion (diamond), motion tracking with motion (square) and no motion tracking with motion (circle). (N = 3).

4.3.3 Ex Vivo Tissue Validation Results

Erosion rate in *ex vivo* atrial wall tissue was measured for a 10 mm motion range (N = 4). An erosion rate of 4.51±0.89 mm/min was achieved for the control case (stationary target).

Erosion rate with motion tracking was measured at 4.40±0.82 mm/min which was comparable to the control rate, ($p = 0.86$; t-test; 97% of control rate). Erosion rate without motion tracking was measured at 1.90±0.39 mm/min or 42% of the control rate, which was significantly lower than both the control and motion tracking rates ($p < 0.01$; t-test).

4.3.4 *In Vivo* Feasibility Results

In the *in vivo* experiment, the motion tracking system successfully tracked the motion of the atrial septum in the live beating canine heart at 3 separate locations. The atrial septum was observed to move over a maximum displacement of 8 mm due to the 14.1±2.1 breaths per minute respiration and 116.6±11.0 beats per minute heart rate. A frame rate of 32.6±5.6 Hz was achieved for accurate motion tracking, which was lower than that in the *in vitro* case due to the increased imaging time required for the 5 steered plane wave acquisitions needed to improve imaging quality. An excerpt of the estimated target path recorded during treatment is plotted in Figure 4-9. The path shows the expected short, quick movements of the septum from cardiac motion added with the larger, slower movements from respiration. 10 treatments totaling 24 minutes of therapy were applied to the septum, generating a targeted lesion on the atrial septum as shown by ultrasound in Figure 4-10. Since this was a procedural feasibility study, the animal was euthanized immediately following therapy. Histological confirmation of a lesion created by histotripsy is shown in the Hematoxylin and Eosin (H&E) stained slide of the treated atrial septum (Figure 4-11). Distinctive borders of injury and slight areas of flanking hemorrhage at the boundary were observed. Wound healing and long-term effects of therapy could not be evaluated with this study.

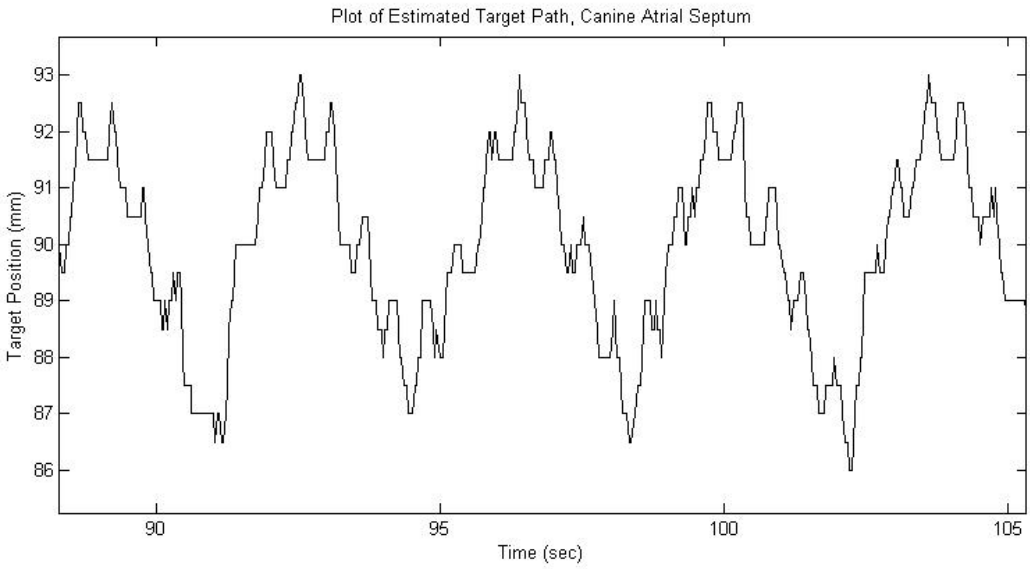

Figure 4-9: Plot of the estimated axial position of the target on the canine atrial septum during treatment.

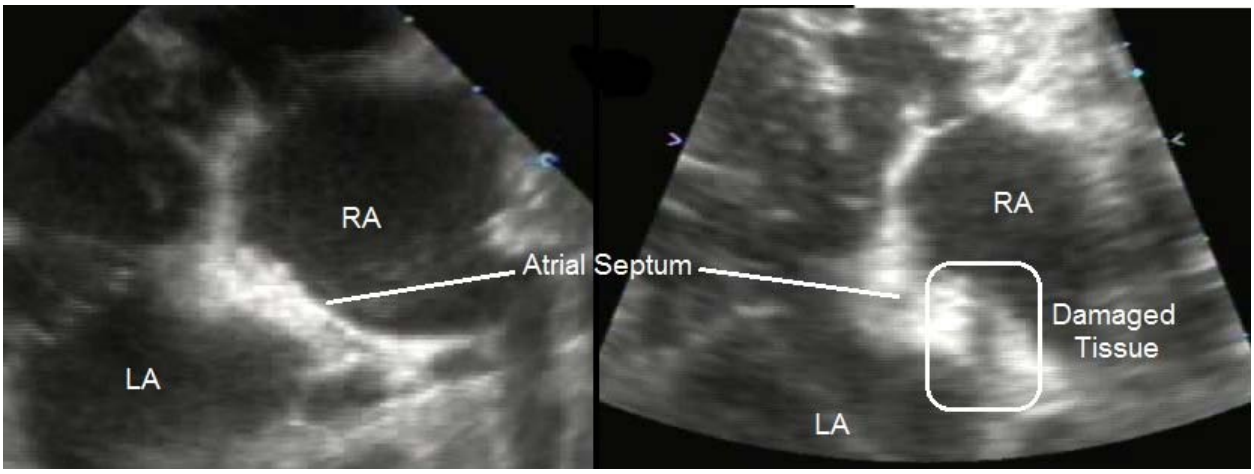

Figure 4-10: Ultrasound images of the atrial septum before therapy (left) and after therapy (right) showing significantly reduced echogenicity across the treated region of the atrial septum, corresponding to regions of damaged or removed tissue. LA = left atrium; RA = right atrium.

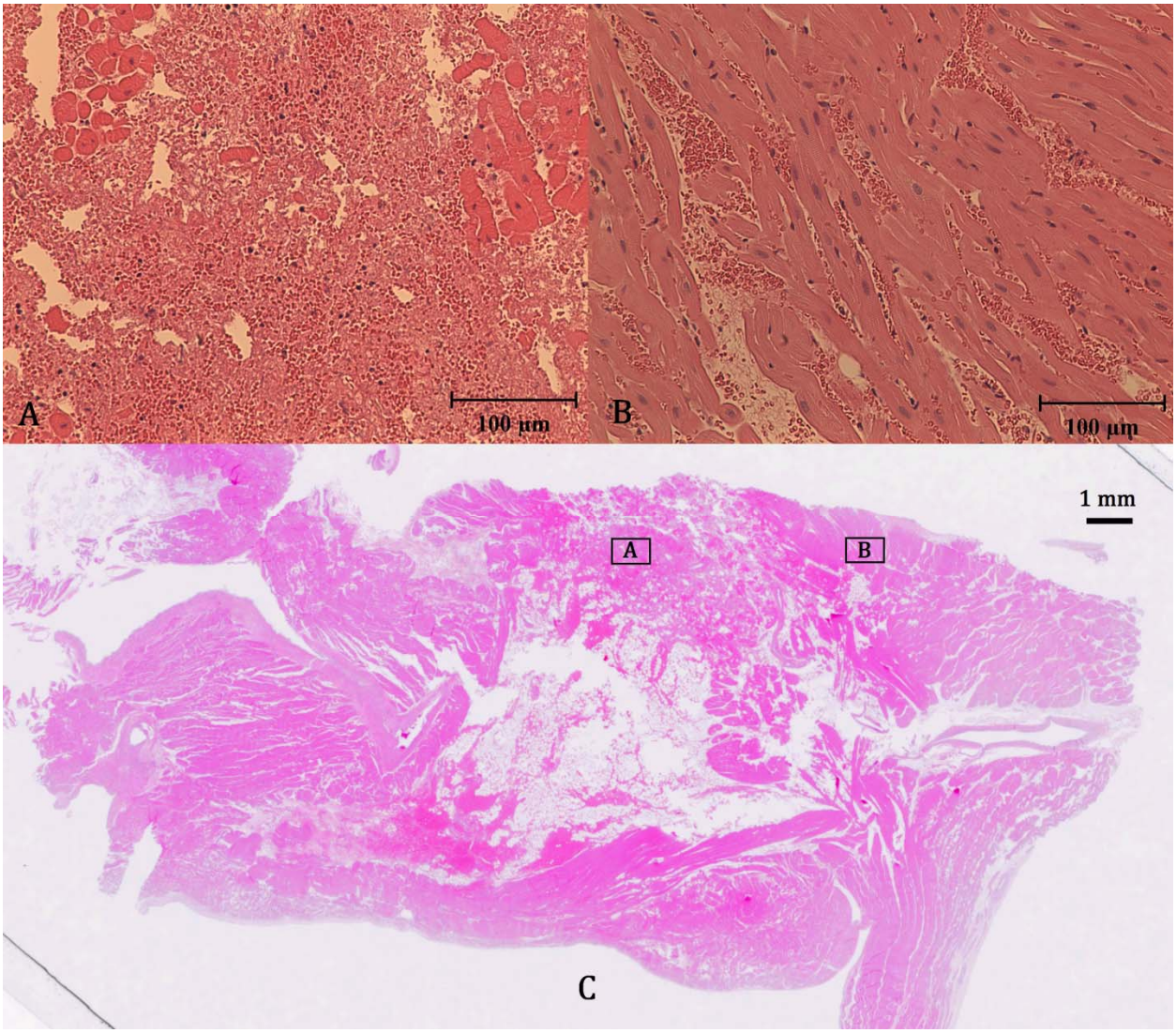

Figure 4-11: Hematoxylin and eosin-stained slide of treated atrial septum (C) along with close-up images of the fractionated region (A) and surrounding untreated region (B).

4.4 Discussion

The main advantage of the system developed here over previously developed ultrasound therapy system with motion correction is that it requires no specialized hardware for implementation. To implement a system similar to the successful motion correcting ultrasound therapy systems demonstrated previously [8, 9], a 2D phased array therapy system with both transmit and receive capabilities would have to be developed along with corresponding multi-

channel data-acquisition hardware. Similar to another recently developed motion correction system [10] our integrated therapy motion correction utilized ultrasound images directly for target motion tracking. The optical flow techniques from that work are aimed at slower moving abdominal organs, and the resulting lower frame rates (8 Hz) are likely not sufficient for high speed cardiac motion. Another advantage of reference image or landmark based tracking methods like these is that they allow the flexibility to utilize image features that are arbitrarily shaped and positioned, and avoids the risk of error compounding over time inherent in relative motion tracking methods. For example, frame to frame speckle tracking methods can allow small estimation errors from each frame to compound over time, potentially degrading accuracy over time as the tracked location "drifts". Our method uses a single reference image for all motion estimates, where the reference feature is either found and the system remains accurate, or an easy to identify tracking error occurs, and therapy can be halted. If the tracked feature is within the treated volume, however, the reference image will need to be recaptured as the treatment progresses, as the appearance of the reference will change when that volume is fractionation by histotripsy.

The current system is not without limitations. In this study, the algorithm tracks the motion in 2D based on ultrasound images, while therapy focus steering is only performed in the axial dimension. This limited dimensionality is useful for correcting the motion encountered in the neonatal and fetal cardiac applications that we are currently investigating, where the only significant motion is along the therapy axis. However, future applications in the adult heart will likely require 3D motion correction. Extensions of the key components of our system (diamond search, SAD criterion, and Kalman filtering) to a 3D motion correction system are straightforward with the use of 3D ultrasound data or two orthogonal 2D image planes. Though

computational complexity is the major concern for the extension of the block matching method, it potentially can be mitigated with appropriate choices of imaging field of view, reference block size, and search procedure. For example, a potential 3D Diamond Search pattern would only require 19/6 test points in LDSP/SDSP versus the current 9/4 in 2D. Furthermore, processing hardware upgrades and computation parallelization may potentially offset these additional requirements, and we anticipate sufficiently high maximal tracking velocity can be achieved for cardiac therapy. Other 3D ultrasound motion tracking methods have been demonstrated [24, 25], and will be evaluated as potential alternatives to the proposed block matching estimation for improved tracking of the non-rigid motion of heart structures. With these improvements, the system's performance could be more directly compared with previous work on 3D motion correction for ultrasound therapy and evaluated for its utility in high speed targets for cardiac therapy.

Other improvements, intended to enhance clinical applicability and ease of use, include automatically halting therapy when tracking is lost, as detected by the SAD metric dropping below a threshold value. Also, as the cavitation bubble cloud is the effective "scalpel" in histotripsy treatment, an algorithm incorporating simultaneous bubble cloud tracking will help evaluate the effectiveness and accuracy of the motion tracking during histotripsy therapy. More precise adjustments could then be made based on this feedback to further improve the therapy efficiency and accuracy if necessary.

The in vivo experiment used an open-chest adult canine model, which provided cardiac motion for our feasibility study. Our current goal is to implement the motion tracking method for pediatric cardiac applications, including perforation of the atrial septum in the neonatal patients with hypoplastic left heart syndrome (HLHS). In these pediatric patients, a subcostal acoustic

window exists to access the atrial setup without lung or rib obstruction. Unfortunately this acoustic window does not exist in non-primate animals, as their heart orientation is different from humans. We have utilized transthoracic histotripsy to create cardiac lesions in neonatal animal models, but partial lung and rib obstruction was encountered [3, 4]. Even though histotripsy has been shown to be able to generate precise lesions through ribs without aberration correction [26], the lungs full of air in the ultrasound pathway still pose a serious problem. Therefore, to access the atrial septum, an open-chest surgery was performed in this initial feasibility study. In the future, we plan to augment the animal model to create access to the atrial septum through an intact chest (e.g., by filling the lung with fluid), which will allow us to test non-invasive histotripsy cardiac therapy integrated with motion tracking without the need to perform open-chest surgery. In addition, to further improve the imaging quality, we also plan to redesign our therapy transducer to allow the imager to be directly placed on to the patient's skin to avoid imaging quality degradation caused by stand-off distance between the imager and the skin. With all these improvements, this motion tracking system can be a valuable tool for histotripsy therapy on moving targets, such as cardiac applications to create intra-cardiac communications in infants with congenital heart disease or the removal of excess myocardial tissue such as that found in adult patients with hypertrophic cardiomyopathy.

4.5 Conclusion

This study has been our first attempt to integrate a motion correction scheme into a histotripsy system to track the motion of a cardiac target during histotripsy therapy. Our results indicate that the block matching method using diamond search algorithm and Kalman filtering is capable of tracking fast motion with high accuracy. When treating a moving target *in vitro*,

significant improvement in therapy accuracy and efficiency was achieved compared to therapy without using the algorithm. Though *in vitro* testing phantoms could not produce the non-rigid motion present in the heart, feasibility was evaluated in a live beating heart *in vivo* with further work necessary to quantitatively evaluate the system performance in this setting and adapt the system for non-invasive therapy.

4.6 References

[1] R. M. Miller, Y. Kim, K.-W. Lin, C. A. Cain, G. E. Owens, and Z. Xu, "Histotripsy Cardiac Therapy System Integrated with Real-Time Motion Correction," *Ultrasound in Medicine & Biology,* vol. 39, pp. 2362-2373, 2013.

[2] Z. Xu, G. Owens, D. Gordon, C. A. Cain, and A. Ludomirsky, "Noninvasive Creation of an Atrial Septal Defect by Histotripsy in a Canine Model," *Circulation,* vol. 121, pp. 742-749, February 2010.

[3] G. Owens, R. Miller, S. Owens, S. Swanson, K. Ives, G. Ensing, D. Gordon, and Z. Xu, "Intermediate-Term Effects of Intracardiac Communications Created Noninvasively by Therapeutic Ultrasound (Histotripsy) in a Porcine Model," *Pediatric Cardiology,* vol. 33, pp. 83-89, 2012/01/01 2012.

[4] G. E. Owens, R. M. Miller, G. Ensing, K. Ives, D. Gordon, A. Ludomirsky, and Z. Xu, "Therapeutic ultrasound to noninvasively create intracardiac communications in an intact animal model," *Catheterization and Cardiovascular Interventions,* vol. 77, pp. 580-588, 2011.

[5] Y. Kim, S. K. Gelehrter, C. G. Fifer, J. C. Lu, G. E. Owens, D. R. Berman, J. Williams, J. E. Wilkinson, K. A. Ives, and Z. Xu, "Non-invasive pulsed cavitational ultrasound for fetal tissue ablation: feasibility study in a fetal sheep model," *Ultrasound Obstet Gynecol,* vol. 37, pp. 450-7, Apr 2011.

[6] H. D. Kubo and B. C. Hill, "Respiration gated radiotherapy treatment: a technical study," *Phys Med Biol,* vol. 41, pp. 83-91, Jan 1996.

[7] S. A. Strickberger, T. Tokano, J.-U. A. Kluiwstra, F. Morady, and C. A. Cain, "Extracardiac Ablation of the Canine Atrioventricular Junction by Use of High-Intensity Focused Ultrasound," *Circulation,* vol. 100, pp. 203-208, July 1999.

[8] F. Marquet, J. F. Aubry, M. Pernot, M. Fink, and M. Tanter, "Optimal transcostal high-intensity focused ultrasound with combined real-time 3D movement tracking and correction," *Physics in Medicine and Biology,* vol. 56, pp. 7061-7080, November 2011.

[9] M. Pernot, M. Tanter, and M. Fink, "3-D Real-time Motion Correction in High-Intensity Focused Ultrasound Therapy," *Ultrasound in Medicine and Biology,* vol. 30, pp. 1239-1249, September 2004.

[10] V. Auboiroux, L. Petrusca, M. Viallon, T. Goget, C. D. Becker, and R. Salomir, "Ultrasonography-based 2D motion-compensated HIFU sonication integrated with reference-free MR temperature monitoring: a feasibility study ex vivo.," vol. 57, 2012.

[11] P. Arnold, F. Preiswerk, B. Fasel, R. Salomir, K. Scheffler, and P. Cattin, "3D Organ Motion Prediction for MR-guided High Intensity Focused Ultrasound," *Medical Image Computing and Computer-Assisted Intervention,* vol. 14, pp. 623-630, 2011.

[12] B. D. de Senneville, C. Mougenot, and C. T. Moonen, "Real-time adaptive methods for treatment of mobile organs by MRI-controlled high-intensity focused ultrasound," *Magn Reson Med,* vol. 57, pp. 319-30, Feb 2007.

[13] B. D. de Senneville, M. Ries, G. Maclair, and C. Moonen, "MR-Guided Thermotherapy of Abdominal Organ Using a Robust PCA-Based Motion Descriptor," *IEEE Transactions on Medical Imaging,* vol. 30, pp. 1987-1995, November 2011.

[14] B. D. de Senneville, S. Roujol, C. Moonen, and M. Ries, "Motion Correction in MR Thermometry of Abdominal Organs: a Comparison of the Referenceless vs. the Multibaseline Approach," *Magnetic Resonance in Medicine,* vol. 64, pp. 1373-1381, November 2010.

[15] M. Ries, B. D. de Senneville, S. Roujol, Y. Berber, B. Quesson, and C. Moonen, "Real-time 3D target tracking in MRI guided focused ultrasound ablations in moving tissues," *Magn Reson Med,* vol. 64, pp. 1704-12, Dec 2010.

[16] G. Jacob, J. A. Noble, C. Behrenbruch, A. D. Kelion, and A. P. Banning, "A shape-space-based approach to tracking myocardial borders and quantifying regional left-ventricular function applied in echocardiography," *IEEE Trans Med Imaging,* vol. 21, pp. 226-38, Mar 2002.

[17] J. D'Hooge, E. Konofagou, F. Jamal, A. Heimdal, L. Barrios, B. Bijnens, J. Thoen, F. Van de Werf, G. Sutherland, and P. Suetens, "Two-dimensional ultrasonic strain rate measurement of the human heart in vivo," *IEEE Trans Ultrason Ferroelectr Freq Control,* vol. 49, pp. 281-6, Feb 2002.

[18] M. J. Ledesma-Carbayo, J. Kybic, M. Desco, A. Santos, M. Suhling, P. Hunziker, and M. Unser, "Spatio-temporal nonrigid registration for ultrasound cardiac motion estimation," *IEEE Trans Med Imaging,* vol. 24, pp. 1113-26, Sep 2005.

[19] M. Suhling, M. Arigovindan, C. Jansen, P. Hunziker, and M. Unser, "Myocardial motion analysis from B-mode echocardiograms," *IEEE Trans Image Process,* vol. 14, pp. 525-36, Apr 2005.

[20] J. Kuo and O. T. von Ramm, "Three-dimensional motion measurements using feature tracking," *IEEE Trans Ultrason Ferroelectr Freq Control,* vol. 55, pp. 800-10, Apr 2008.

[21] S. Zhu and K.-K. Ma, "A New Diamond Search Algorithm for Fast Block-Matching Motion Estimation," *IEEE Transactions on Image Processing,* vol. 9, pp. 287-290, February 2000.

[22] J. E. Parsons, C. A. Cain, and J. B. Fowlkes, "Cost-effective Assembly of a Basic Fiber-optic Hydrophone for measurement of High-Amplitude Therapeutic Ultrasound Fields," *Journal of the Acoustical Society of America,* vol. 119, pp. 1432-1440, March 2006.

[23] A. D. Maxwell, T. Y. Wang, L. Yuan, A. P. Duryea, Z. Xu, and C. A. Cain, "A tissue phantom for visualization and measurement of ultrasound-induced cavitation damage," *Ultrasound Med Biol,* vol. 36, pp. 2132-43, Dec 2010.

[24] M. A. Bell, B. C. Byram, E. J. Harris, P. M. Evans, and J. C. Bamber, "In vivo liver tracking with a high volume rate 4D ultrasound scanner and a 2D matrix array probe," *Phys Med Biol,* vol. 57, pp. 1359-74, Mar 7 2012.

[25] E. J. Harris, N. R. Miller, J. C. Bamber, P. M. Evans, and J. R. Symonds-Tayler, "Performance of ultrasound based measurement of 3D displacement using a curvilinear probe for organ motion tracking," *Phys Med Biol,* vol. 52, pp. 5683-703, Sep 21 2007.

[26] Y. Kim, T.-Y. Wang, Z. Xu, and C. A. Cain, "Lesion Generation Through Ribs Using Histotripsy Therapy Without Abherration Correction," *IEEE Transactions on Ultrasonics, Ferroelectrics, and Frequency Control,* vol. 58, pp. 2344-2343, November 2011.

Chapter 5
Bubble-induced Color Doppler Feedback for Histotripsy Tissue Fractionation

A majority component of this chapter is excerpted from a manuscript that is being prepared for *IEEE Transactions on Ultrasonics, Ferroelectric, and Frequency Control*.

5.1 Introduction

Real-time imaging feedback during minimally invasive or non-invasive ablation therapy is essential for ensuring efficient and thorough treatment of the target tissue. The fractionation induced by histotripsy appears as a hypo-echoic zone on B-mode ultrasound images, resulting from the backscatter amplitude reduction due to reduced number and size of scatters [1]. Although this is only observed when substantial tissue fractionation is generated, and the level of reduction corresponding to treatment completion varies significantly across subjects. [2]. Magnetic resonance (MR) imaging has also been investigated and histotripsy lesions can be shown on standard T1- or T2- weighted images [3]. MR is sensitive to histotripsy-induced tissue damage, where T2-weighted images can detect apparent changes after only a few therapy pulses have been applied. The high cost of MR imaging systems, the slower frame rate, and the requirement for MR compatible ultrasound therapy transducers are potential limiting factors. Elastography has also been explored to monitor histotripsy therapy, as histotripsy fractionation results in increasingly softer tissue. With comparatively low cost and ease of integration,

ultrasound elastography [4-9] is an attractive choice for histotripsy feedback. Ultrasound elastography has been widely investigated for tissue delineation because the high contrast in the elasticity between normal and diseased tissues allows higher specificity and sensitivity for disease diagnosis [10-12]. Wang et al.'s work has demonstrated shear wave elastography is more sensitive at detecting early-stage histotripsy fractionation compared to echogenicity decrease [13]. However, in that work, to measure a shear wave velocity reliably, the treatment needs to be halted temporally to allow the application of additional push pulses and the measurements of shear wave velocity.

Color Doppler imaging, synchronized with histotripsy pulses has been observed to detect motion in the focal volume during the time immediately after the therapy pulse arrives at the focus (Figure 5-1). The velocity detected at a fixed delay after the therapy pulses was observed to change in magnitude and even direction over the course of histotripsy therapy.

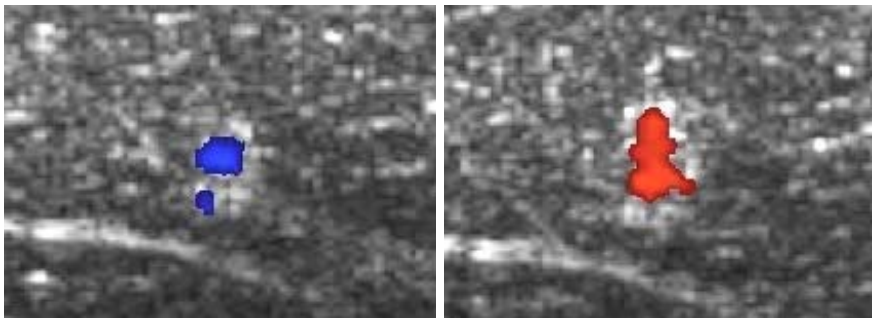

Figure 5-1: Color Doppler overlaid on B-mode images during a histotripsy treatment of ex vivo porcine liver. Doppler velocity was observed to transition from towards the therapy transducer at the start of treatment (left) to away from the transducer later in the treatment (right) in fixed delay, synchronized color Doppler imaging.

This motion is only detectable when a cavitation bubble cloud is formed, and therefore we have termed it bubble-induced motion. This motion can last over 20 ms after each histotripsy pulse. The motion itself likely results from some net force exerted by rapid bubble expansion or

collapse in the focal region, though the precise mechanism(s) that cause it are not clear. This force generates a variable motion response depending on mechanical properties of the tissue in the focal region. This is similar to the dynamic stress applied in some forms of elastography, and could provide similar information about the focal tissue mechanical properties. We hypothesize that direct metrics of the changing motion parameters over the course of histotripsy therapy may be directly correlated with fractionation progression and can be detected by ultrasound color Doppler during the histotripsy treatment. The residual cavitation nuclei can persist for over 100 ms after the cloud collapse and provide strong acoustic scattering for Doppler acquisitions of bubble-induced motion in the treatment focal region.

This chapter investigates the characteristics of metrics gathered from this color Doppler velocity feedback of bubble-induced motion during the histotripsy treatment and correlates them to the degrees of tissue fractionation generated by histotripsy. Three experiments were performed. First, the bubble-induced motion was recorded and characterized using both acoustic and optic methods. The motion in the treatment focal region after each histotripsy therapy pulse was generated in transparent tissue-mimicking agarose phantom and estimated using ultrasound color Doppler and particle image velocimetry (PIV) processing of simultaneous ultrasound and high-speed optical images of the focal region. The profiles of the Doppler and PIV velocity were compared over the course of the entire histotripsy treatment to analyze and characterize the motion. Second, the change in the temporal profile of Doppler velocity of the bubble-induced motion is correlated with the level of fractionation generated in tissue-mimicking phantom over the course of the histotripsy treatment. Finally, the same color Doppler acquisitions were performed in ex vivo porcine liver tissue to validate this correlation in real tissue. To evaluate the potential of using bubble-induced color Doppler feedback for real-time histotripsy monitoring,

we also investigated metrics to quantify the temporal profile of the bubble-induced motion that can be measured and processed during the histotripsy treatment.

5.2 Methods

5.2.1 General Methods

1. Histotripsy Therapy

Histotripsy therapy pulses of 2 cycle pulse duration at > 30 MPa peak negative pressure were applied over a 6mm cube using a 500 kHz phased array transducer built in-house. The transducer is composed of 32 elements with 50 mm diameter mounted confocally on a 15 cm hemispherical shell. The array is driven by a custom-built 32-channel amplifier system that controls the driving amplitude and phase of each individual element. To ensure uniform fractionation over the target volume, 219 focal points at 1 mm separations were treated sequentially at 150 Hz with a single pulse applied at each location. These focal locations were arranged into layers separated by 1 mm in the axial dimension, with alternating layers offset in both lateral dimensions from adjacent layers by half the lateral spacing (Figure 5-2). This treatment strategy provides complete coverage of the treatment area with fewer focal locations and less treatment overlap than a simple rectilinear scan due to the roughly ellipsoidal bubble cloud shape. This process was repeated every 1.5 seconds until all focal locations had been treated with up to 2000 pulses each. Using this pulsing strategy, all 219 foci are treated in parallel, at a constant rate of 0.67 Hz. This pulsing strategy guarantees uniform therapy dose over the treatment volume at all times during treatment.

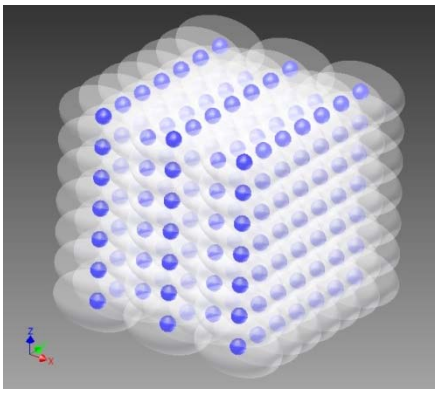

Figure 5-2: Steered focal locations for the 219 foci with 5 alternating 1mm spaced axial layers of 7x7 foci and 6x6 foci. The axial layers are separated by 1mm, but with the 6x6 grids offset from the 7x7 layers by 0.5mm in both lateral dimensions.

2. High Speed Optical Imaging

High speed optical images of the focal region were captured using a Phantom V210 with 135mm macro lens on bellows with backlighting (Vision Research, Wayne, NJ). The camera and backlight were positioned perpendicular to the therapy axis (Figure 5-3). The camera was set to capture either a single image per therapy pulse, or acquisition sets of 200 images at 10 kHz frame rate beginning immediately after the firing of a therapy pulse. For the 200 image per pulse acquisition mode, the internal memory of the camera could not accommodate acquisitions after every therapy pulse, so to facilitate continuous treatment without interruptions for data transfer; acquisition sets were captured after every 10^{th} pulse delivered to the center focal location.

3. Doppler Ultrasound Imaging

Ultrasound Doppler acquisitions were performed using a Verasonics imaging system (Seattle, WA) with a 5 MHz linear imaging transducer (ATL HDI L7-4, Philips, Andover, MA). The imaging transducer was positioned opposite the therapy transducer, aligned along the therapy axis, i.e., the ultrasound imaging beam was rigidly aligned with the therapy beam to avoid the effect of angle variation on Doppler (Figure 5-3). The ultrasound imaging system was

set to capture acquisition sets of 200 Doppler acquisitions at 10 kHz pulse repetition frequency (PRF) rate beginning immediately after the firing of a single therapy pulse. Acquisition sets were captured after every pulse delivered to the center location, and therefore included Doppler acquisitions simultaneous to the optical images acquired after every 10th pulse for direct comparison.

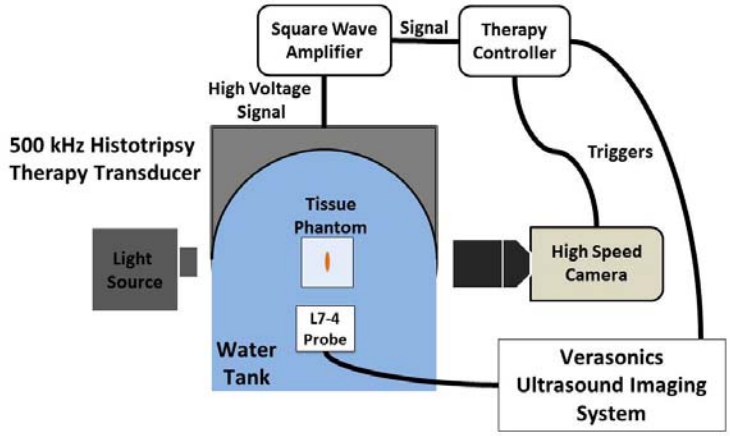

Figure 5-3: Experimental setup with 500 kHz transducer mounted to the side of a water tank with 5 MHz imaging probe mounted opposite the therapy and aligned along the therapy axis. The Phantom high speed camera was positioned perpendicular to the therapy axis.

5.2.2 Experiment 1 – Bubble-induced Motion Characterization using PIV and Doppler

1. Agarose Tissue Phantom Preparation and Treatment

To characterize the bubble-induced motion after each histotripsy pulse through the entire histotripsy treatment, experiments were performed on optically and acoustically transparent agar tissue mimicking phantoms. The purpose of this phantom is to allow simultaneous optical and acoustic interrogation of the focal volume for motion analysis during histotripsy treatment. Agar powder (AG-SP, Lab Scientific, Livingston, NJ) was dissolved in heated distilled water at 1.5% concentration by mass. The solution was then degassed in a vacuum chamber and allowed to cool and solidify in an acrylonitrile butadiene styrene (ABS) plastic housing frame with thin

polycarbonate walls. The phantom was treated at 3 locations with 941 histotripsy pulses using the previously described methods and parameters. These treatments were monitored using the described optical and ultrasound imaging methods for PIV and Doppler velocity estimation. In this experiment, 200 optical images were acquired after every 10th therapy pulse for PIV analysis, and 200 Doppler acquisitions were collected after every therapy pulse, both at 10 kHz frame rate.

2. PIV Velocity Estimation

The high-speed optical images of the focal region were processed using the freely available PIVlab package (1.32) for MATLAB to estimate the motion resulting from the histotripsy therapy pulses. The PIV analysis was performed in a roughly 6.6 × 3.3 mm field of view at a resolution of 116 pixels per mm (total 768 x 384 pixels). The images were processed in pairs at two subsequent time points using a FFT window deformation algorithm with 3 pass velocity estimation with image block sizes and step sizes of 64/32 pixels for pass 1, 32/16 pixels for pass 2, and 16/8 pixels for pass 3. This resulted in velocity field maps of the field of view over the 19 ms after a histotripsy therapy pulse. The axial components of these PIV velocity maps were then spatially averaged over the 2 x 4 mm bubble cloud area, and temporally averaged over a 1 ms rolling window to produce an average velocity estimate in the focal region over time to compare with that measured by color Doppler. As the optical images have higher resolution than the acoustic images, the motion estimated from PIV is considered as the gold standard that we can use to compare with the Doppler Velocity estimation.

3. Doppler Velocity Estimation

The ultrasound Doppler acquisitions were processed offline using the Doppler processing algorithm included in the Verasonics imaging system. To calculate the velocity over the 19 ms

after the therapy pulse, the 200 acquisitions were processed in rolling 10 acquisition segments (equivalent to making 190 separate 10 frame acquisitions at 10 kHz PRF with delay times of integer multiples of 100 ns after each histotrispy pulse). These Doppler velocity maps were then spatially averaged over the 2 x 4 mm bubble cloud area to produce the final average velocity estimate over time. The motion profiles as measured by color Doppler can then be compared to those measured by direct optical interrogation to determine if color Doppler acquisitions can provide an accurate measure of histotripsy bubble cloud induced motion.

From both the PIV and Doppler dataset, a metric was extracted to capture the changes of the temporal profile of the bubble-induced motion over the course of therapy into a single number. PIV and Doppler images observe a coherent motion pushed away from the therapy transducer and rebounded back. The metric used is the time to peak rebound velocity (t_{PRV}), which was computed by calculating the time of the highest magnitude negative velocity after each therapy pulse. This metric was computed from both the PIV and color Doppler velocity measurements for comparison.

5.2.3 Experiment 2 – Correlate Bubble-induced Color Doppler with Histotripsy Tissue Fractionation in Agarose Tissue Phantom

1. Damage-indicating Agarose Phantom Preparation and Treatment

The purpose of this phantom is to include a quantifiable damage indicator of histotripsy tissue fractionation to correlate with a feedback metric extracted from the color Doppler velocity estimations. Tissue-mimicking agarose gel phantoms embedded with a thin layer of red blood cell (RBC) have been shown to produce reliable estimates of the cavitation-induced fractionation, where the RBC area turns from opaque to translucent pink as the RBCs are fractionated and can

be visualized directly during the treatment [14]. To form the 3 layer phantom, agar powder was dissolved in heated, phosphate-buffered saline solution at 1.5% concentration by mass. This solution was degassed and poured to half fill the same ABS housing with thin polycarbonate walls. This was allowed to solidify to form a bottom layer of transparent agarose. Red blood cells were then added to small amount of agarose solution at 5% concentration by mass. This was then poured onto the base layer of transparent agarose in an approximately 1mm thick layer and allowed to solidify. Finally, a top layer of transparent agarose was added to fill the housing and fully contain the RBC layer in a large tissue-mimicking phantom.

The ultrasound imaging and high speed optical imaging setup was identical to the previous experiment, with color Doppler and optical interrogations performed following the therapy pulse delivered to center focal location after each full treatment of the therapy volume. In this case however, only a single optical image was captured per therapy pulse. The phantom was positioned with the RBC layer parallel to the therapy propagation and perpendicular to the high speed imaging to visualize the lesion development over the course of therapy. The phantom was treated at 3 locations with 1000 histotripsy pulses each using the previously described methods and parameters.

2. Fractionation Progress Estimation

From images of this lesion progression, we can create a reference metric of fractionation progression and use it to correlate with the t_{PRV} Doppler feedback metric. To compute this reference metric, an approximately 4mm square region of interest was chosen in the center of the treated region and the average pixel intensity was computed over the treatment course. The red blood cell layer allows more light to pass through as it is increasingly fractionated, eventually becoming completely transparent when all cells in the layer have been destroyed. The mean

lesion intensity (MLI) in the region of interest can therefore directly measure the fractionation progression in that region, and can serve as a reference metric of fractionation progression. This metric was computed for the three treatments and correlated to the fractionation metric extracted from the color Doppler velocity feedback (t_{PRV}) to determine its sensitivity in detecting histotripsy fractionation damage in the RBC tissue phantom.

5.2.4 Experiment 3 – Validate Bubble-induced Color Doppler in Ex Vivo Porcine Liver

A final experiment was conducted in ex vivo porcine liver to validate the bubble-induced color Doppler feedback in real tissue. Doppler data were collected throughout the histotripsy treatment. Ex vivo porcine liver samples were treated at different therapy doses (i.e., number of therapy pulses), with 3 samples per dose. The treated tissue was processed for histological analysis, and the degree of tissue fractionation corresponding to a therapy dose was assessed by counting the percentage of intact cell nuclei within the treatment region as described below. The t_{PRV} metric was computed for these datasets as described earlier. An alternative metric, the fixed delay focal mean velocity (FD-FMV), was also computed from synchronized, delayed color Doppler acquisitions at high frame rates. The FD-FMV would therefore be useful for applications requiring faster treatment pulsing rates. Both t_{PRV} and FD-FMV were correlated with the level of tissue fractionation evaluated histologically.

1. Tissue Preparation

Freshly excised porcine liver tissue was acquired from a local supplier, preserved in normal saline at 4° C, and used within 24 hours of harvest. Prior to treatment, the liver was sectioned into approximately 5 cm cube sections. The sections were placed in degassed saline (less than 20% of normal saturation determined by pO_2) at room temperature for at least 1 hour

to allow for equilibration of the temperature and gas concentration. The liver sections were then embedded in 1% agarose in the same ABS framed, polycarbonate walled housing.

2. Ex Vivo Tissue Treatment

Lesions were created in the liver samples with 50, 200, 500, 1000, or 2000 pulses per treatment location using the previously described histotripsy setup and therapy parameters. A total of 15 samples were treated, resulting in a sample size of 3 for each number of therapy pulses. The ultrasound imaging setup was identical to the previous experiments, with color Doppler interrogations performed following the therapy pulse delivered to center focal location after each full treatment of the therapy volume. This process was repeated every 1.5 seconds until all focal locations had been treated with up to 2000 pulses each. The Doppler acquisitions were processed identically to the previous experiments to produce a velocity progression over the course of histotripsy therapy.

3. Assessment of Degree of Tissue Fractionation

The degree of tissue fractionation was assessed for the lesions produced in the liver samples via histology. The liver sections were fixed in 10% neutral buffered formalin and processed for hematoxylin and eosin (H&E) staining. Histological sections 5 μm thick were made at 500 μm intervals through the lesion with slices oriented in parallel with the ultrasound imaging plane. The degree of tissue fractionation was evaluated with the percentage of structurally intact cell nuclei remaining in the lesions. This percentage was calculated using the method described in [2], and summarized here. The number of structurally intact cell nuclei was counted in five 320 μm × 240 μm regions near the center of the lesion, or in an untreated control region. An average count was obtained from the five counts. The average count for the lesion was then divided by that for the control, producing the percentage of nuclei remaining metric

(PNR). This metric was then compared to the fractionation metric extracted from the color Doppler velocity feedback (t_{PRV}) to determine its sensitivity in detecting histotripsy fractionation damage in tissue.

5.3 Results

5.3.1 Experiment 1 – Bubble-induced Motion estimation using PIV and Color Doppler

Following each histotripsy pulse, a cavitation bubble cloud was generated immediately and collapsed within 300 μs. Residual bubble nuclei persisted for over 100 ms after the cavitation collapse and were clearly visible in high-speed optical images of the focal region after a histotripsy therapy pulse. These residual nuclei acted as the contrast particles for PIV analysis of the bubble-induced motion. PIV velocity maps showed 2 phases of motion during the 20 ms after a histotripsy therapy pulse. For up to the first 2 ms, chaotic motion was present, where the motion was pointed in all directions in a random manner through this period and was inconsistent from pulse to pulse. This chaotic motion phase likely resulted from the violent activity of the histotripsy bubble cloud. After this chaotic motion subsides, a coherent motion along the direction of the therapy ultrasound beam was visible. The coherent motion was first moving away from the therapy transducer, and then rebounding back towards the therapy transducer and oscillating Figure 5-4 shows images of an example progression of the focal region PIV velocity map after the tissue had been treated with 50 histotripsy pulses. The therapy pulse was propagated from right to left.

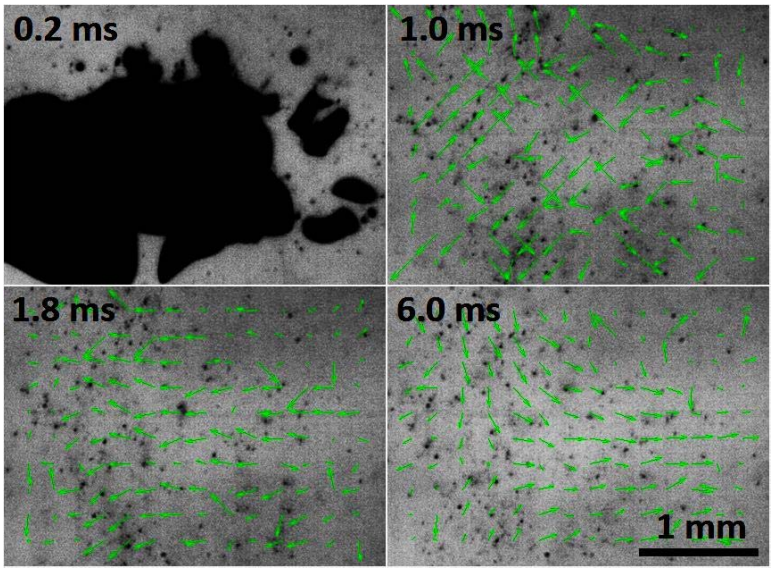

Figure 5-4: High speed images of the focal region 50 pulses into treatment (therapy applied from the right) with PIV velocity map overlays showing the histotripsy bubble cloud (top left), chaotic motion immediately after the collapse of the bubble cloud (top right), and finally coherent motion, including a push away from the transducer (bottom left) and subsequent rebound (bottom right).

Three treatments of 941 pulses were performed in the agarose tissue phantom, with the bubble-induced motion following the histotripsy pulses monitored using the PIV and color Doppler methods described. Velocity maps collected using both methods show a similar trend, with brief chaotic motion followed by push and rebound motion. This trend remained the same as the treatment progresses. The duration of these push and rebound motions were observed to increase over the course of histotripsy therapy as the tissue phantom was increasingly fractionated. The average velocity progression is shown in Figure 5-5 for both PIV and Doppler estimation methods. The estimated velocity is shown in color (red is away from therapy transducer and blue is towards the therapy transducer) versus the time delay from the onset of the therapy pulse (y axis) and the number of therapy pulses (x axis). Both profiles are shown over the same limited velocity range (-1 cm/sec to 1 cm/sec) to allow more easy comparison of the changes over the course of treatment.

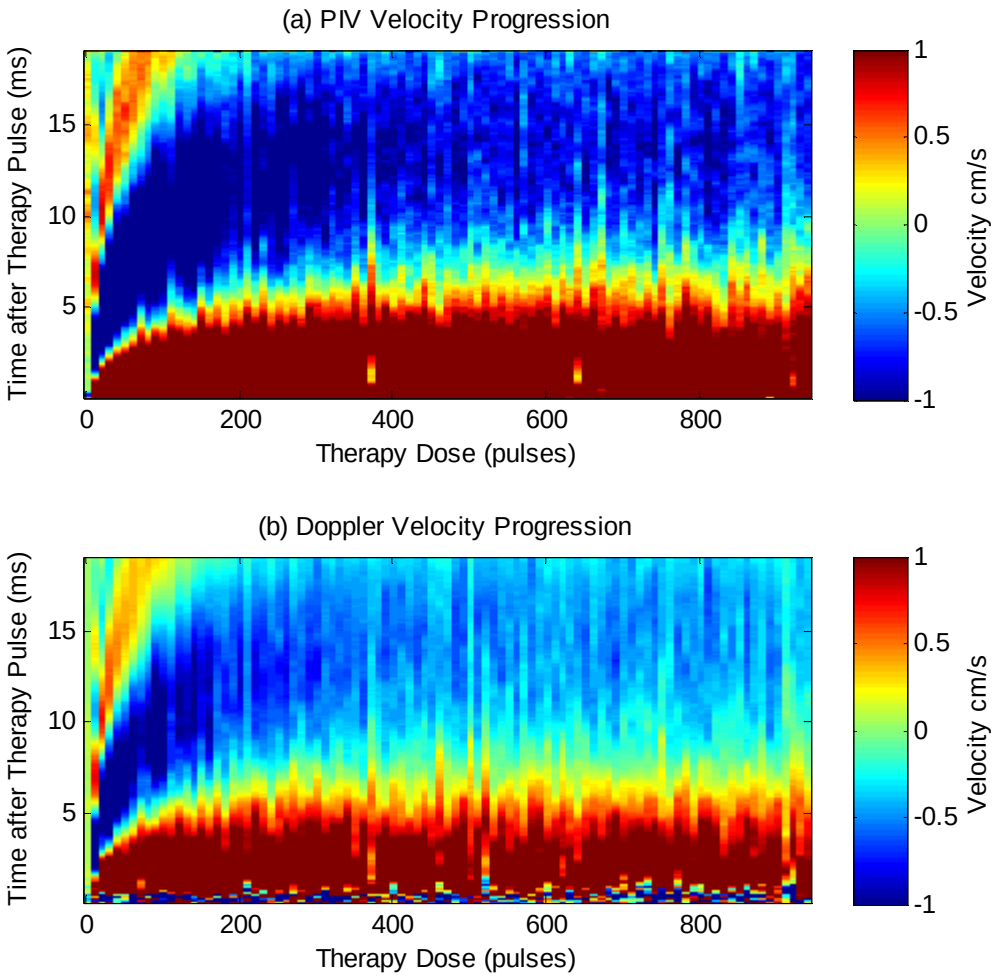

Figure 5-5: Comparison plots showing the average velocity estimates from PIV (a) and Doppler (b) after every 10 therapy pulses. The plots show velocity (color map) versus time after the therapy pulse (y-axis) over the course of therapy (x-axis).

For further comparison of the bubble-induced velocity estimated using PIV versus color Doppler for a specific number of therapy pulse applied, Figure 5-6 shows 3 individual velocity traces after 10, 30, and 290 therapy pulses. These traces correspond to vertical lines in the full velocity progressions at the specified dose points. After the 2 ms chaotic motion phase, PIV and Doppler estimates of the average velocity agree with each other well over the course of treatment with a root mean squared (RMS) error of 0.48 ± 0.1 cm/s. These plots show a temporal expansion of the velocity profile with increased therapy dose, likely resulting from reduced

elasticity as the phantom was increasingly fractionated by histotripsy pulses. For example, t_{PRV} was 2.6, 5.4, and 10.8 ms after 10, 30, and 290 pulses, respectively. The increase in the duration of the coherent push and rebound motion reached a plateau after roughly 250 pulses, likely because the phantom was completely liquefied.

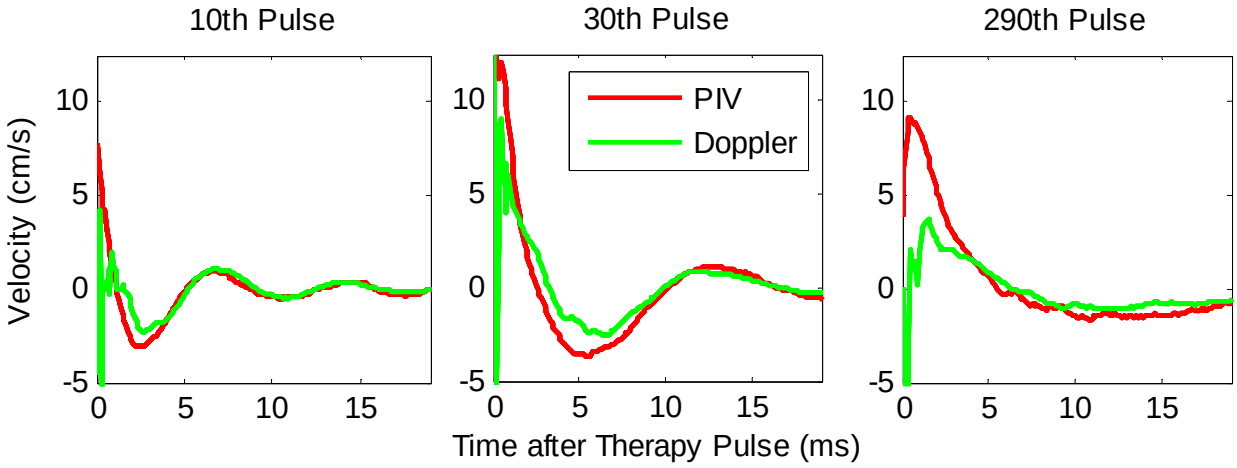

Figure 5-6: Individual velocity plots for the 19 ms after the therapy pulse after 10 therapy pulses (left), 30 therapy pulses (center), and 290 therapy pulses (right) showing good agreement between PIV and Doppler in measured velocity after the initial chaotic motion.

The t_{PRV} metric was computed for the velocity profiles obtained from the 3 treatments using PIV and Doppler data to further validate the Doppler velocity measurements. Analysis was performed on both the raw metric, along with a 5 point (50 pulse) moving average filtered version to compare the underlying trend in the progression of the t_{PRV} metric. Figure 5-7 shows the mean and standard deviation of the raw t_{PRV} metric from the PIV and Doppler analysis, along with the filtered version of each for comparison. t_{PRV} extracted from PIV and Doppler both increase with increasing therapy dose. Pulse to pulse variation between the two measurements was observed to increase for higher therapy dose (> 250 pulses). Figure 5-8 shows the correlation of the raw t_{PRV} metric from both sources, along with the correlation of filtered metric. The pulse

to pulse variation clearly reduced the correlation ($R^2 = 0.74$) for the raw metric, however the underlying trend is clearly the same from the high correlation of the filtered metric ($R^2 = 0.95$).

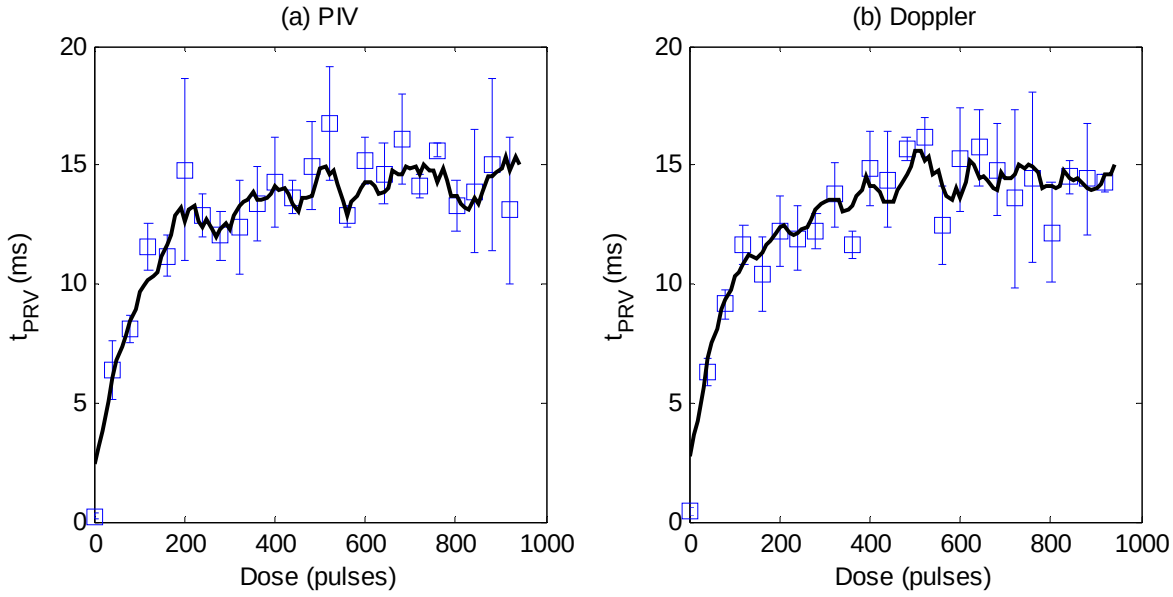

Figure 5-7: Plots of the t_{PRV} metric from the PIV analysis (a) and the Doppler analysis (b) with mean and standard deviation of the raw metric for every 40th pulse, along with a solid line representing the 5 point (50 pulse) moving average (N = 3).

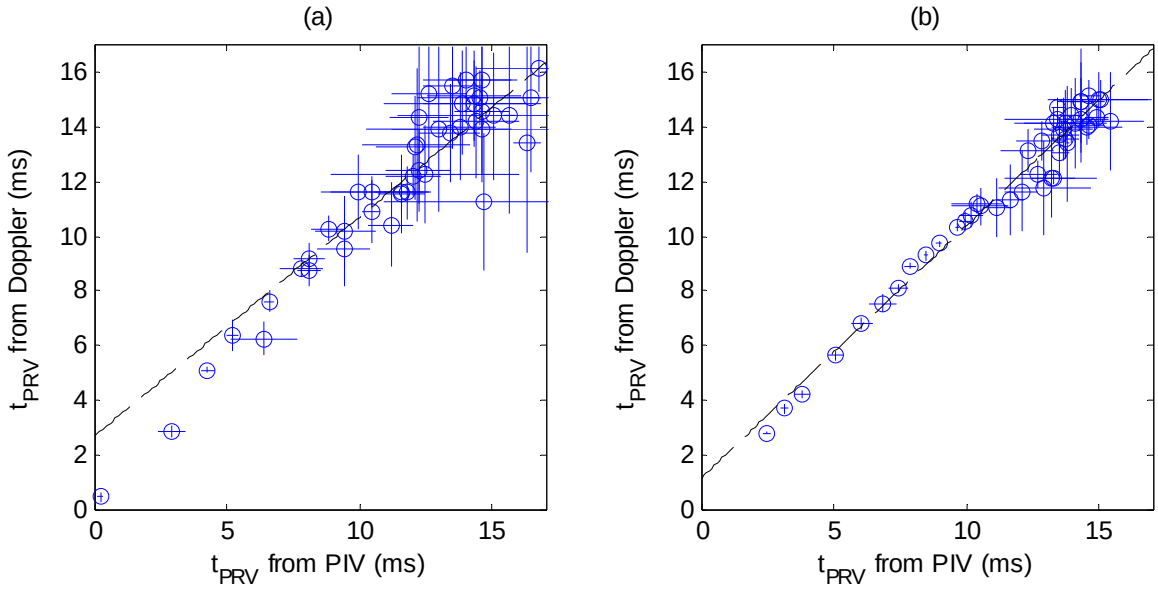

Figure 5-8: (a) Correlation of the t_{PRV} metric from the PIV and the Doppler analysis. Dashed line: $y = 0.8059 \cdot x + 2.673$ ($R^2 = 0.74$) (N = 3). (b) Correlation of the filtered t_{PRV} metric from the PIV and the Doppler analysis. Dashed line: $y = 0.9261 \cdot x + 1.14$ ($R^2 = 0.95$) (N = 3).

5.3.2 Experiment 2 – Correlate Bubble-induced Color Doppler with Histotripsy Tissue Fractionation in Agarose Phantom

In the agarose tissue phantom, optical images of the RBC layer and Doppler velocity profiles were collected after each of the 941 therapy pulses at the center of the treated volume. The RBC phantoms showed rapid fractionation for the first 50 pulses, with slower fractionation up to 120 pulses, when the lesion became completely transparent. Example images of the RBC layer fractionation progression are shown in Figure 5-9 after 10, 25, 100, and 250 pulses have been applied to all points in the treatment pattern.

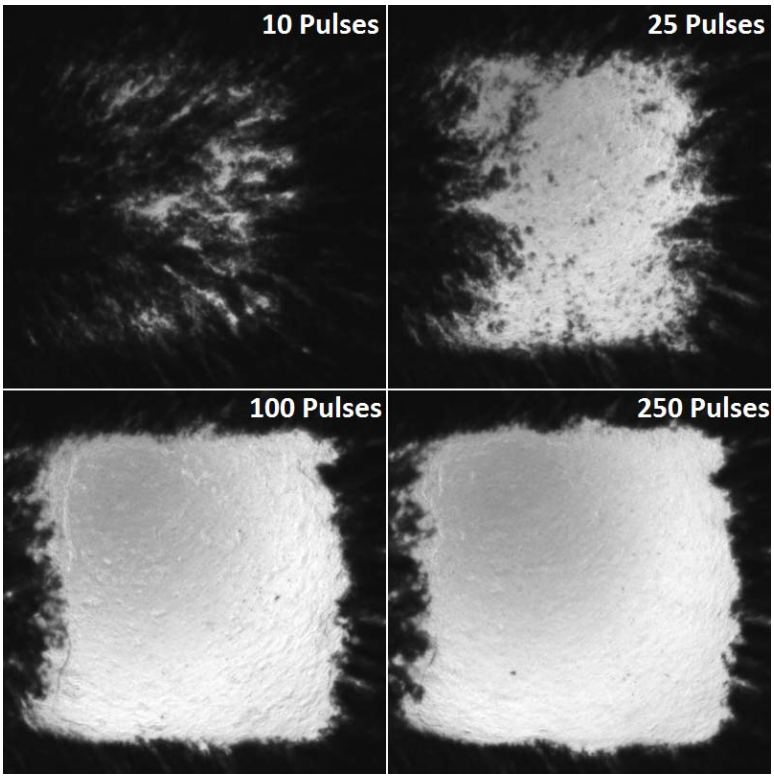

Figure 5-9: Images of the fractionated red blood cell (RBC) layer after 10 (top left), 25 (top right), 100 (bottom left), and 250 (bottom right) therapy pulses have been applied to each focal point in the 219 point focal pattern.

The color Doppler velocity progression is shown in Figure 5-10 over the first 500 pulses of the treatment. The estimated velocity is shown in color (red is away from the therapy

transducer and blue is towards the therapy transducer) versus the delay from the therapy pulse (y axis) and therapy dose (x axis). This velocity profile shows the velocity response expand in time for increased therapy dose, reaching a plateau after roughly 150 pulses. Additional therapy beyond this point generates no further change in the dynamics of the bubble induced motion that can be detected by color Doppler acquisitions.

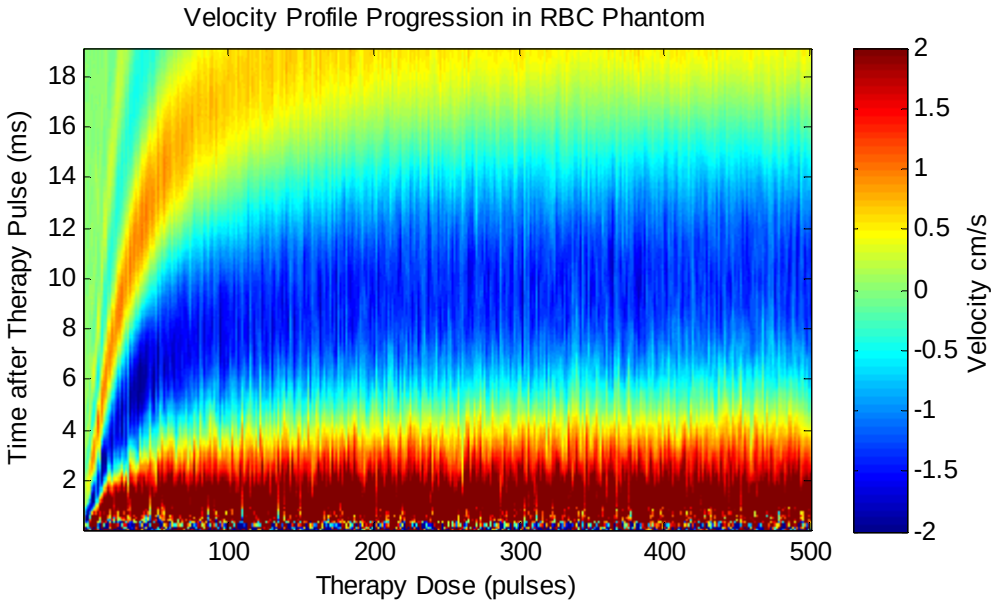

Figure 5-10: Average Doppler velocity profile for the first 500 pulses during the 6 RBC phantom ablations. The plot shows velocity (color map) versus time after the therapy pulse (y-axis) over the course of therapy (x-axis) (N=6).

Fractionation metrics were computed from the data for each of the 6 individual RBC layer treatments. From the optical images of the RBC layer, the fractionation metric of mean lesion intensity (MLI) was computed and is plotted over the course of therapy in Figure 5-11. This plot shows saturation of the MLI metric after approximately 120 pulses. At this point, images of the lesion show that all the RBC's in the layer had been destroyed and no further information could be obtained with this metric. From the Doppler velocity data, the time to peak rebound velocity (t_{PRV}) metric was computed for the motion following each therapy pulse. The

t_{PRV} metric can be visualized in the full velocity progression (Figure 5-10) as the time value (y-axis value) at which the highest negative velocity (darkest blue color) occurs for each value of therapy dose (x-axis value). This metric is plotted in Figure 5-11, showing saturation of the t_{PRV} metric after approximately 250 pulses, indicating no further change in the bubble induced motion following additional histotripsy therapy pulses. Both metrics were computed for all 1000 therapy pulses, but are displayed with mean and standard deviation for only every 10th pulse for the first 250 pulses for clarity.

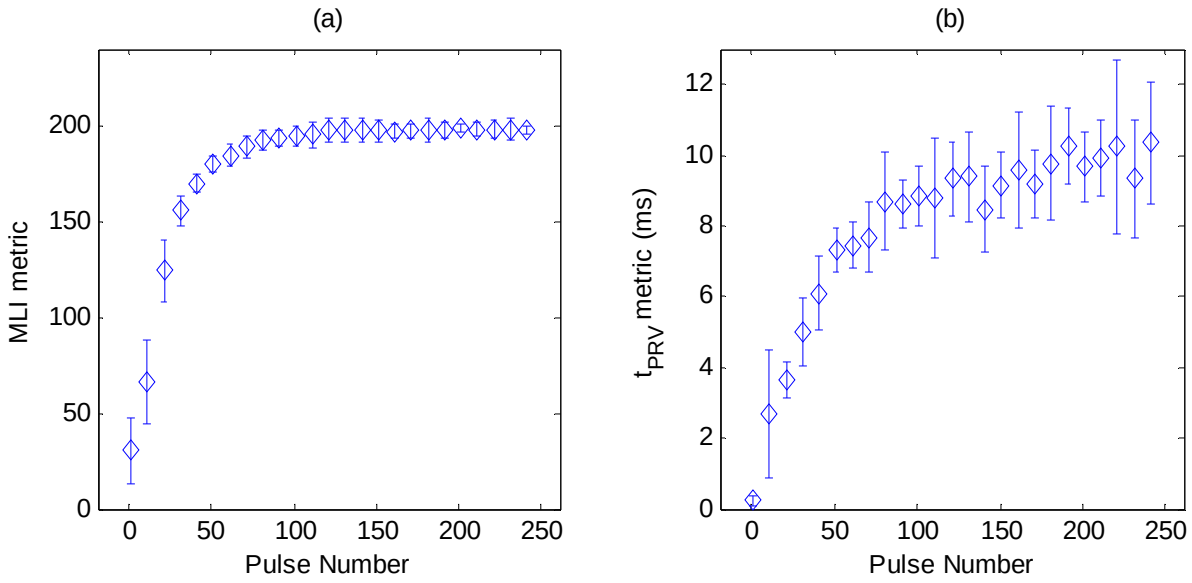

Figure 5-11: Progression of the MLI reference metric (a) and t_{PRV} metric (b) over the first 250 pulses of histotripsy therapy in the RBC layer Agarose phantom. Both metrics are plotted with mean and standard deviation (N = 6) for every 10th pulse for pulses 1 to 241 for clarity.

The correlation between these metrics was then computed to determine the validity of the t_{PRV} metric to measure the degree of fractionation of the target tissue and is shown in Figure 5-12. This analysis was confined to the first 120 pulses, since the reference metric of fractionation progress (MLI) saturated at this point, providing no additional information about the

fractionation progression for additional therapy. A linear correlation was observed between the t_{PRV} metric and the reference MLI metric ($R^2 = 0.95$).

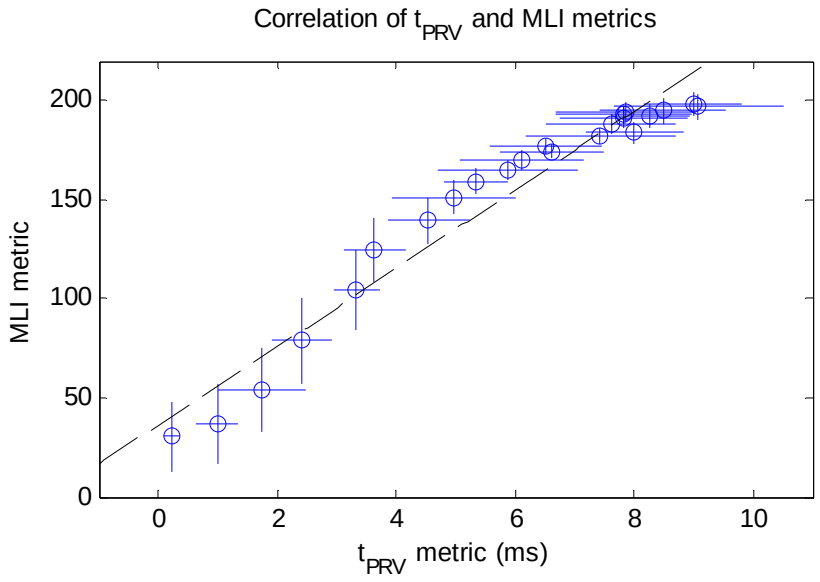

Figure 5-12: MLI metric vs. t_{PRV} metric for the first 120 pulses of therapy in the RBC phantom. Dashed line: $y = 19.81 \cdot x + 36.22$ ($R^2 = 0.95$) (N=6).

5.3.3 Experiment 3 – Validate Bubble-induced Color Doppler in Ex Vivo Porcine Liver

Representative histology of the lesions produced in the ex vivo liver sections are shown in Figure 5-13. In the control regions, all tissue and cellular structures appeared normal and structurally intact. Even with only a small number of pulses (50 pulses/treatment location) applied, large scale fractionation was apparent in the tissue. While some pockets of cells appeared structurally intact with normal appearing cell nuclei, much of the tissue appeared damaged with large regions of mostly homogenized tissue visible. At the next measured therapy dose (200 pulses/treatment location), nearly all tissue structures and cells were destroyed. Only a few scattered nuclei and tissue fragments remained intact. At a large number of pulses (>500 pulses/treatment location), the treated volume appeared completely homogenized with no recognizable tissue structures or cellular components. The tissues outside the lesion volume

appeared structurally intact, with only minor damage pockets scattered around the area very near the edges of the treated region (< 100 micron).

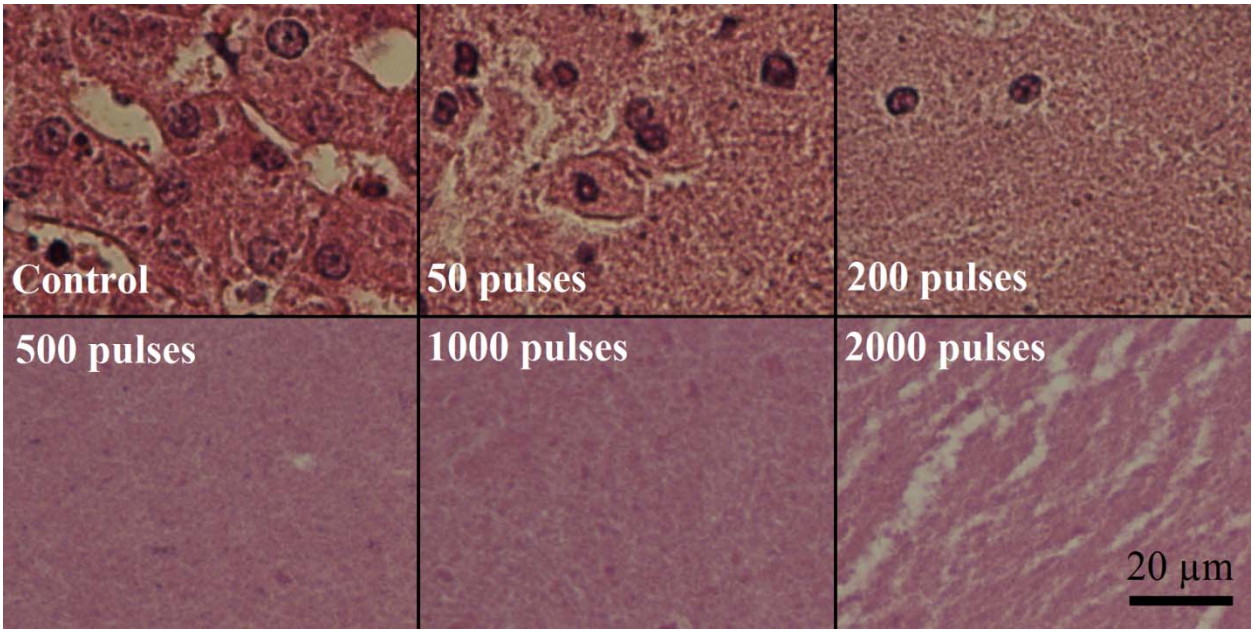

Figure 5-13: Histological sections of the lesions produced with increasing numbers of therapy pulses per treatment location. In the control, all tissue structures and cells appeared structurally intact. After 50 pulses, large volumes of acellular debris were observed, with some pockets of structurally intact cells and nuclei remaining. After 200 pulses, the entire lesion appeared fractionated with few remaining intact nuclei. Beyond this (>500 pulses/treatment location), the treated volume appeared completely homogenized with no recognizable tissue structures and very few fragments of nuclear material.

The percentage of nuclei remaining (PNR) metric in the treated volume was plotted against the number of therapy pulses in Figure 5-14. This percentage decreased exponentially with increasing numbers of therapy pulses ($R^2 = 0.97$), and reached nearly zero shortly after 200 pulses per treatment location.

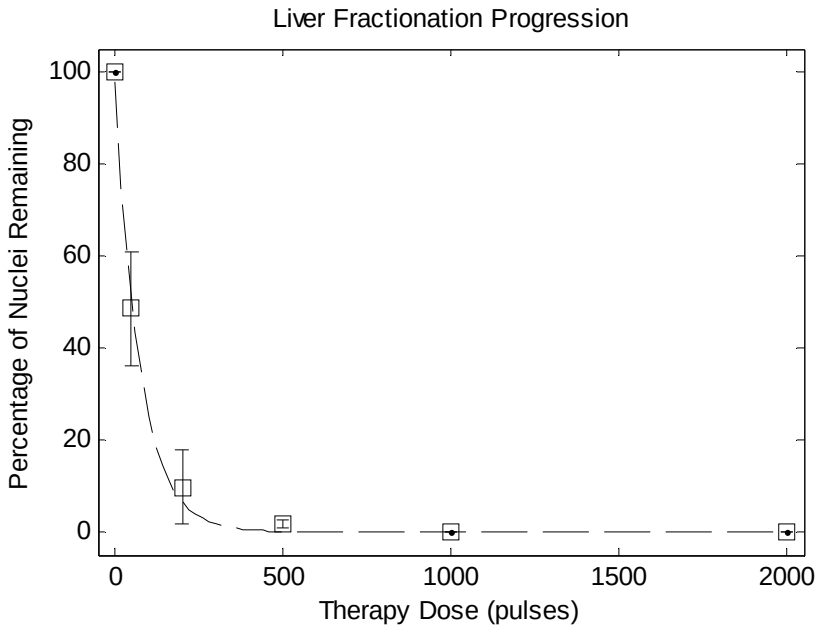

Figure 5-14: Percentage of structurally intact cell nuclei decreased exponentially with increasing numbers of therapy pulses per treatment location. Dashed line: $y = 99.37 \cdot e^{-0.01362 \cdot x}$ ($R^2 = 0.97$).

Color Doppler velocity profiles were collected after each of up to 2000 therapy pulses at the center of the treated volume for the 15 *ex vivo* liver treatments. Figure 5-15 shows the average velocity profile over the three 2000 pulse treatment. The estimated velocity is shown in color (red is away from the therapy transducer and blue is towards the therapy transducer) versus the delay from the therapy pulse (y axis) and therapy dose (x axis). The Doppler velocity profiles in the *ex vivo* porcine liver were similar to the agarose phantom, with a brief period of chaotic motion followed by coherent push and rebound motions. These coherent motions also expanded in time with increased therapy dose up to 800 pulses, likely due to increasing fractionation leading to complete tissue liquefaction at 800 pulses. After that point, the push duration stayed roughly constant or decreased slightly with increasing number of therapy pulses.

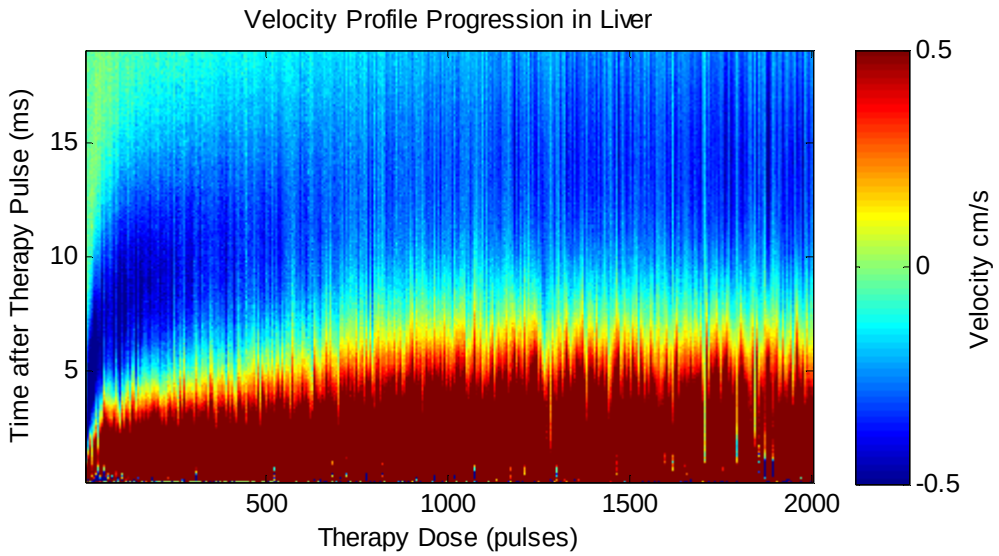

Figure 5-15: Plot showing the average velocity estimates from Doppler after every therapy pulse in ex vivo porcine liver. The plot shows velocity (color map) versus time after the therapy pulse (y-axis) over the course of therapy (x-axis) (N=3).

The t_{PRV} metric was computed from the color Doppler data collected during the 2000 pulse *ex vivo* liver treatments. This metric is plotted in Figure 5-16, showing a rapid increase in the t_{PRV} metric for the first 200 pulses, corresponding to the rapid fractionation necessary to cause the extent of the damage observed histologically at this time point. The t_{PRV} metric continued to slowly increase from 200 to 800 pulses, indicating continued fractionation of the tissue fragments. After approximately 800 pulses, no consistent change in the bubble induced motion following additional histotripsy therapy pulses was observed. The metric was computed for all 2000 therapy pulse, but is displayed with mean and standard deviation for only every 10^{th} pulse for the first 200 pulses (Figure 5-16b), and every 40^{th} pulse for the first 1200 pulses (Figure 5-16b) for easy of visualization. From 1200 to 2000 pulses, t_{PRV} has a flat trend, similar to that from 800-1200 pulses.

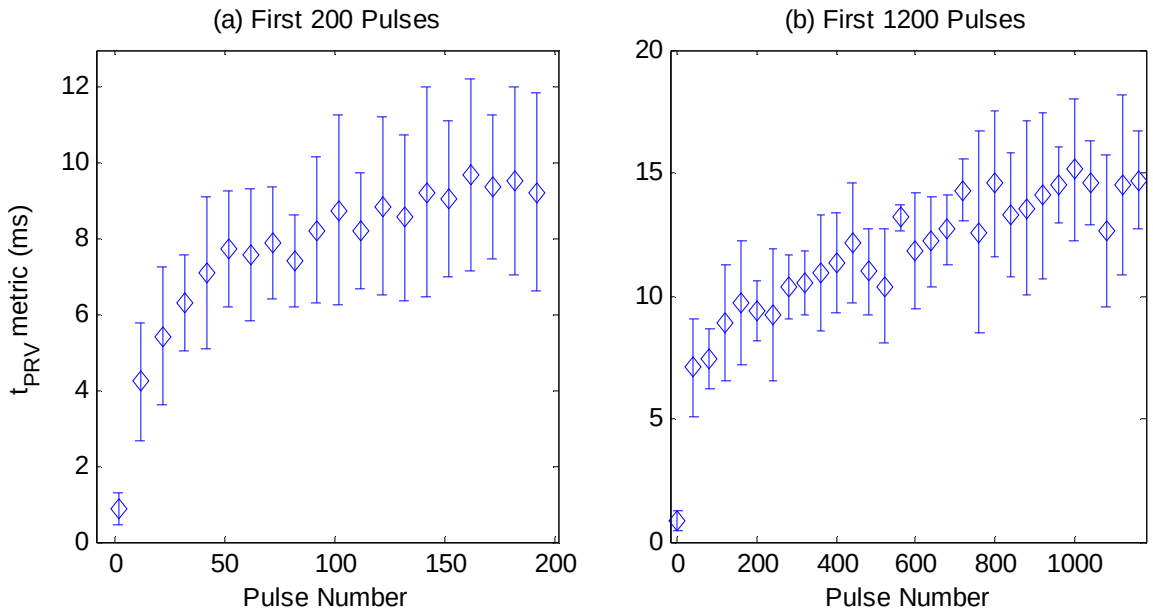

Figure 5-16: Plots of t_{PRV} metric over the course of therapy in the *ex vivo* porcine liver tissue. Panel (a) shows the rapid increase in the t_{PRV} metric during the first 200 pulses and panel (b) shows the slower increase from 200 to 800 pulses. Pulses beyond this point generated no significant change in the t_{PRV} metric (N = 3).

The correlation between the t_{PRV} metric and the PNR metric was then computed to determine the validity of the t_{PRV} metric to measure the degree of fractionation in tissue and is shown in Figure 5-17. This analysis was confined to the first 500 pulses, since the reference metric of fractionation progress (PNR) saturated at this point, providing no additional information about the fractionation progression for additional therapy.

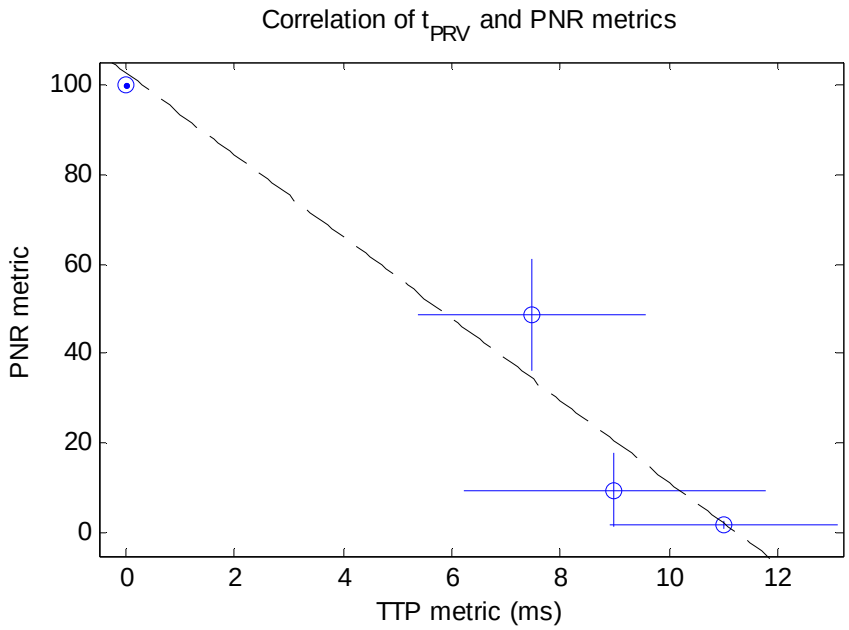

Figure 5-17: PNR metric vs. t_{PRV} metric for the first 500 pulses of therapy in the *ex vivo* liver samples. Dashed line: $y = -9.107 \cdot x + 102.5$ ($R^2 = 0.95$) (N = 3).

The FD-FMV metric was computed from the color Doppler data collected during the 2000 pulse *ex vivo* liver treatments using at a delay of 14.3 ms. This metric can be visualized in the full velocity progression (Figure 5-10) as the velocity value (color axis) for each value of therapy dose (x-axis) at a fixed delay of 14.3 ms (y-axis). The pulse to pulse variation in the Doppler velocity measurement leads to increased noise in this measurement, for this reason, a 10 point rolling average filter was applied to each individual FD-FMV vs dose trace before comparison. This metric is plotted in Figure 5-18a for the first 500 pulses with mean and standard deviation for every 25th pulse for clarity. This delay was chosen since it behaved similarly to the t_{PRV} metric, capturing the rapid increase in the observed velocity for the first 200 pulses, with a slower increase beyond 200 pulses. The correlation between the FD-FMV metric and the PNR metric was then computed to determine the validity of the metric to measure the degree of fractionation in tissue and is shown in Figure 5-18b. This analysis was also confined to

the first 500 pulses, due to the saturation of the reference metric of fractionation progress (PNR) at this point. A linear correlation was observed between the t_{PRV} metric and the reference PNR metric ($R^2 = 0.95$).

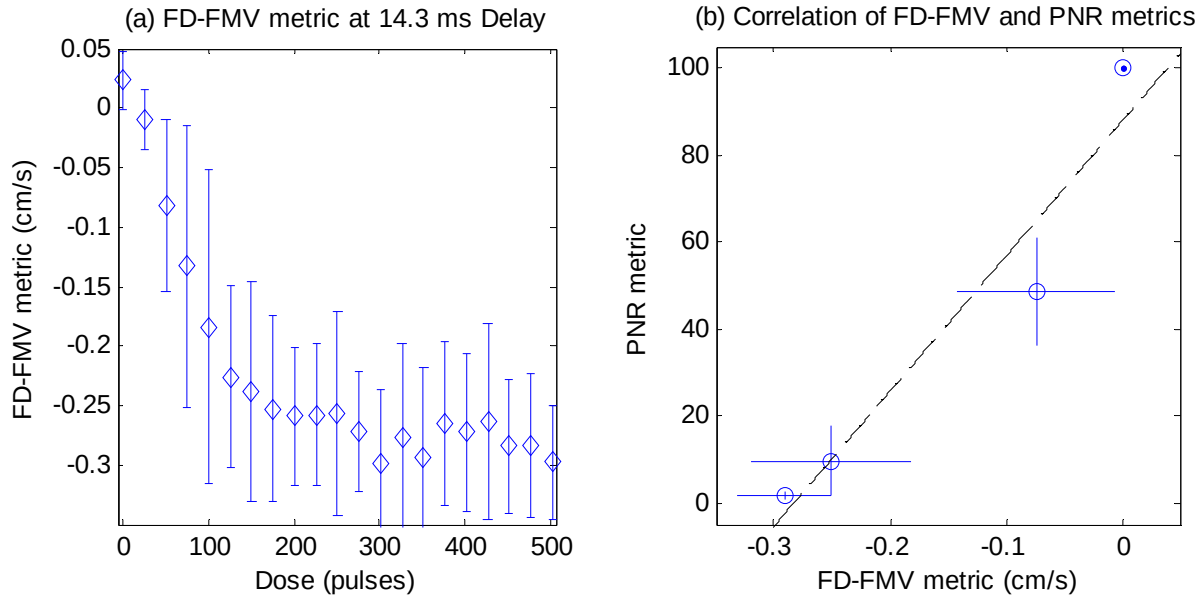

Figure 5-18: Panel (a) shows the FD-FMV metric at 14.3 ms delay for the first 500 pulses of therapy in the ex vivo liver samples. Panel (b) shows the PNR metric vs. the FD-FMV metric for the first 500 pulses in the *ex vivo* liver samples. Dashed line: $y = 310.7 \bullet x + 87.85$ ($R^2 = 0.93$) (N = 3).

5.4 Discussion

The imaging feedback method proposed in this paper relies on bubble-induced motion after each histotripsy pulse at the therapy focus along the axis of propagation. The source of this motion is not fully understood at this time, but the experiments presented here demonstrate that the phenomenon is consistent and reproducible. Several potential mechanisms have been identified, and are currently being investigated. Acoustic radiation force is a tempting choice for the mechanism behind the type of push-rebound motions observed in this study, however the extremely short pulses (< 2 cycles) are not sufficient to generate the observed motion simply

through absorption alone. Moreover, preliminary experiments show no measurable focal velocity at slightly sub-cavitation threshold pulses (~28.7 MPa peak negative pressure) with large velocities comparable to those observed in this study for supra-threshold pulses (~38.6 MPa peak negative pressure). This does not completely eliminate acoustic radiation force however, as the presence of forming cavitation bubbles could greatly enhance the radiation force via reflection of subsequent acoustic energy. The violent collapse of the histotripsy bubble cloud is another potential mechanism that could generate the observed motion. Certainly the cloud collapse generates much of the chaotic motion in the focal region observed in this study, but it could also generate consistent pushes of the focal region should the transducer geometry produce bubble clouds that consistently collapse asymmetrically. Another potential mechanism is asymmetric expansion of the bubbles during the formation of the bubble cloud. High speed imaging has shown that as the individual bubbles form, they grow more along the direction of propagation than back toward the therapy transducer, generating a net force on the medium. The cumulative effect of all the bubbles could generate the motion observed in this study. Some combination of these mechanisms is also possible, and a comprehensive study is in progress based on these preliminary results to fully elucidate the mechanism behind this observed motion.

One advantage of the methods presented in this work is the ability to acquire these metrics during therapy, for real-time feedback on histotripsy fractionation progression. An important consideration is therefore how rapidly these metrics can be computed. The primary metric presented in this work, t_{PRV}, has significant acquisition and computational requirements. The major computational element is the processing of the 190 color Doppler acquisition sets to form the full 20 ms velocity profile at the 0.1 ms time resolution used in this work. A real-time method using these exact techniques would likely achieve frame rates around 0.25 Hz, though

optimization and parallelization would likely improve this by a factor of 10. Therapy monitoring at this rate would be most useful for volume ablations similar to the 6 mm cube treatment presented in this work, where the treatment progression is monitored for a single location with the remainder of the lesion treated during processing. Once the monitored location has been sufficiently fractionated, additional probing pulses with color Doppler fractionation feedback could be directed to other points in the treated volume to verify complete treatment over the full lesion. If focal steering is not possible, or serial lesion creation is required, this feedback can still be acquired for some subset of the therapy pulses applied. For example, if therapy is applied at 100 Hz PRF, and color Doppler feedback rate is possible at 1 Hz, you would pause therapy for the 20 ms Doppler acquisitions every 100^{th} pulse, and process the data while treating another 100 pulses at 100 Hz. However, it may be necessary in certain applications to gather feedback more rapidly, and for this reason the FD-FMV metric was developed. The FD-FMV metric is essentially a spatial velocity average taken from a standard color Doppler imaging sequence. This metric is currently achievable in real-time at an average rate of 30 Hz on the Verasonics imaging system used in this study. The only requirements are that the color Doppler acquisitions be synchronized and delayed from the therapy pulses by a predetermined amount, and that ultrasound imaging system provides access to the color Doppler data for spatial averaging. The required delay would be determined from preliminary tissue studies, similar to those presented here, in the target tissue to identify an appropriate delay that generates a metric sensitive to the desired therapeutic endpoint. Other metrics, extensions of these metrics, or detectors based on these metrics are also possible from bubble-induced color Doppler feedback including: push or rebound duration metrics, fixed delay peak velocity or zero-crossing detection, and focal mean velocity saturation detection.

Other methods for quantitative histotripsy therapy feedback have been developed previously, including ultrasound backscatter reduction [1, 2], ultrasound shear wave elastography [13], and peak-to-peak displacement of the shear displacement profile [REF]. Though the results cannot be directly compared due to the use of a different transducer and therapy pulsing parameters, we are encouraged by the sensitivity of the elasticity metric for detecting histotripsy therapy progress at low therapy doses presented in [13]. We believe that changes to the tissue mechanical properties, especially elasticity, at the focus in response to histotripsy fractionation are the primary cause of the changes to the bubble-induced velocity profile captured by the metrics presented in this work. No direct calculations of tissue mechanical properties are possible using these methods at this time, since the mechanism of the push is not fully understood; therefore additional work is necessary to determine what tissue properties are being measured using these techniques.

Although the methods presented here were only tested in liver tissue, the principle is likely applicable in other tissues that soften as they are increasingly fractionated by histotripsy pulses. Based on our experience, most soft tissues follow this trend, including liver [1], kidneys [15, 16], prostate [17-20], heart [21-23], and thrombus [24]. Although the different tissues begin therapy, and likely end therapy, with varying mechanical properties, it is expected that this softening will result in a temporally expanding velocity profile similar to that observed in liver in this work. Furthermore, we anticipate that metrics extracted from color Doppler measurements of the bubble-induced motion resulting from histotripsy therapy will change as the tissue is increasingly fractionated and eventually saturate when the tissue is completely homogenized. Therefore these metrics, or similar metrics from color Doppler acquisitions, are potentially useful for real-time feedback during any histotripsy therapy application.

5.5 Conclusion

This chapter shows that histotripsy pulses generate a consistent push at the therapy focus. Characteristics of this push and rebound motion can be accurately estimated using standard color Doppler acquisitions due to enhanced scattering from the residual cavitation nuclei persisting after histotripsy bubble cloud collapse. This was verified by direct comparison with simultaneous optical PIV measurements of the motion of these nuclei in an otherwise acoustically transparent agarose gel phantom. The tissue response to this push changes significantly as the tissue is fractionated by histotripsy. This change can be quantified by metrics extracted from color Doppler acquisitions acquired during continuous therapy. These metrics are closely related to the degree of tissue fractionation as indicated by reference metrics of tissue damage (e.g. RBC lysing and percentage of the structurally intact cell nuclei), thereby providing real-time quantitative feedback on the fractionation progression. Further analysis, targeting a specific tissue and therapeutic endpoint, could refine these methods into a valuable feedback metric for any tissue that can be fractionated using histotripsy.

5.6 References

[1] T. L. Hall, J. B. Fowlkes, and C. A. Cain, "A Real-Time Measure of Cavitation Induced Tissue Disruption by Ultrasound Imaging Backscatter Reduction," *IEEE Transactions on Ultrasonics, Ferroelectrics, and Frequency Control,* vol. 54, pp. 569-575, March 2007.

[2] T.-Y. Wang, Z. Xu, F. Winterroth, T. L. Hall, J. B. Fowlkes, E. D. Rothman, W. W. Roberts, and C. A. Cain, "Quantitative Ultrasound Backscatter for Pulsed Cavitational Ultrasound Therapy-Histotripsy," *IEEE Transactions on Ultrasonics, Ferroelectrics, and Frequency Control,* vol. 56, pp. 995-1005, May 2009.

[3] T. L. Hall, G. R. Lee, C. A. Cain, and L. Hernandez-Garcia, "Relaxation Properties of Cavitation Induced Tissue Lesions," presented at the Joint Annual Meeting ISMRM

(International Society for Magnetic Resonance in Medcine)-ESMRMB (European Society for Magnetic Resonance in Medicine and Biology), 2007.

[4] M. Fatemi and J. F. Greenleaf, "Probing the dynamics of tissue at low frequencies with the radiation force of ultrasound," *Physics in Medicine and Biology,* vol. 45, pp. 1449-1464, June 2000.

[5] K. Nightingale, M. S. Soo, R. Nightingale, and G. Trahey, "Acoustic radiation force impulse imaging: in vivo demonstration of clinical feasibility," *Ultrasound in Medicine & Biology,* vol. 28, pp. 227-235, February 2002.

[6] M. O'Donnell, A. R. Skovoroda, B. M. Shapo, and S. Y. Emelianov, "Internal Displacement and Strain Imaging Using Ultrasonic Speckle Tracking," *IEEE Transactions on Ultrasonics, Ferroelectrics and Frequency Control,* vol. 41, pp. 314-325, May 1994.

[7] J. Ophir, I. Céspedes, H. Ponnekanti, Y. Yazdi, and X. Li, "Elastography: A quantitative method for imaging the elasticity of biological tissues," *Ultrasonic Imaging,* vol. 13, pp. 111-134, April 1991.

[8] K. J. Parker, S. R. Huang, R. A. Musulin, and R. M. Lerner, "Tissue response to mechanical vibrations for “sonoelasticity imaging”," *Ultrasound in Medicine & Biology,* vol. 16, pp. 241-246, 1990.

[9] L. Sandrin, M. Tanter, S. Catheline, and M. Fink, "Shear Modulus Imaging with 2-D Transient Elastography," *IEEE Transactions on Ultrasonics, Ferroelectrics, and Frequency Control,* vol. 49, pp. 426-435, April 2002.

[10] S. Y. Emelianov, M. A. Lubinski, W. F. Weitzel, R. C. Wiggins, A. R. Skovoroda, and M. O'Donnell, "Elasticity imaging for early detection of renal pathology," *Ultrasound in Medicine & Biology,* vol. 21, pp. 871-883, 1995.

[11] T. A. Krouskop, T. M. Wheeler, F. Kallel, B. S. Garra, and T. Hall, "Elastic moduli of breast and prostate tissues under compression," *Ultrasonic Imaging,* vol. 20, pp. 260-274, October 1998.

[12] W.-C. Yeh, P.-C. Li, Y.-M. Jeng, H.-C. Hsu, P.-L. Kuo, M.-L. Li, P.-M. Yang, and P. H. Lee, "Elastic modulus measurements of human liver and correlation with pathology," *Ultrasound in Medicine & Biology,* vol. 28, pp. 467-474, April 2002.

[13] T.-Y. Wang, T. L. Hall, Z. Xu, J. B. Fowlkes, and C. A. Cain, "Imaging Feedback of Histotripsy Treatments Using Ultrasound Shear Wave Elastography," *IEEE Transactions on Ultrasonics, Ferroelectrics, and Frequency Control,* vol. 59, pp. 1167-1181, June 2012.

[14] A. D. Maxwell, T. Y. Wang, L. Yuan, A. P. Duryea, Z. Xu, and C. A. Cain, "A tissue phantom for visualization and measurement of ultrasound-induced cavitation damage," *Ultrasound Med Biol,* vol. 36, pp. 2132-43, Dec 2010.

[15] W. W. Roberts, T. L. Hall, K. Ives, J. S. Wolf, Jr, J. B. Fowlkes, and C. A. Cain, "Pulsed Cavitational Ultrasound: A Noninvasive Technology for Controlled Tissue Ablation (Histotripsy) in the Rabbit Kidney," *The Journal of Urology,* vol. 175, pp. 734-738, February 2006.

[16] N. R. Styn, T. L. Hall, J. B. Fowlkes, C. A. Cain, and W. W. Roberts, "Histotripsy of renal implanted VX-2 tumor in a rabbit model: investigation of metastases," *Urology,* vol. 80, pp. 724-729, Sep 2012.

[17] T. L. Hall, C. R. Hempel, K. Wojno, Z. Xu, C. A. Cain, and W. W. Roberts, "Histotripsy of the prostate: dose effects in a chronic canine model," *Urology,* vol. 74, pp. 932-937, October 2009.

[18] C. R. Hempel, T. L. Hall, C. A. Cain, J. B. Fowlkes, Z. Xu, and W. W. Roberts, "Histotripsy fractionation of prostate tissue: Local effects and systemic response in a canine model," *The Journal of Urology,* vol. 185, pp. 1484-1489, April 2011.

[19] A. M. Lake, T. L. Hall, K. Kieran, J. B. Fowlkes, C. A. Cain, and W. W. Roberts, "Histotripsy: minimally invasive technology for prostatic tissue ablation in an in vivo canine model," *Urology,* vol. 72, pp. 682-686, September 2008.

[20] J. C. Wheat, T. L. Hall, C. R. Hempel, C. A. Cain, Z. Xu, and W. W. Roberts, "Prostate histotripsy in an anticoagulated model," *Urology,* vol. 75, pp. 207-211, January 2010.

[21] G. Owens, R. Miller, S. Owens, S. Swanson, K. Ives, G. Ensing, D. Gordon, and Z. Xu, "Intermediate-Term Effects of Intracardiac Communications Created Noninvasively by Therapeutic Ultrasound (Histotripsy) in a Porcine Model," *Pediatric Cardiology,* vol. 33, pp. 83-89, 2012/01/01 2012.

[22] G. E. Owens, R. M. Miller, G. Ensing, K. Ives, D. Gordon, A. Ludomirsky, and Z. Xu, "Therapeutic ultrasound to noninvasively create intracardiac communications in an intact animal model," *Catheterization and Cardiovascular Interventions,* vol. 77, pp. 580-588, 2011.

[23] Z. Xu, G. Owens, D. Gordon, C. A. Cain, and A. Ludomirsky, "Noninvasive Creation of an Atrial Septal Defect by Histotripsy in a Canine Model," *Circulation,* vol. 121, pp. 742-749, February 2010.

[24] A. D. Maxwell, G. Owens, H. S. Gurum, K. Ives, D. D. Myers, and Z. Xu, "Noninvasive treatment of deep venous thrombosis using pulsed ultrasound cavitation therapy (histotripsy) in a porcine model," *Journal of Vascular and Inerventional Radiology,* vol. 22, pp. 369-377, March 2011.

Chapter 6
An Integrated Histotripsy Therapy System for Pediatric Cardiac Applications

6.1 Introduction

To transition histotripsy into a clinical tool for pediatric cardiac applications, an integrated, ultrasound image-guided, histotripsy therapy system should be designed and constructed specifically for the human neonate with congenital heart disease. This complete histotripsy therapy system includes an integrated probe; consisting of a compact therapy transducer, an acoustic coupling apparatus and an ultrasound imaging probe. The system also includes the control unit; consisting of the ultrasound imaging system, driving electronics for the therapy transducer, and a macro-positioning arm and motorized micro-positioner to connect and manipulate the integrated probe. The control unit should be a mobile cart and chassis, housing the ultrasound imaging system, the driving electronics and a host computer with software to control and integrate all the components (Figure 6-1).

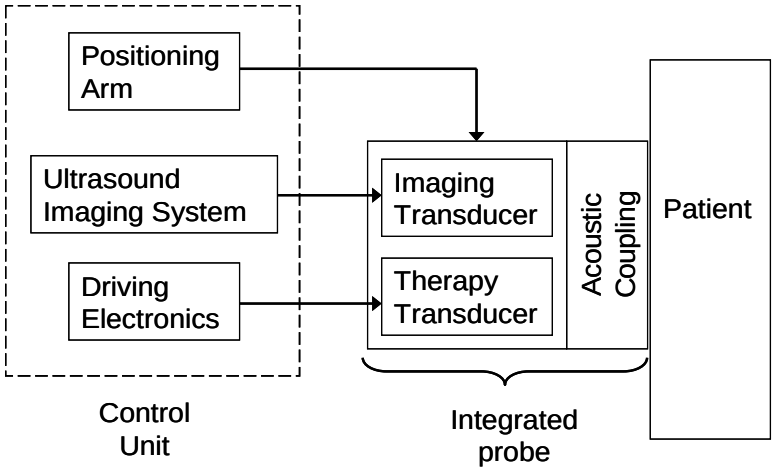

Figure 6-1: Block diagram of the complete, integrated pediatric cardiac histotripsy therapy system

This chapter will focus first on development of materials and methods for therapy transducers for the pediatric cardiac application specifically. This includes the analysis of several piezo-electric materials for use in custom transducers, as well as the testing of various array designs including several transducers built in-house and a custom manufactured commercial transducer. Second, a custom ultrasound imaging probe will be designed to integrate directly into these transducers and minimize loss of active area in the therapy transducer design. This probe will be built compatible with an ultrasound imaging system that allows flexible programing for the potential integration of custom guidance and therapy feedback techniques (e.g. color Doppler fractionation feedback, motion tracking, etc). Finally, a description of other required parts and integration of all components into a complete pediatric cardiac histotripsy system is detailed.

6.2 Histotripsy Therapy Transducer

The primary component of this integrated pediatric cardiac histotripsy therapy system is the histotripsy transducer. The main design consideration for this application is the acoustic

access to the heart in the human neonate. Echocardiography data collected from HLHS patients in previous work (Table 6-1) shows a subcostal acoustic window free of rib and lung obstruction with very little atrial septum motion [1].

Table 6-1: Measurements on Human HLHS Neonatal Patients using Echocardiography

Measurements	Coronal (mm)	Sagittal (mm)
Skin to RA wall distance	21.5 – 28.0	20.7-27.5
RA wall to Atrial Septum distance	11.2 – 18.5	11.4-17.5
Atrial Septal thickness	1.7 – 2.2	1.5-2.1
Atrial Septal Length	11.2-17.4	8.8-11.4
Septum to LA wall distance	7.7 – 10.4	8.8- 11.4
Septal motion	1 – 2	1-2
RA free wall motion	1 – 3	1-3
LA free wall motion	0 – 1	0-1

Based on this data, the transducer must be capable of generating a histotripsy bubble cloud on the atrial septum in the neonatal heart through the roughly 4 x 6 cm subcostal acoustic window through an estimated 3-4.5 cm of overlying tissue in the acoustic path. Transducers were designed with slightly larger active area than this to ensure full utilization of the acoustic window. To accommodate differences in anatomy, the transducer must have at least 4.5 cm of working distance (perpendicular distance from the front plane of the transducer to the focal position), or be steerable along the propagation axis to allow for working distances of 3 – 4.5 cm.

Methods have been developed within our research group to design and manufacture therapy transducers of any geometry at low cost. These transducers contain multiple flat piezoelectric elements acoustically matched to a focusing lens within a custom housing shell designed in 3D modeling software and manufactured using stereolithography (SLA) rapid prototyping. There are four main advantages of using this rapid prototyping method to build a high pressure, focused transducer in comparison to using a single segment of spherical

piezoelectric crystal: 1) the cost and time to develop and build a transducer is significantly reduced, as small flat piezoelectric elements are readily available, 2) transducers can be easily built for any complex geometry, 3) acoustic matching layer can be applied to increase the transducer bandwidth and surface pressure transmission to the media, and 4) the electric impedance of the smaller element allows (through our amplifier) very high voltage to be delivered and high pressure to be achieved. These methods are ideal for rapid iteration in early feasibility testing; however, a custom manufactured transducer has several main advantages that make it more suitable for a clinical prototype. The primary advantage is that the array elements can be arbitrarily shaped and sized, allowing for elements to be much more densely packed and even arranged to allow steering of the therapy focus. Secondarily, since the goal of this work is develop a tool to translate histotripsy into a clinical trial, a device manufactured within regulatory guidelines, using materials certified for bio-compatibility would expedite this process. Based on the strengths of these methods; initial prototype design, manufacture, and testing would be conducted in house to determine an optimal design for a final prototype to be manufactured by a third party with electrical and biocompatibility certification included.

6.2.1 PZT-4 and PMN-PT Single Crystal Element Testing

Previous transducers built within our group have primarily used lead zirconium titanate (PZT), or more specifically the PZT-4 composition. A single crystal PMN-PT material (JFE Mineral Company LTD., Tokyo, Japan) is assessed here for potential use in the pediatric cardiac transducer to increase the pressure output versus this standard. The PZT-4 elements used were diced from 45mm plates of SM111, a modified formulation of PZT-4 (SMPL45W45T14111, Steiner and Martin Inc., Miami, USA). To directly compare the PMN-PT single crystal with a

standard PZT-4 transducer, single element housings with acoustic focusing lens and ¼ wavelength tungsten epoxy matching layer were designed and constructed. Identical housings were manufactured using SLA rapid prototyping and assembled with a single crystal PMN-PT element (20 x 20 x 1.5 mm) and a PZT-4 element cut to the same size. Though these elements are manufactured for use at 1.5 MHz, they were electrically matched and driven at 1.25 MHz. This is possible due to the increased bandwidth that results from acoustically matching the element to the lens with a tungsten epoxy layer. To facilitate maximum electrical driving efficiency, the elements were electrically matched using an "L-C" type matching network. The PMN-PT element started with an electrical impedance of 40.7 – j12.6 ohms, and was electrically matched to 5.4 ohms. The PZT-4 element started with an electrical impedance of 12.4 – j44.2 ohms, and was matched to 7 ohms. This resulted in voltage gains of about 4 for the PMN-PT element and 5.4 for the PZT-4 element.

The transducers were driven with high-voltage square waves at 1.266 MHz, and the pressure output was measured using a 200 μm piezoelectric "bullet" hydrophone (HGL-0200; Onda Corp., Sunnyvale, CA) for 2D planes perpendicular to the propagation direction 6 mm from the element surface and at the geometric focus. The driving voltage used in each case resulted in 150 V peak to peak (Vpp) applied to the element in all tests. The 2D surface pressure profiles for the PZT-4 and PMN-PT transducers are shown in Figure 6-2. The PZT-4 produced a mean peak negative pressure of about 120 kPa over the 20 x 20 mm scan, while the PMN-PT produced a mean peak negative pressure of 275 kPa. The notch of reduced pressure on the right side of both profiles corresponds to the hollow well in the lens where the front electrode attaches to the element.

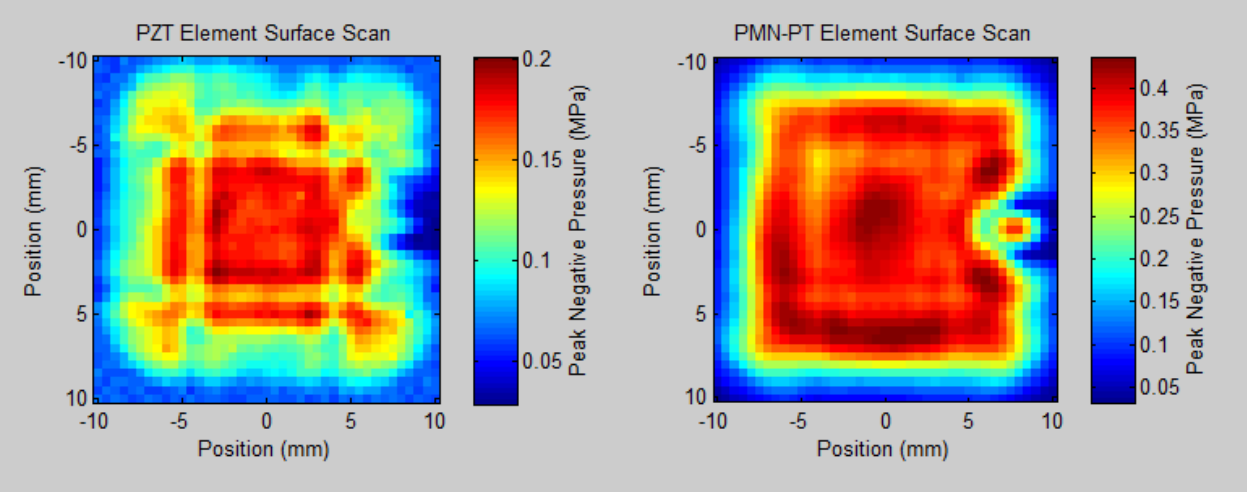

Figure 6-2: Surface pressure measurements taken ~6 mm from the transducer elements for the PZT-4 transducer (left) and the PMN-PT transducer (right).

2D focal pressure profile for the PZT-4 and PMN-PT transducers are shown in Figure 6-3. The PZT-4 produced a peak negative pressure of 0.69 MPa, while the PMN-PT produced a peak negative pressure of 1.9 MPa. The PMN-PT element focused more sharply, despite the identical element size, housing and lens (-6 dB beam width of 2.72 mm for the PMN-PT versus 3.18 mm for the PZT-4).

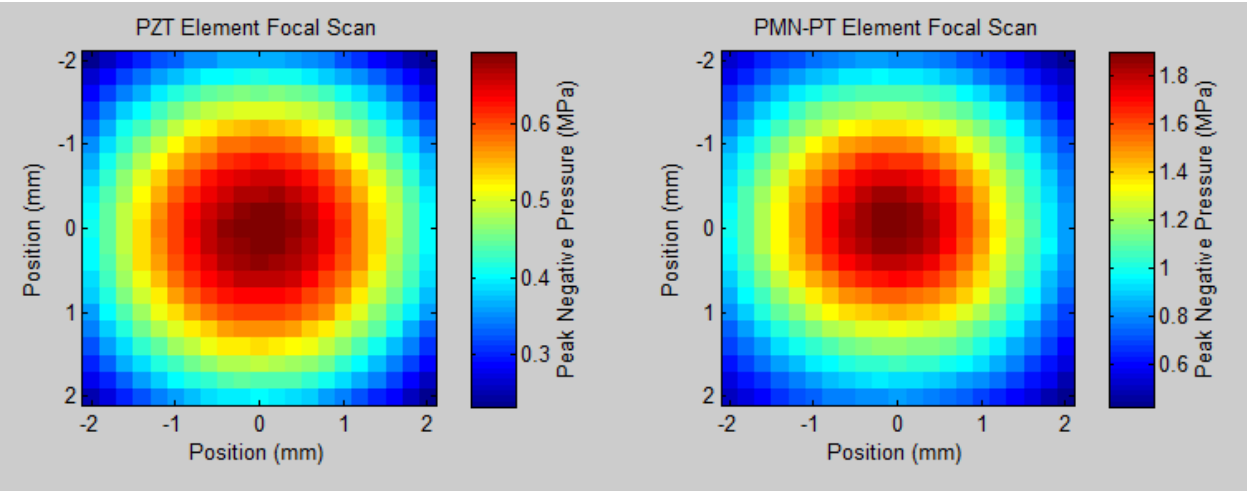

Figure 6-3: Focal pressure scans taken at the geometric focus of the lens ~ 65 mm from the transducer elements for the PZT-4 transducer (left) and the PMN-PT transducer (right).

To assess the performance at higher driving voltages (up to 1578 Vpp for the PMN-PT element, and 1781 Vpp for the PZT-4 element), pressure measurements were taken using a fiber optic hydrophone [2] at a single point near the surface and at the geometric focus. An example focal pressure waveform for the two transducers driven with the same peak to peak driving voltage (525 Vpp) is shown in Figure 6-4. In this case, the PZT-4 element produced a peak negative pressure of 2.5 MPa and the PMN-PT element produced a peak negative pressure of 3.4 MPa. These waveforms show well developed shock fronts impinging on the negative half cycles, indicating that acoustic saturation could be an issue for higher driving voltages, especially for the PMN-PT element.

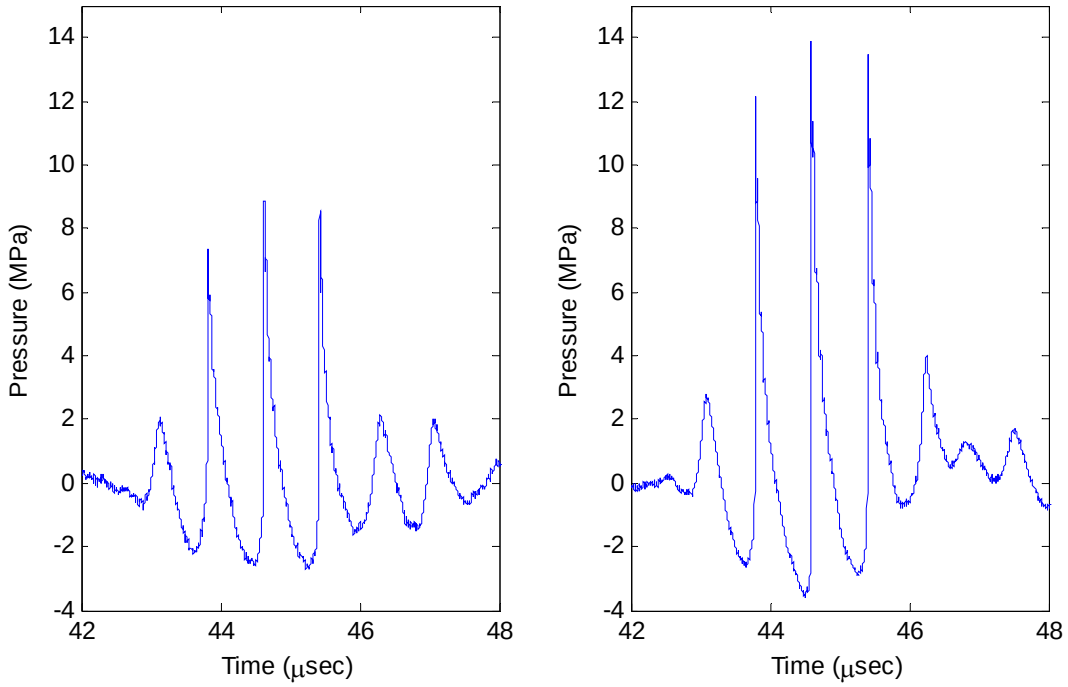

Figure 6-4: Pressure waveforms for the PZT-4 element (left) and PMN-PT element (right) when driven with 525 Vpp on the element.

Surface pressure and focal pressure versus driving voltage are shown in Figure 6-5. The PMN-PT transducer was able to generate nearly 7 MPa of surface pressure, versus roughly 3.8

MPa from the PZT-4 transducer. At this focal length and frequency however, the difference in focal pressure was not as drastic due to the effects of non-linear propagation. Focal pressure saturated at around 7.5 MPa for the PMN-PT with the PZT-4 element saturating around 5.2 MPa, for an improvement of around 44%.

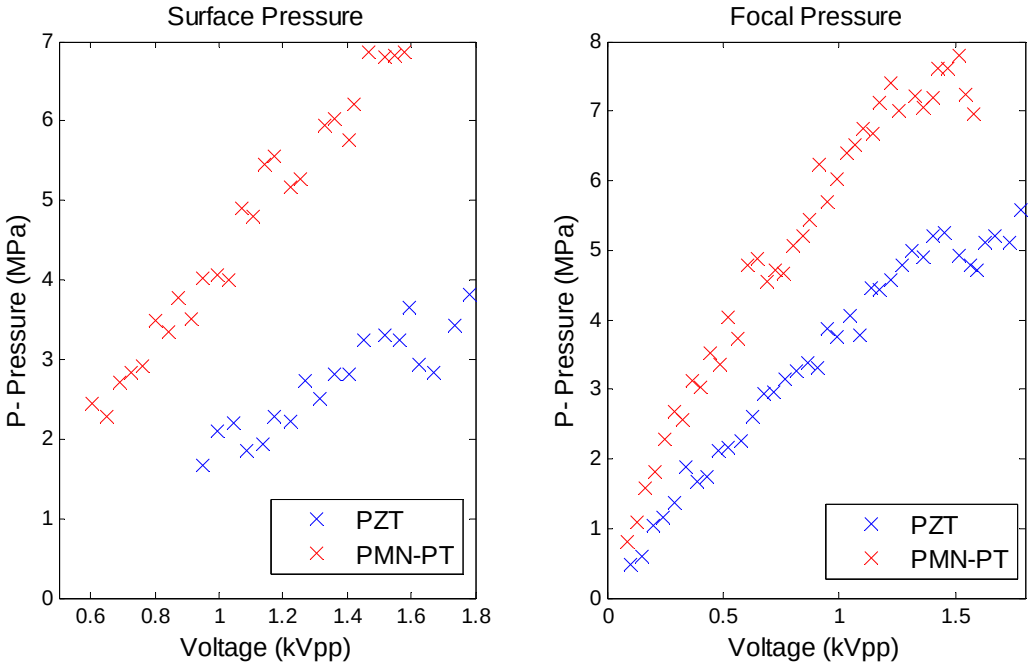

Figure 6-5: Peak negative pressure versus applied voltage for both transducers measured at the surface (left) and at the focus (right).

6.2.2 PZ36 Element Testing

A low impedance formulation of PZT (PZ36, Meggitt, Kvistgaard, Denmark) was tested for its potential use in histotripsy therapy transducers similarly to the previous section. The PZ36 elements were ordered in a 15 mm square size to facilitate better packing density in array designs, and therefore could not be directly compared to the previous set of experiments. A single element housing similar to those used in the PMN-PT testing was designed and constructed, with the only notable difference being the removal of the ¼ wavelength tungsten-epoxy matching

layer. The matching layer was not necessary due to the low acoustic impedance of the PZ36 material, allowing direct coupling to the lens material. These PZ36 elements started with an electrical impedance of 27 – j30.2 ohms and were electrically matched to about 10.4 ohms resulting in a voltage gain of about 3.2. Surface and focal pressure profile measurements were taken using a 500 micron "needle" hydrophone (HGL-0500; Onda Corp., Sunnyvale, CA) over a 15mm x 15mm region at the surface with the transducer driven with 656 Vpp and a 6mm x 6mm region at the focus when driven at 344 Vpp. Both scans were taken with 500µm separation between grid points. The 2D surface pressure profile for the PZ36 transducer is shown in Figure 6-6. The PZ36 produced a mean peak negative pressure of about 1.9 MPa over the 15 x 15 mm scan. The increasing pressure trend from top right to bottom left is likely the result of the transducer element not being entirely parallel to the scanned plane. This misalignment results in the hydrophone being closer to the transducer for some measurements.

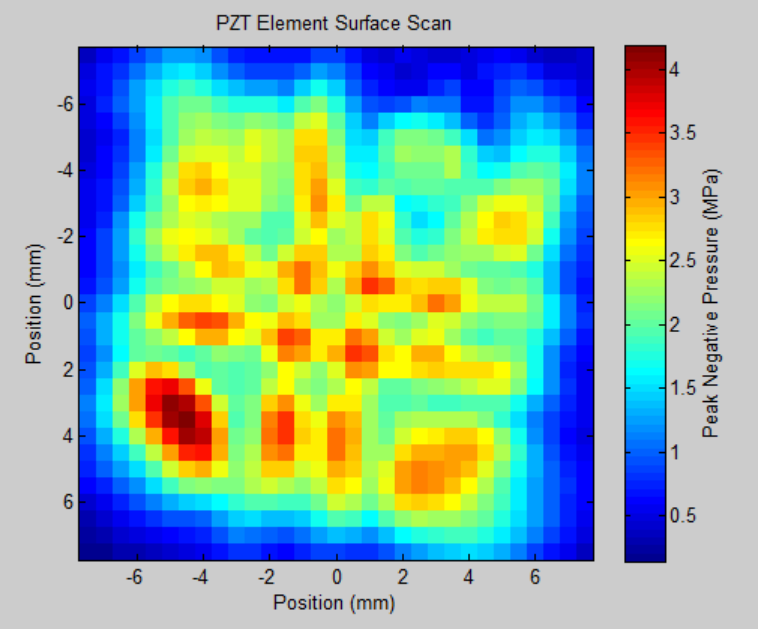

Figure 6-6: Surface pressure measurements taken ~5 mm from the transducer element for the PZ36 transducer driven with 656 Vpp.

Peak pressure measurements at the transducer focus were taken using the fiber optic hydrophone for peak to peak voltages on the element from 344 volts to 950 volts to determine the maximum pressure output. An example focal pressure waveform for the PZ36 transducer driven with a peak to peak driving voltage of 569 V is shown on the left in Figure 6-7. In this case, the PZ36 element produced a peak negative pressure of 2.7 MPa. Peak negative pressure versus driving voltage is shown on the right in Figure 6-7. The sample lost power output at driving voltages higher than 1000 Vpp, and was confirmed by comparison of the impedance before and after testing to have been irreparably damaged.

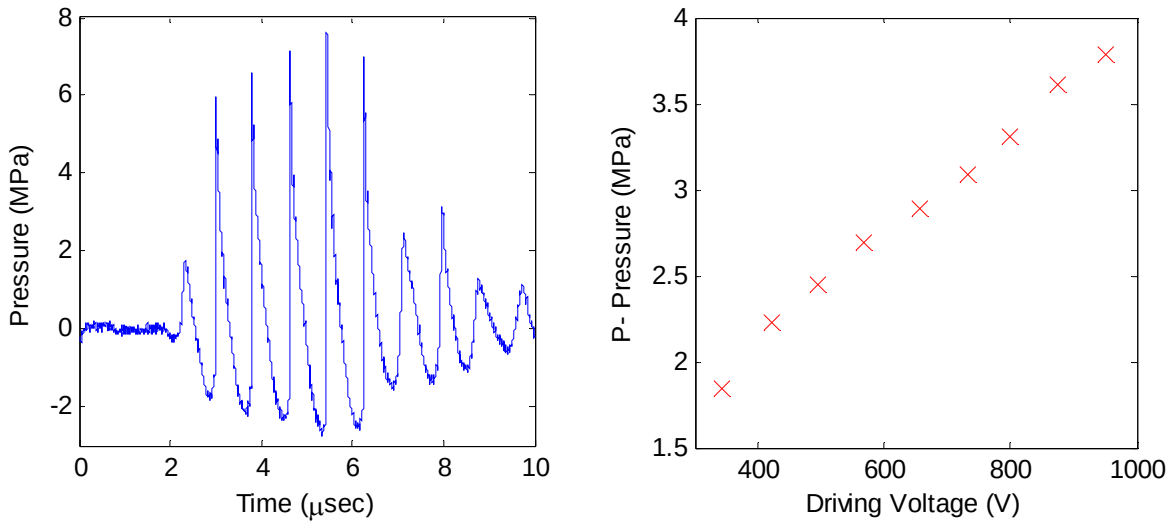

Figure 6-7: Peak negative pressure output of the 15 mm PZ36 element. An example pressure waveform (left) when driven with 569 Vpp on the element, along with the peak negative pressure versus driving voltage (right).

6.2.3 5 Element Array Design and Testing

An initial prototype transducer was designed and manufactured in house. This design (Figure 6-8 left) consists of five 2.25 cm square PZT-4 elements with acoustic matching and lens' aligned confocally, each with a 6.5 cm focal length. The elements were cut from the same 45mm plates described in the previous section. The working distance of the five element array is 4.5 cm,

the maximum housing dimensions are 6.5 x 8.5 cm, and the active aperture is about 5.1 x 7.1 cm. This design has an approximate 40% utilization of the transducer footprint (total element area divided by the area of the housing's footprint), and a 70% packing density (total element area divided by the usable front face area). A 12 MHz phased array imaging probe provision is aligned with the therapy focus lying on the imaging axis (Phillips S12) for therapy guidance using an available ultrasound imaging system. The focal widths of this 1.25MHz therapy transducer (-3dB from the peak pressure) are simulated to be 1.07 (lateral) x 1.83 mm (elevational) x 8.01 mm (axial) (Figure 6-8 right).

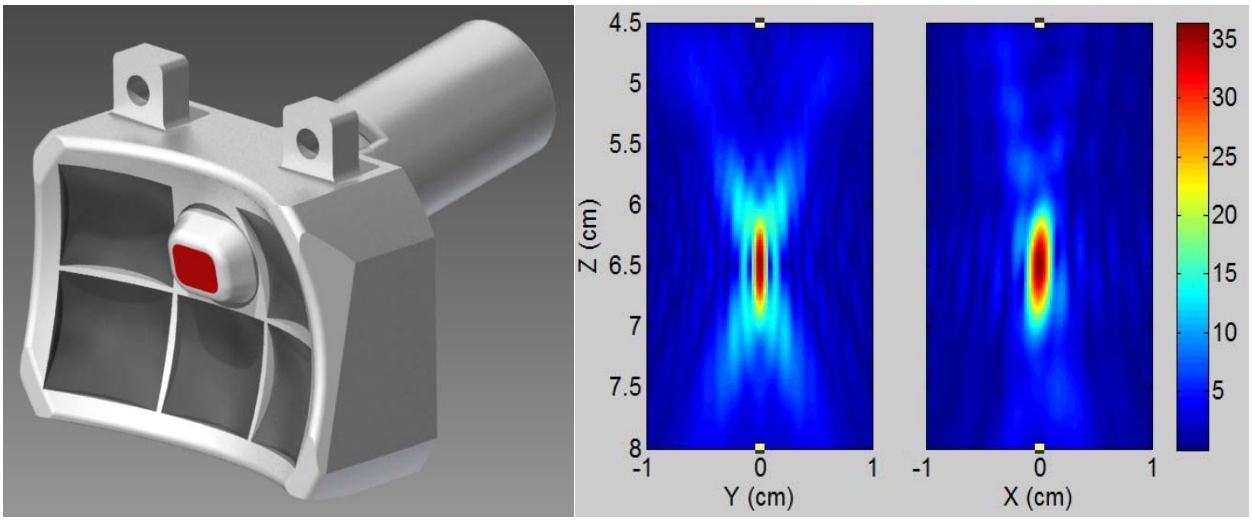

Figure 6-8: (Left) Rendering of the initial prototype transducer, with 5 piezo-ceramic transducer elements (dark gray) confocally aligned and a 12 MHz ultrasound imager aligned with the therapy focus along the imaging axis. (Right) 2D simulated focal gain pressure profiles for this configuration

The 5 elements were electrically matched to around 12 ohms impedance at 1.25 MHz, generating a voltage gain of approximately 3.5 and driven with a custom five-channel class D amplifier. The focal beam profile was measured using a "bullet" hydrophone with an 85 micron tip (HNR-0085, Onda Corp., Sunnyvale, CA). The measured focal beam profiles were slightly larger than those predicted by simulation, measuring roughly 1.31 mm (lateral) x 1.97 mm

(elevational) x ~9.5 mm (axial, extrapolated). This is likely explained by the wider focal zone of the PZT-4 elements that was observed in the single element testing in section 6.2.1.

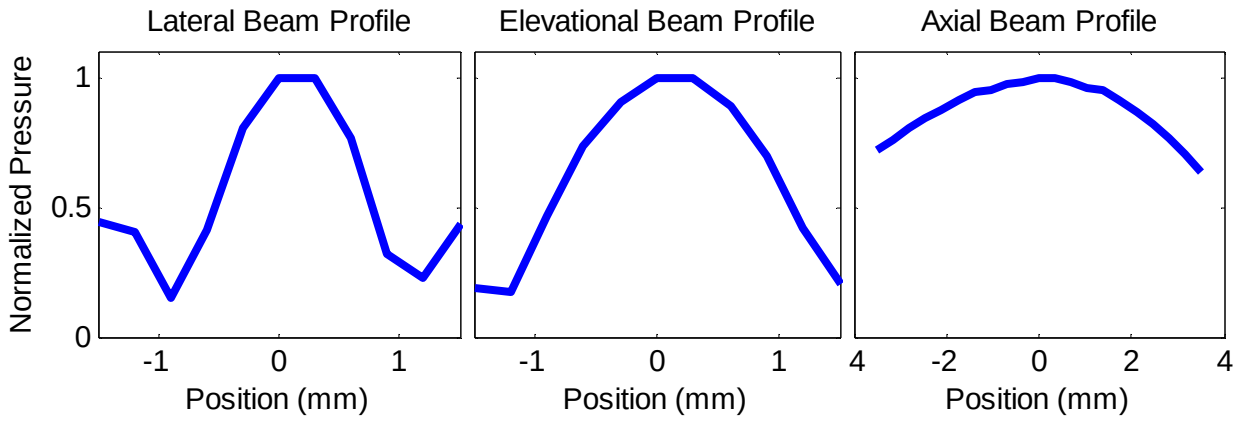

Figure 6-9: Normalized pressure profiles of the main lobe at the geometric focus for the 5 element transducer.

The maximum pressure output measured using a fiber optic hydrophone for voltages between 70 and 1050 Vpp. The transducer was able to achieve maximum pressure output when driven with 6 cycles from a five-channel class D amplifier, generating peak negative pressures up to 22 MPa (Figure 6-10) as measured with a fiber optic hydrophone. The pressure output appeared to saturate at this point, likely due to non-linear propagation of the large peak positive shockwave impinging on the negative half-cycle. This is consistent with the single element testing, where the pressure appeared to saturate around 5 MPa at the focus of a single element. That element was slightly smaller than the elements used here, and therefore required higher voltage to achieve that pressure. For this reason, even though the elements could be driven up to 1400 VPP, increased focal pressure was not observed for applied voltages over 820 V peak to peak in water. The ability to apply higher voltages is however necessary in the case of attenuating media, where increased surface pressure will be necessary to achieve similar focal pressures.

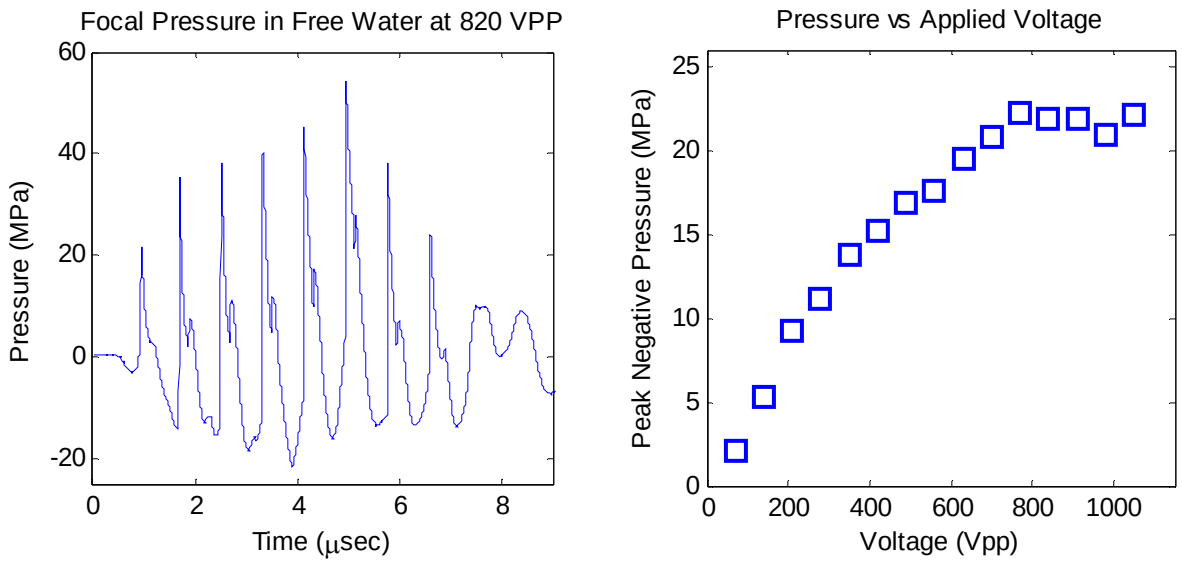

Figure 6-10: Focal Pressure for the 14 element transducer measured at 820 Vpp (left) with the peak negative pressure versus applied voltage (right) all measured using a fiber optic hydrophone.

This design was then evaluated for use in the ongoing feasibility studies for histotripsy in pediatric cardiac applications. The transducer was fired through 2.5 cm of porcine ribcage and muscle tissue *in vitro*, were it was demonstrated to be capable of sustaining a bubble cloud through 2.5 cm of porcine ribcage and muscle tissue *in vitro*, performing comparably to the 1 MHz annular array transducer used for the *in vivo* neonatal porcine ventricular septal defect creation studies in Chapter 2. An *in vivo* study targeted the ventricular septum, mirroring the procedures outlined in Chapter 2 with this new transducer replacing the larger 9 cm aperture 1 MHz transducer used for that work. In this study, the transducer provided 4 separate treatments totaling 7.5 minutes of therapy on the ventricular septum, after which the presence of a newly created VSD was confirmed by color-flow Doppler observation of a flow channel between the ventricles.

A second *in vivo* experiment used the same setup, only targeting the atrial septum for defect creation. In this case, the transducer could not reliably generate a cavitation cloud on the

atrial septum, suggesting the need for a more powerful transducer. Having the imaging transducer off the therapy axis proved to be sub-optimal in these *in vivo* studies as well, as in certain cases cavitation was audible but could not be visualized on ultrasound imaging. This was likely due to the cloud forming slightly in front of or behind the geometric focus, which is outside the imaging field for all imager rotational orientations besides aligned with the axial-elevational plane of the therapy transducer.

6.2.4 14 Element Array Design

A second prototype was designed and manufactured using smaller elements to facilitate denser element packing for increased active area. The use of more, lower pressure elements that interact only very near the transducer focus should reduce the nonlinear acoustic saturation effects as well. This transducer (Figure 6-11) consists of fourteen 1.5 cm square elements cut from the same 4.5 cm PZT-4 plates as the previous transducer with acoustic matching and lens' aligned confocally, each with a 6.5 cm focal length. The working distance of the fourteen element array is 4.5 cm and the maximum housing dimensions are 6.2 x 9.0 cm. In this case, the 12 MHz phased array imaging probe provision is centered in the therapy transducer, with the imaging axis aligned with the therapy axis. This design has an approximate 49% utilization of the transducer footprint with active area and a 73.3% packing density. This is a slight improvement in packing density over the previous design, but more importantly, an increase of over 600 mm^2 of active area.

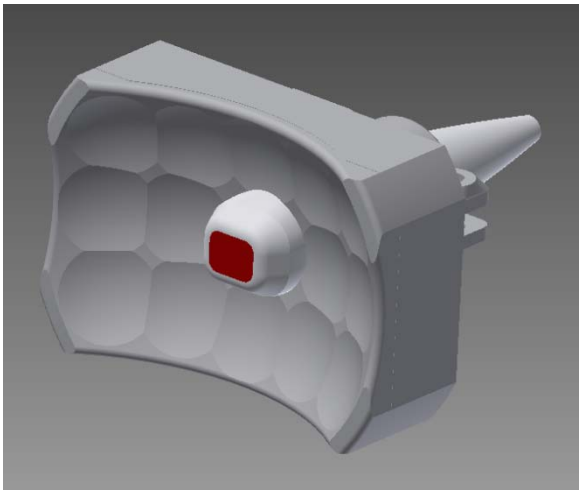

Figure 6-11: Rendering of the second prototype transducer with 14 piezo-ceramic transducer elements confocally aligned and a 12 MHz ultrasound imager aligned directly with the therapy axis.

The 14 elements were electrically matched to around 5 ohms impedance at 1.25 MHz, resulting in a voltage gain of around 5.2. This increased the potential peak to peak voltage that could be applied to the elements to around 2000 V. The focal beam profile was measured using the same 85 micron "bullet" hydrophone, and was very similar to the 5 element transducer due to their similar shape and identical frequency and focal length. The focal widths measure roughly 1.23 mm (lateral) x 1.82 mm (elevational) x ~9.5 mm (axial, extrapolated). The 2D lateral/elevational beam pattern at the axial focus is shown on the left in Figure 6-12 along with 1D profiles in the 3 principle axes. All measurements where done with the "bullet" hydrophone.

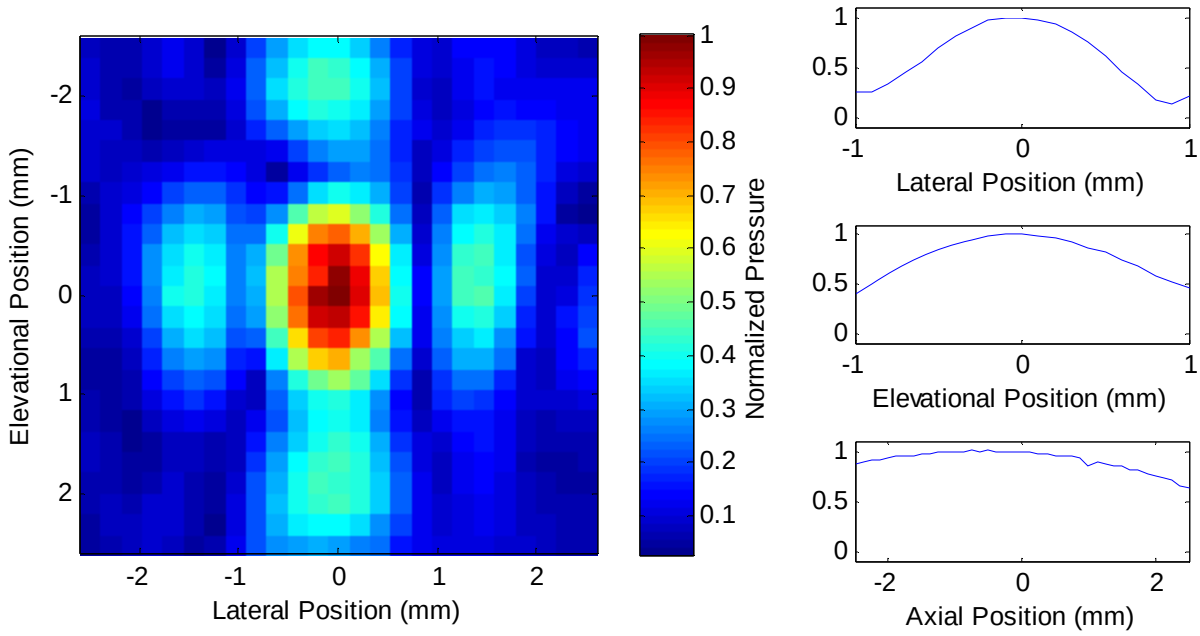

Figure 6-12: 2D beam profile of normalized peak negative pressure around the geometric focus of the 14 element transducer.

The maximum pressure output was estimated by summing measurements of the output of 4 groups of elements using a fiber optic hydrophone. The 14 elements were divided into 4 groups of 3-4 elements. The 3 middle elements on the top and bottom made up the first 2 groups, and the remaining 4 elements on each side made up the other 2. Groups were composed of adjacent elements to preserve as much of the impact of non-linear interaction between elements as possible. This transducer was able to achieve maximum pressure output when driven with 5 cycles from a fourteen-channel class D amplifier, generating estimated peak negative pressures up to 32 MPa. Pressure waveforms with all elements firing could only be taken up to 910 Vpp, where the transducer generated about 21.5 MPa peak negative pressure (left of Figure 6-13), as higher negative pressures generated cavitation on the hydrophone's fiber tip that corrupted the measurements. Estimated pressure from summing the output of 4 groups of elements agreed well with direct measurements up to this point (right of Figure 6-13). Additional non-linear

propagation losses are likely with all elements firing however, and the actual pressure output is likely lower than these estimates at very high driving voltages.

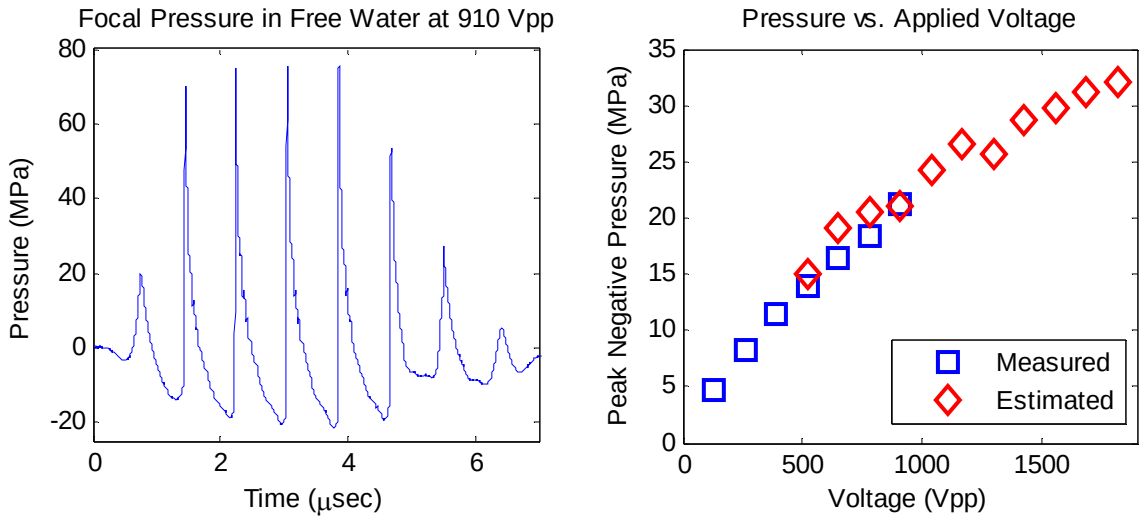

Figure 6-13: Focal Pressure for the 14 element transducer measured directly at 910 V (left) with a comparison of the peak negative pressure measured directly vs the extrapolation from summing the output of 4 subgroups of elements (right) all measured using a fiber optic hydrophone.

This design was also evaluated for use in the ongoing feasibility studies for histotripsy in pediatric cardiac applications. The transducer was used in a series of *in vivo* validation experiments targeting the atrial septum in a neonatal porcine model with various augmentations to reduce pre-focal lung obstruction. In these studies, the transducer was often able to generate a cavitation cloud on the atrial septum, however sufficient treatment time to generate an ASD was not possible secondary to deteriorating lung function. This was likely due to increased overlying lung tissue in the pre-focal acoustic field when targeting the atrial septum versus targeting the ventricular septum. Augmentations to the model to remove pre-focal lung obstruction improved treatment times, but could not completely prevent lung damage.

6.2.5 19 Element Transducer Design

A final prototype transducer was designed in cooperation with a transducer manufacturing company (Imasonic, S.A., Besançon, France). Professional manufacturing was utilized since their fabrication techniques allow for arbitrarily shaped and sized elements, facilitating both increased element packing density and steerable array designs. A limitation of fixed focus designs is that they must be designed to accommodate the maximum possible working distance, and therefore are most often used with a significant standoff from the patient when targeting individuals with a shallower target depth. This standoff reduces ultrasound image quality and therapy focal gain. A steerable design is optimal, such that the therapy probe can always be positioned against the skin, and the focal location steered to the target depth. For this reason, the prototype transducer was designed with the elements arranged within 6 concentric rings, allowing focal steering along the therapy axis. These rings were divided into equal area sections to allow for easy and consistent electrical matching and amplifier integration. The rings were also truncated to match the roughly rectangular acoustic window in the human neonate Figure 6-14. The transducer was designed with a 60 mm focal length, since this resulted in the highest focal gain over the estimated anatomical range of working distances. The simulations of the pressure field and steered focal gain are shown in Figure 6-15.

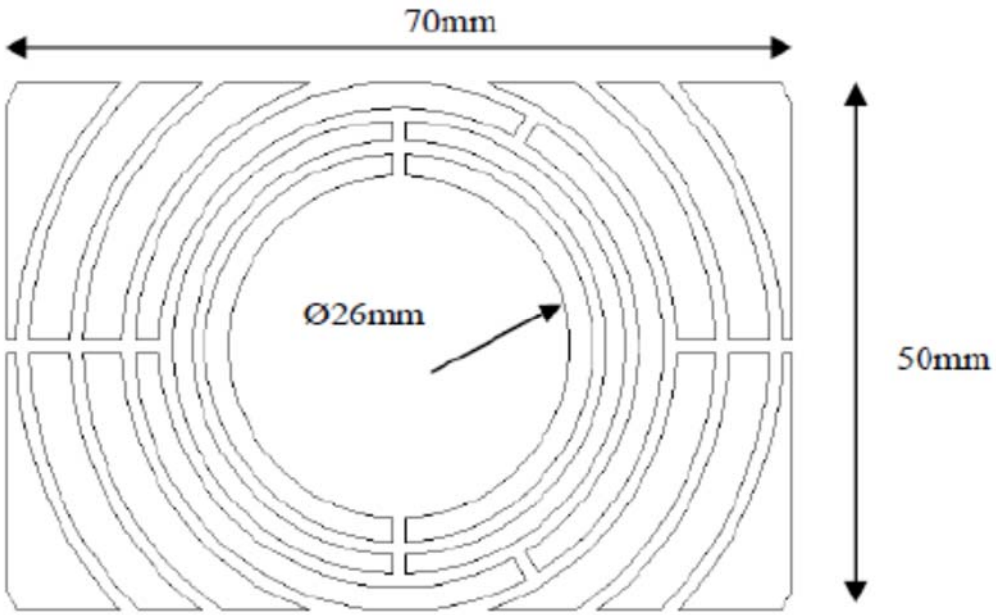

Figure 6-14: Diagram of the axis-steerable therapy array design. 19 elements of equal area are arranged into 6 concentric rings. The aperture is truncated into a 5 x 7 cm rectangle with a 2.6 cm diameter center hole for the ultrasound imaging transducer.

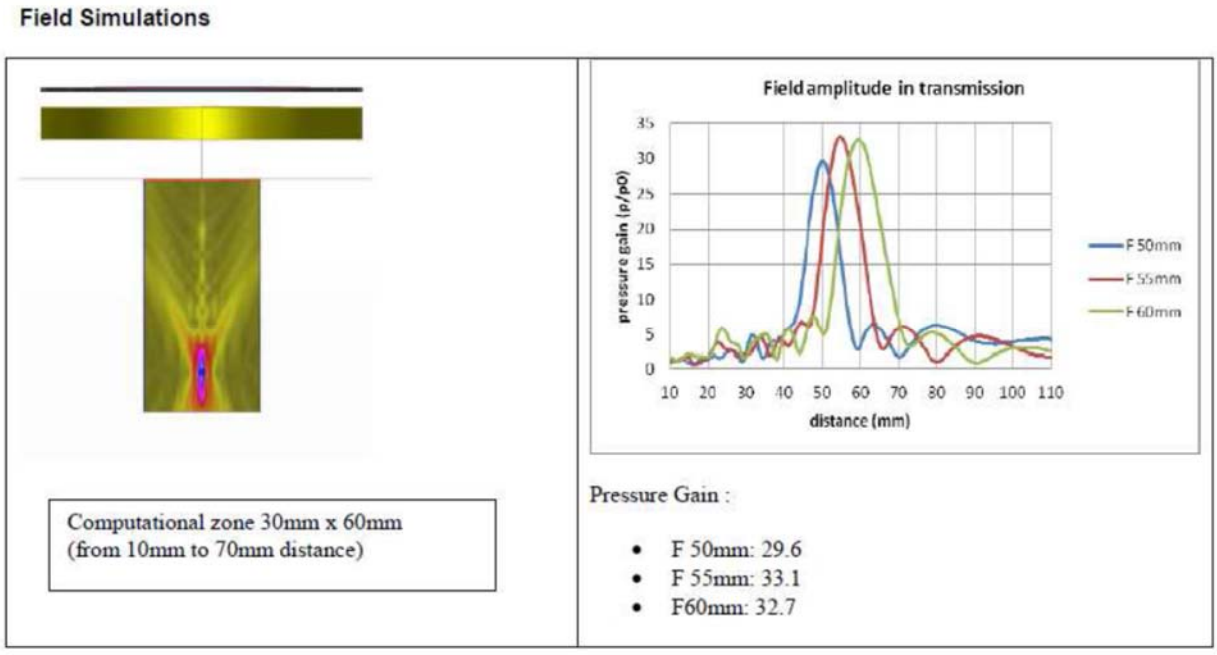

Figure 6-15: Simulation results for this 19 element, 1 MHz array transducer showing the pressure field (left) along with the steered pressure gain for steered focal lengths of 50, 55, and 60 mm.

The transducer housing was designed to minimize the lateral dimensions, and resulted in a housing of 6.2 x 7.6 cm. This design has 19 elements of 155 mm^2 (2945 mm^2 total), resulting in a 64% utilization of the transducer footprint with active area and a 90% packing density. The housing included a center hole provision for a ultrasound imaging transducer that will be detailed later in this chapter.

The transducer was manufactured and delivered by Imasonic, and configured for testing with a 19 channel class D amplifier system. The element impedance was measured to be 120±3.4 ohms real part, and -234±4.5 ohms imaginary part. The elements were matched to approximately 22 ohms using an "L-C" matching network, resulting in a voltage gain of about 3.5. The focal beam profile was measured using a 500 micron "needle" hydrophone (HNR-0500, Onda Corp., Sunnyvale, CA). The beam profile for the 19 element array transducer was again very similar to the previous transducers due to their similar shape. In this case however, a lower frequency (1 MHz here vs 1.25 MHz previously) and smaller aperture (5 x 7 cm with this design versus 8.1 x 5.3 cm of the 14 element array) resulted in the focal zone being slightly larger. The focal widths measure roughly 1.51 mm (lateral) x 2.17 mm (elevational) x 9.9 mm (axial). The 2D lateral/elevational beam pattern at the axial focus is shown on the left in Figure 6-16 along with 1D profiles in the 3 principle axes. All measurements where done with the "needle" hydrophone.

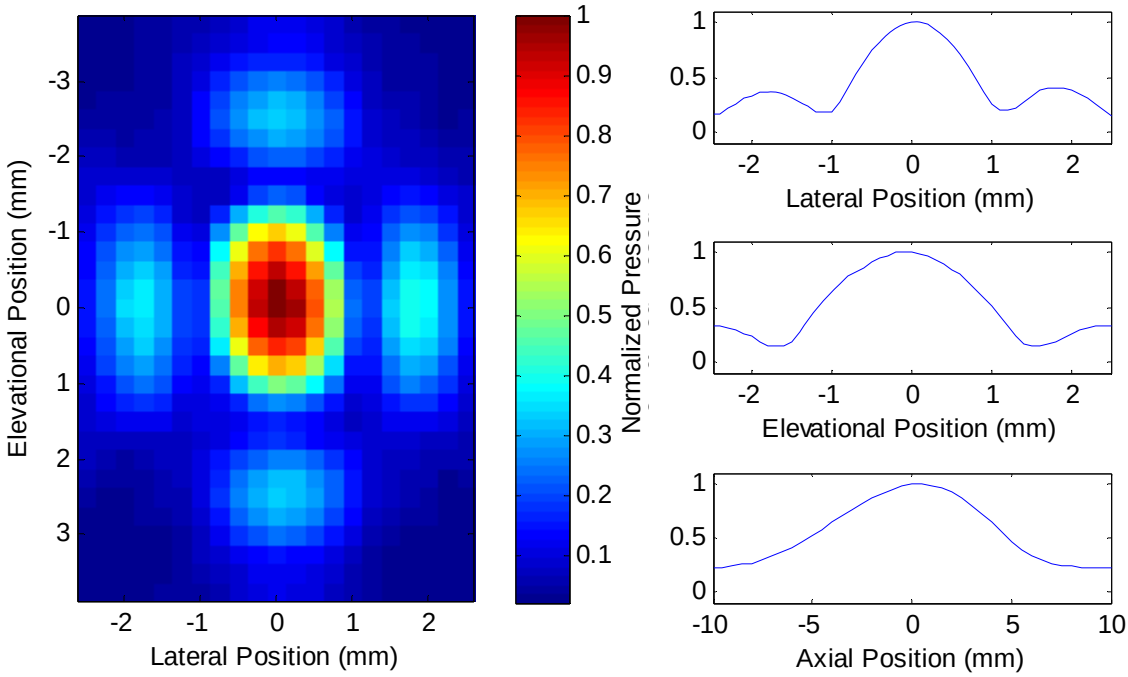

Figure 6-16: Normalized 2D peak negative pressure profile in the lateral/elevational planes at the axial focus (left), along with 1D scans on the principle axes (right) as measured with the "needle" hydrophone.

Maximum pressure output was estimated by summing measurements of the output from 2 groups of the elements using a fiber optic hydrophone. These two groups were composed of the two halves of the transducer, split along the axial/elevational plane, resulting in groups of 10 and 9 elements. The extra element in one group results from the ring that is split into 3 elements, as opposed to the others rings that are split into 2 or 4 elements (Figure 6-14). This transducer was able to achieve maximum pressure output when driven with 3 cycles from a nineteen-channel class D amplifier, generating estimated peak negative pressures up to 40 MPa. Pressure waveforms with all elements firing could only be taken up to 588 Vpp, where the transducer generated about 24 MPa peak negative pressure (left of Figure 6-17). Estimated pressure from summing the output of 2 groups of elements agreed well with direct measurements up to this point (right of Figure 6-17). Summing the acoustic output from only 2 groups of elements should

maintain most of the effects of non-linear propagation in this case; however, additional losses are possible with all elements firing. For this reason, the actual pressure output is likely close, or slightly lower than these estimates at very high driving voltages.

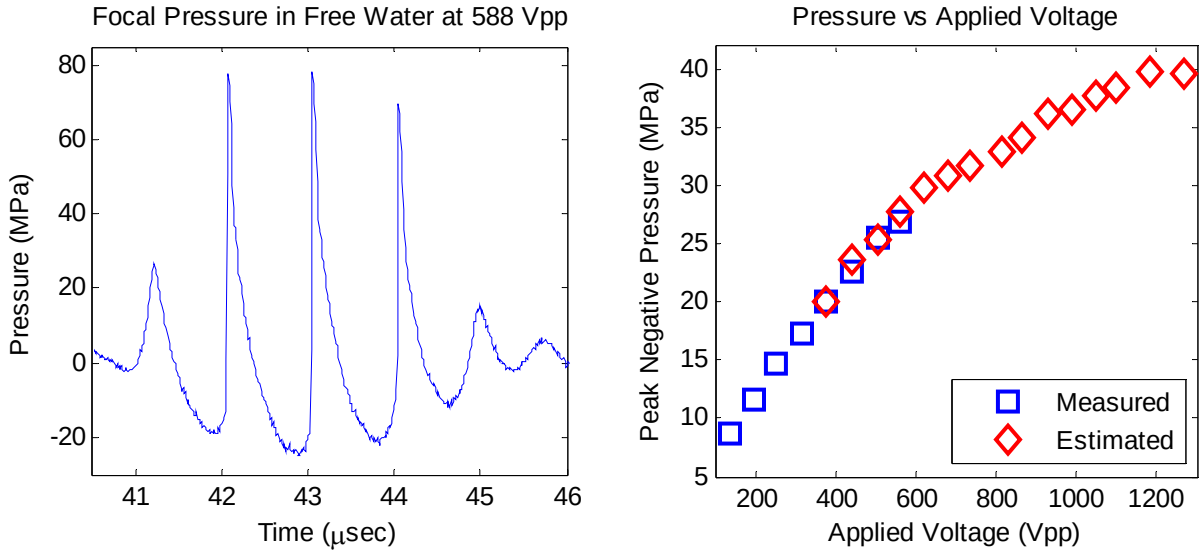

Figure 6-17: Focal Pressure for the 19 element transducer measured directly at 588 Vpp (left) with a comparison of the peak negative pressure measured directly vs the extrapolation from summing the output of 2 subgroups of elements (right) all measured using a fiber optic hydrophone.

This design of the transducer and water box resulted in a working distance of 36.25 mm, and the HLHS application requires working distances between 30 and 45 mm. This would require a minimum steered focal length of 53.75 mm, and a maximum steered focal length of 68.75 for this transducer. To assess the impact of steering on pressure output, the transducer was steered over 5 points within this range at identical driving voltages of 319 Vpp and focal pressure waveforms were acquired using the fiber optic hydrophone and compared to the pressure output at the geometric focus. The peak negative pressure over the required steering range is plotted in Figure 6-18, relative to the pressure achieved at the geometric focus. Focal pressure varied over the steering range from 81% to 108% of the peak negative pressure at the geometric focus.

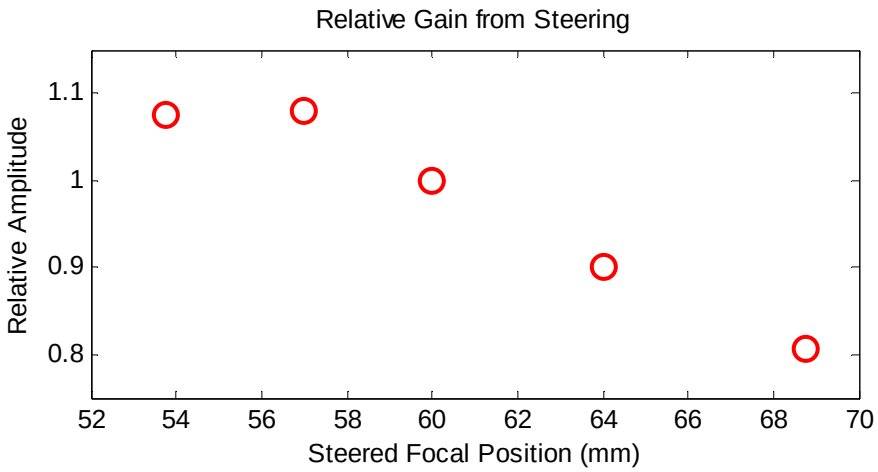

Figure 6-18: Peak negative pressure over the required steering range relative to the geometric focus, showing a relative gain between 0.81 and 1.08 over the entire range.

6.3 Integrated Histotripsy Therapy Cart

6.3.1 Ultrasound Imaging System

Ultrasound is the imaging modality most often used to visualize structures and blood flow in the neonatal heart. Ultrasound imaging is inexpensive, fast, and flexible. The ultrasound imaging for this system must be able to accept synchronization from an external source since imaging during therapy will be required for therapy monitoring. This synchronization will eliminate interference from the high intensity histotripsy therapy pulses, increasing ultrasound image quality for therapy monitoring. Histotripsy therapy will be applied at a pulsing rate determined by safety and efficacy analysis, so the imaging sequence must be flexible enough to acquire between therapy pulses at a broad range of repetition rates. Custom image sequence modification will also be necessary to allow for the potential addition of imaging, guidance and feedback optimizations for this specific application that would not be possible with an "off the shelf" clinical ultrasound imaging system, including those developed in this work (Chapter 4, Chapter 5).

The Ultrasonix SonixTouch system is available in a research configuration, allowing arbitrary acquisition of frames or scan lines, custom probe compatibility, and full image sequence customization. This system has been used successfully previously by Histosonics Inc. in an integrated histotripsy therapy system for ultrasound image guidance and targeting in treating benign prostate hyperplasia (BPH).

To limit the loss of active area in the therapy transducer, a small imaging probe is essential. The ultrasound imaging probe must be capable of imaging structures and blood flow in the neonatal heart through the subcostal acoustic window with the estimated 3-4.5 cm of overlying tissue in the acoustic path. Clinically, a high frequency (> 5 MHz) phased array probe would be used for this scenario. The probe must be compatible with the chosen imaging system, and ideally, the probe housing would have a cylindrical shape to allow easy translation and rotation within a cylindrical hole in the therapy transducer.

A custom phased array imaging probe was ordered from Vermon SA. The 64 element probe would have a center frequency of 4.9 MHz and 4 MHz bandwidth. This was the highest center frequency that their manufacturing techniques allowed. The probe was designed with a 20 mm cylindrical housing, 64.2 mm long with a 2 m cable to an Ultrasonix connector Figure 6-19 shows a detailed drawing of the probe design.

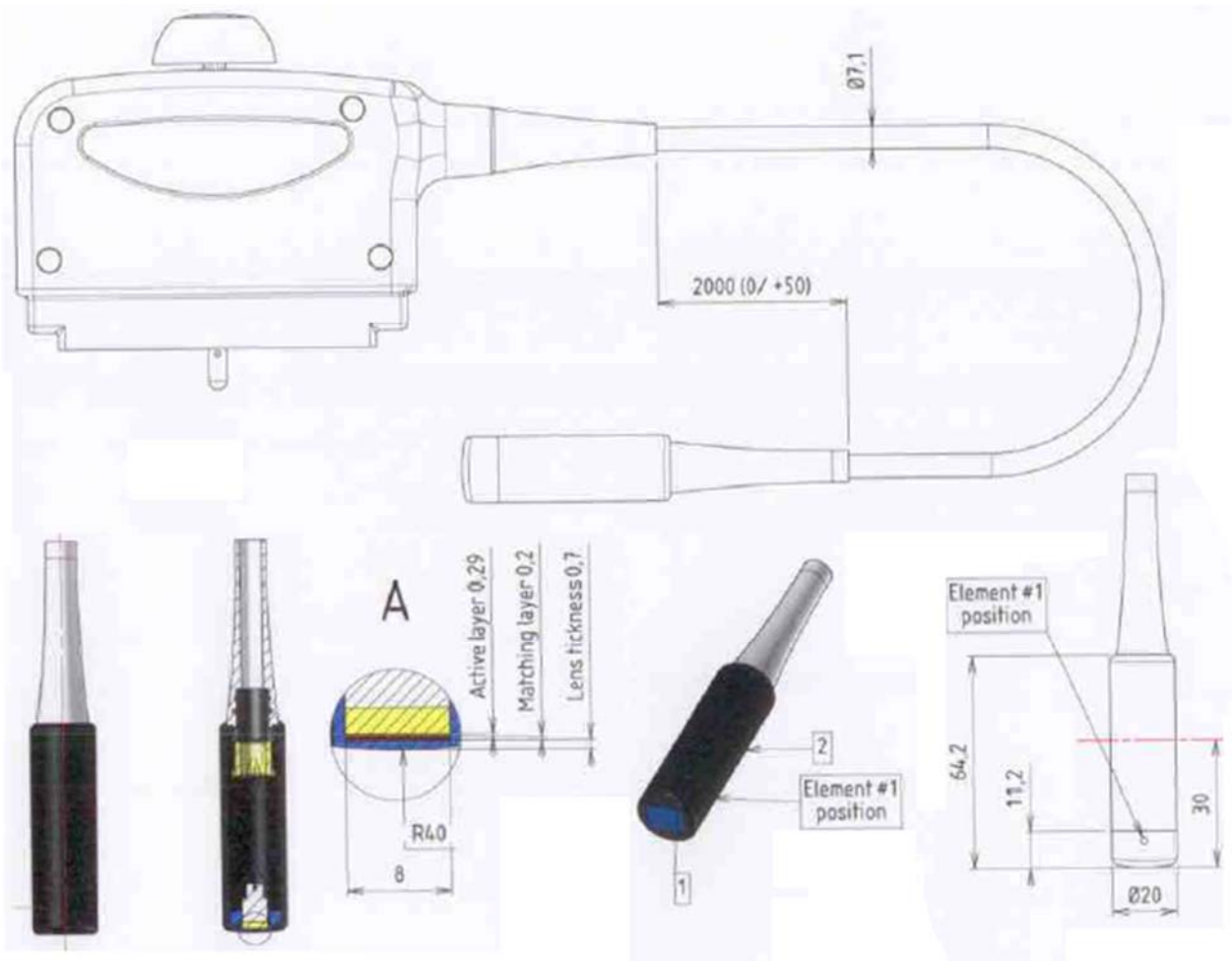

Figure 6-19: Detailed drawing of the custom image transducer, a 4.9 MHz phased array with 4 MHz bandwidth.

The custom PA7-4 imaging transducer was integrated into the Ultrasonix SonixTouch system, and a basic imaging study performed on an adult volunteer. Figure 6-20 shows an image of the custom built transducer on the left and a sample ultrasound image of the carotid artery of an adult volunteer taken with the transducer on the right.

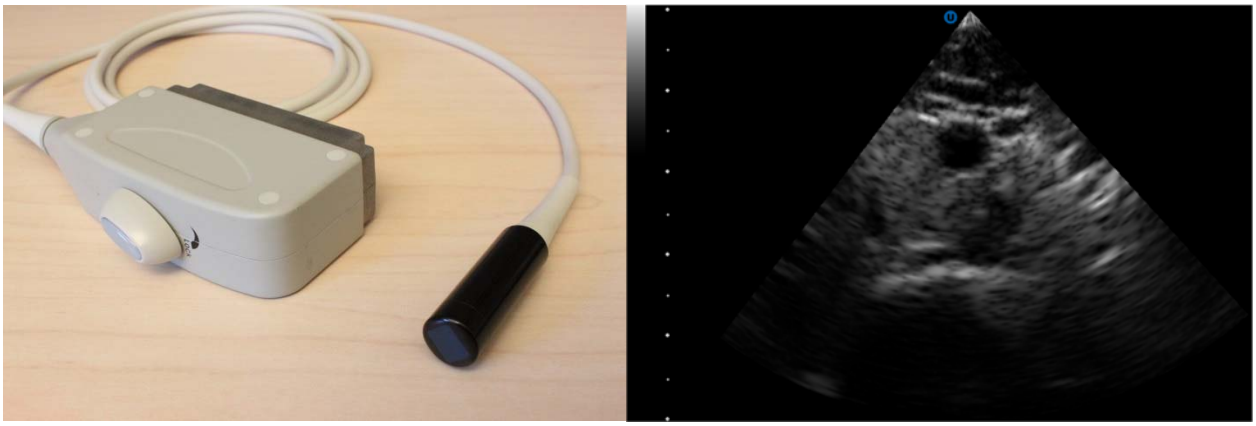

Figure 6-20: Image of the custom PA7-4 transducer (left) along with an example image taken with the transducer of the carotid artery of an adult volunteer.

6.3.2 Ultrasound Coupling Device

To ensure efficient transfer of acoustic energy from the therapy and imaging transducers into the patient, a water box coupling system was designed. This water box coupler design simply extends the transducer housing evenly beyond the curved transducer face to form a flat front surface. This device was designed to preserve as much of the original working distance of the transducer as possible, though a loss of 2.7 mm of working distance was required. A thin flexible membrane will be affixed over the front opening to couple directly to the patient's skin via ultrasound gel. A thin imager sheath with 3 rubber "o-rings" will be sealed to the imaging transducer so the cavity between the transducer and the front face of the coupling box can be filled with water for coupling. Figure 6-21 shows the detailed design drawings of the housing, imager sheath and water box.

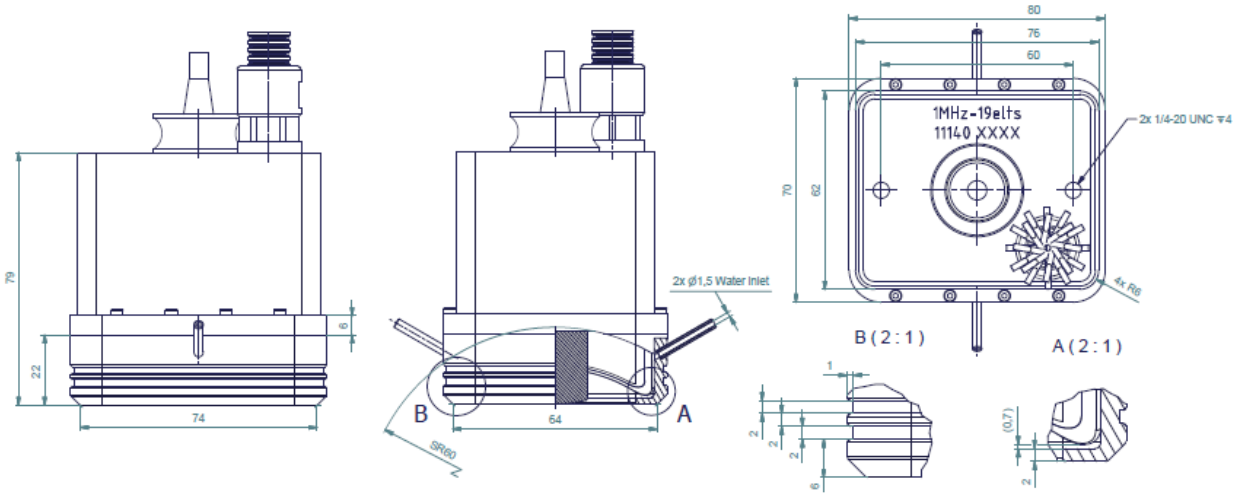

Figure 6-21: Detailed drawing of the 1 MHz, 19 element array transducer design. The main housing measures 6.2 x 7.6 cm (not counting the 2-4 mm mounting shoulder for the coupling box).

With the imager sheath, the ultrasound imager can be rotated or extended freely in the center hole of the therapy transducer, while maintaining a water-tight seal between the imager and therapy transducer. Figure 6-22 shows the imager sheath along with the imager mounted in the therapy transducer with the water box coupler attached. When telescoping, the inner volume of the water box will change. The small tube on the top and bottom of the water box are for connections to a water reservoir to allow flow in and out of the cavity during telescoping to allow this without affecting the coupling to the patient. Positive water pressure on these ports may also be useful to expand the front membrane and improve coupling to uneven surfaces.

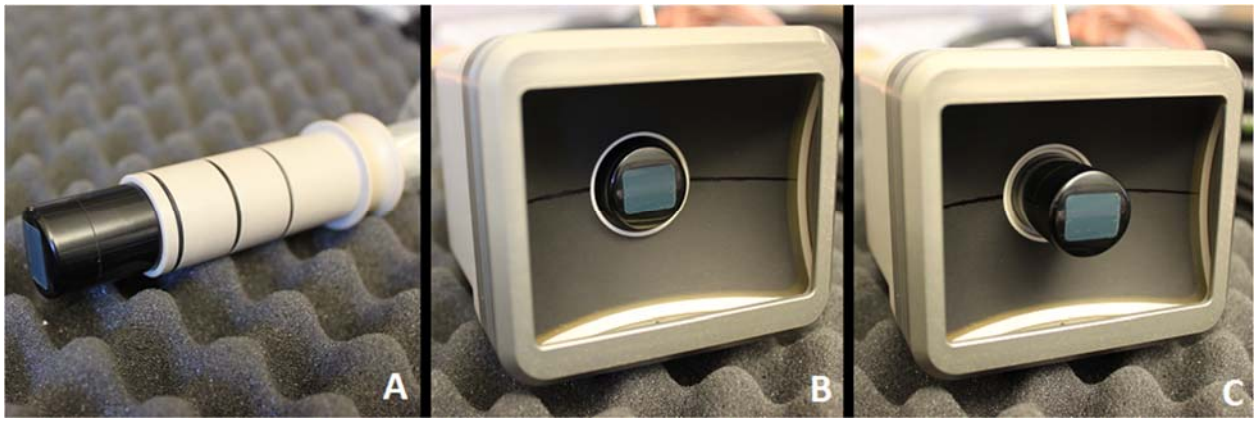

Figure 6-22: Ultrasound imaging transducer with sheath (A) with rubber "o-rings" to form a watertight seal with the therapy transducer while maintaining the ability to telescope from a retracted position during therapy (B) to an extended position in direct contact with the patient's skin (C) for better image quality during pre- and post-treatment imaging studies.

6.3.3 Therapy Generator and Controller

The therapy transducer requires a multi-channel, high power amplifier to generate the high amplitude acoustic pulses necessary for histotripsy therapy. An amplifier for this application should allow a configurable number of channels, independent phasing of at least a subset of those channels, and should be able to produce a synchronization output appropriate for the imaging system. This amplifier must be able to generate high voltage (>1500 V peak to peak) and handle high instantaneous current (>30 A) on all channels to ensure that the therapy transducer can be driven to its maximum pressure output. Therapy will be applied at low duty cycles (< 1%) so time average power and thermal concerns should be minimal. The controller should allow a maximum center frequency of at least 1.5 MHz, a maximum of at least 10 cycles per burst, and at least 1000 Hz maximum burst repetition rate. Ideally, the therapy generator would also be built within the relevant electrical safety requirements for easier transition to clinical research.

A custom histotripsy generator and controller meeting these requirements has been developed previously by Histosonics Inc. and integrated into an expanded chassis Ultrasonix SonixTouch system. The therapy generator can provide up to 1700 V peak to peak on up to 36 channels up to 250W total power. The histotripsy control software, called Histotripsy Service Tool, is installed directly into the Ultrasonix host computer and supports main frequencies between 500 kHz and 3 MHz, 1 to 100 cycles per burst, and a burst repetition rates between 1 Hz and 100 kHz. The 36 total channels are divided among 6 boards, and each of these boards can have independent phasing set by the histotripsy controller. This system was chosen as the foundation for the integrated therapy system described in this chapter.

6.3.4 Transducer Mounting and Positioning

A positioning system is required to mount the integrated therapy unit to the mobile chassis. The positioning arm should include some means to coarsely position the therapy unit over the patient's abdomen, and a motorized fine positioning mechanism to accurately place the therapy probe focus on target. The positioning arm will need to support both the weight of the micro-positioning system and the estimated maximum 5 lb weight of the integrated therapy unit. The micro-positioning system should be able to translate the therapy unit at least 5 cm in 3 orthogonal dimensions, with a minimum positioning accuracy of 100 microns. One axis should be aligned with the therapy/imaging axis. This will allow direct mechanical adjustment along the steering axis, and make positioning more intuitive for the operator based on the ultrasound imaging feedback. The mechanical micro-positioner should include joystick control, along with direct positioning commands through a console on the host computer. These positioning commands should include commands to move each axis, read the position of each axis, and store and easily return to a "home" position.

A positioning arm meeting the requirements for the macro-positioning arm comes integrated into the expanded chassis Ultrasonix SonixTouch system chosen previously. A micro-positioner was developed matching our requirements to mount directly to this positioning arm. The final stage would include a direct mount for the 19 element array transducer developed in the previous section.

The completed integrated therapy probe was then mounted to the last stage of the 3 axis micro-positioner. This assembly was mounted to macro-positioning arm of the extended chassis therapy cart and is shown in Figure 6-23. With the water-tight front membrane attached to the water box, the integrated probe can be coupled directly to the patient's skin via ultrasound gel. This completed the assembly of the integrated histotripsy therapy system for pediatric cardiac applications, and the final device is shown in Figure 6-24.

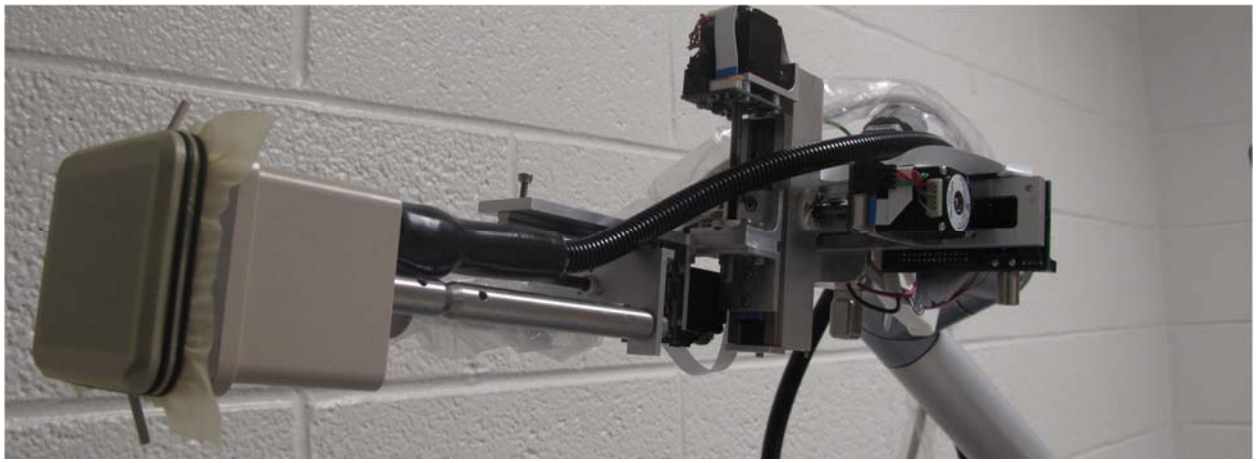

Figure 6-23: Complete integrated probe mounted to the 3 axis micro-positioner at the end of the macro-positioning arm.

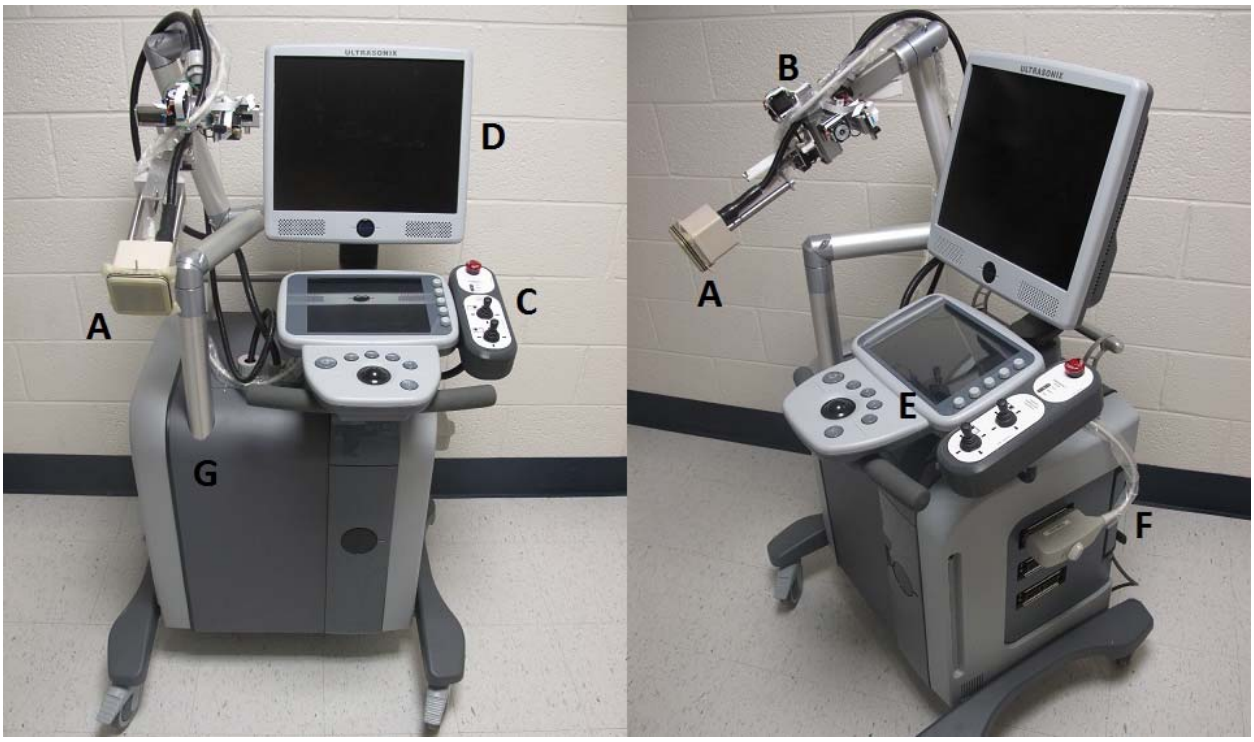

Figure 6-24: Completed integrated histotripsy therapy system. The integrated probe (A) includes the therapy transducer, coaxial imaging transducer and ultrasound coupling water box. The probe is mounted directly to the motorized micro-positioner (B) and manipulated by joystick (C) or direct commands through the console (D). Rough positioning of the probe and micro-positioner is accomplished by the manual positioning arm which is rigidly mounted to the cart chassis (G). This extended chassis (G) houses the therapy amplifiers and power supply, along with ultrasound imaging system (F), which is controlled through the touch panel (E) with images displayed on the main console (D).

6.4 Discussion

In this chapter several materials were tested for their potential in replacing PZT-4 for use in custom manufacturing of transducers in house. The PMN-PT single crystal consistently produced over twice the surface pressure of the comparably sized PZT-4 element at the same driving voltage, peaking at nearly 7 MPa of surface pressure. However, this increased output also led to increased acoustic saturation effects from nonlinear propagation. Surface pressures near 7 MPa only resulted in focal pressures of less than 8 MPa for this focal length, despite the linear focusing gain of around 5 from the acoustic lens. This could potentially lead to significant

prefocal heating for these elements. These elements are much more expensive than PZT elements, costing several hundred dollars each versus the 5-20 dollars per element that PZT elements typically cost. These elements are also difficult to manufacture in this frequency range and below, due to fact that a single crystal must be grown to the full thickness. Based on these factors, these elements were not ideal for a transducer for this application, but should be considered for applications that require miniaturized, high frequency, short focal length histotripsy transducers in the future.

Also of note from the PMN-PT material test was the increased focusing achieved versus the PZT-4 samples, despite the identical size, driving frequency, and acoustic lens (-6 dB beam width of 2.72 mm for the PMN-PT versus 3.18 mm for the PZT-4). A possible explanation can be formed based on the surface pressure profiles (Figure 6-2), where the PMN-PT produced a very even pressure field out to the edges, while the PZT-4 had reduced output near the edges. This made the radiating surface of the PZT-4 element smaller, effectively increasing the f-number of that transducer. This could also contribute to the increased focal spot size that was observed for the 5 element array versus that predicted by simulation.

The PZ36 material performed favorably in these tests, though no direct comparison was made with identical PZT-4 transducers. A single 15 mm square element at a 6.5 cm focal length (approximate f number of 3.8) was able to achieve over 4 MPa focal pressure. The major drawback was that this material proved significantly less resilient to high voltages than PZT-4, though its increased efficiency at lower applied voltages made up for that fact. An additional advantage of these elements is their low acoustic impedance, eliminating the need for an acoustic matching layer, reducing complexity in the printed housing and decreasing the difficulty in transducer assembly. It is for this reason that these elements have become a popular choice for

recent transducers, including an as-yet untested replacement for the 14-element array presented in this work.

It was hypothesized that reduced focal pressure when targeting the atrial septum in the *in vivo* porcine model was the result of either increased attenuation, or blockage of the acoustic field. This motivated the development of the 14 element transducer, to increase the packing density and active area and increase focal pressure compared to the 5 element transducer. This transducer proved more capable of creating and maintaining a bubble cloud on the atrial septum, however cumulative damage to overlying pre-focal and post focal lung tissue limited treatment times. Augmentations to the model to remove pre-focal lung tissue improved treatment times, but damage to post-focal lung tissue still resulted in poor treatment outcomes. This is a limitation of the neonatal porcine model however, and does not imply the same challenges will be present in a human. Heart orientation differences between bipedal humans and quadrupedal pigs result in different therapy access to treat the atrial septum. In humans, therapy will be applied from the subcostal acoustic window, which is free of ribs and lung. For this reason the usefulness of this model may be limited, and alternatives should be pursued.

6.5 Conclusion

An integrated, ultrasound image-guided, histotripsy therapy system was designed and constructed. This system includes a histotripsy therapy transducer specifically designed for the human neonate with congenital heart disease. The system is a necessary tool for the experiments to establish feasibility of histotripsy for pediatric cardiac applications. With it complete, the next steps toward a clinical trial for histotripsy cardiac therapy in infants can be taken.

6.6 References

[1] Z. Xu, G. Owens, D. Gordon, C. A. Cain, and A. Ludomirsky, "Noninvasive Creation of an Atrial Septal Defect by Histotripsy in a Canine Model," *Circulation,* vol. 121, pp. 742-749, February 2010.

[2] J. E. Parsons, C. A. Cain, and J. B. Fowlkes, "Cost-effective Assembly of a Basic Fiber-optic Hydrophone for measurement of High-Amplitude Therapeutic Ultrasound Fields," *Journal of the Acoustical Society of America,* vol. 119, pp. 1432-1440, March 2006.

Chapter 7
Summary and Future Work

7.1 Summary

This dissertation demonstrates the safety and effectiveness of cardiac histotripsy in a live animal model. Therapeutic creation of cardiac septal defects in necessary for the palliation of several forms of congenital heart disease and is typically performed invasively with surgical or cardiac catheterization techniques. Nine VSDs were created in 9 intact neonatal pigs with minimal collateral damage or systemic side-effects. VSD size was variable (2-6.5 mm), likely related to varying aberration of ultrasound energy from intervening bones and tissue, as well as motion and consistency of the targeted ventricular septum. Flanking injury, comparable to that seen in ASD creation in the open-chest canine model [1], was also observed and likely related to some of the same factors. These variables should be de-emphasized with an unobstructed acoustic window, such as the subcostal approach in human neonates, targeting of the thinner and less mobile atrial septum, as well as with improved transducer design allowing for motion tracking, ECG gating, and improved targeting (by decreasing focal distance and improving imaging resolution).

Six additional animals were treated noninvasively with histotripsy to create VSDs and allowed to recover for 1 month. These animals had no clinical symptoms and gained weight appropriately. In addition, ventricular systolic function was preserved, and no evidence of thromboembolic events was observed based on lung pathology and MRI of the brain. The lack of

embolic events is consistent with *in vitro* data, showing that most particles created by histotripsy-induced tissue fractionation are less than 6 μm in size (size of a red blood cell) [2]. In all, although more robust evaluation of other distal tissues is necessary before clinical advancement, the aforementioned data suggest that histotripsy cardiac therapy is safe and that effects are limited to the targeted region. Flanking hemorrhage and myocyte injury observed in the animals killed immediately after the procedure were completely resolved by 1 month, with some lesion expansion but suggesting that the unintentional damage was recoverable. However, the smallest amount of acute unintentional damage, such as the mild right ventricular free wall damage seen in two acute animals, could be devastating. This damage likely resulted from the close proximity of the free wall to the target, the bubble cloud size, and motion. Thus, innovative efforts to incorporate ultrafast motion tracking, to decrease aberration from intervening tissues (i.e., bones), and to synchronize real-time color-Doppler feedback would be useful to increase therapy accuracy further and decrease unintended injury. This work, in combination with previous data demonstrating effective creation of ASDs in an open-chest dog model suggest that non-invasive creation of both atrial and ventricular septal defects via histotripsy is potentially feasible in the human neonate.

The effects of unintended injury during histotripsy therapy of the heart could be severe, and the risk of unintended injury is increased when the target and surrounding tissue are in motion. To mitigate this potential risk, a motion correction scheme was integrated into a histotripsy system to track the motion of a cardiac target during histotripsy therapy. Results indicate that the block matching method using diamond search algorithm and Kalman filtering is capable of tracking fast motion with high accuracy. When treating a moving target *in vitro*, significant improvement in therapy accuracy and efficiency was achieved compared to therapy

without using the algorithm. Though *in vitro* testing phantoms could not produce the non-rigid motion present in the heart, feasibility was evaluated in a live beating heart *in vivo* with further work necessary to quantitatively evaluate the system performance in this setting and adapt the system for non-invasive therapy.

Real-time imaging feedback during minimally invasive or non-invasive ablation therapy is essential for ensuring efficient and thorough treatment of the target tissue. A new technique for histotripsy therapy feedback would be useful over existing techniques if it; didn't require MRI compatible hardware, was more sensitive to early stage fractionation than ultrasound backscatter reduction, and could be done without halting therapy as is required for shear-wave elastography. It was shown that histotripsy pulses generate a consistent push at the therapy focus, and characteristics of the resulting motion can be accurately estimated using standard color Doppler acquisitions. The tissue response to this push changes significantly as the tissue is fractionated by histotripsy, and these changes can be quantified by color Doppler feedback metrics that are closely related to the degree of tissue fractionation as indicated by reference metrics of tissue damage (e.g. RBC lysing and percentage of the structurally intact cell nuclei). Further analysis targeting a specific tissue and therapeutic endpoint, could refine these methods into a valuable feedback metric for cardiac or any other histotripsy therapy application.

Several histotripsy therapy transducers with appropriate physical dimensions and acoustic parameters to precisely ablate cardiac tissue non-invasively in a human neonate were developed and tested. Initial prototypes yielded minimal success in preliminary *in vivo* studies targeting the atrial septum in a neonatal porcine model, owing mainly to difficulties associated with that animal model. Additional work to augment that model, or develop a new or supplemental model is required to prove feasibility for ASD creation in a human neonate with congenital heart

disease. To aid in this process, a final prototype transducer was developed and integrated into a complete ultrasound guided histotripsy therapy system optimized for this application. This complete therapy system includes expanded Ultrasonix SonixTouch ultrasound imaging system cart with integrated histotripsy therapy amplifiers and control hardware, a macro-positioning arm with 3 axis precision micro-positioner, and an integrated therapy probe with custom telescoping phased array imaging probe and sealed ultrasound coupling chamber.

7.2 Future Work

7.2.1 *Establish Feasibility of Cardiac Histotripsy in Human Neonate*

Initial studies targeting the atrial septum in the neonatal porcine model have had little success due to the damage to pre- and post- focal lung tissue. Increased treatment times are necessary to perforate the more membranous atrial septum versus the muscular ventricular septum targeted in previous work. The lung is more sensitive to the effects of high intensity ultrasound, with the pressure threshold for damage reported to be less than 1 MPa peak negative pressure [3]. For this reason, the porcine model is sub-optimal, as the heart orientation forces an acoustic path with intervening lung tissue.

The orientation of the heart in humans is different from the orientation of the heart in pigs. In humans, that walk upright, the long axis of the heart is closer to parallel with the long axis of the body Figure 7-1A. In pigs however, that walk on all fours, the long axis of the heart is nearly perpendicular to the long axis of the body Figure 7-1B [4].

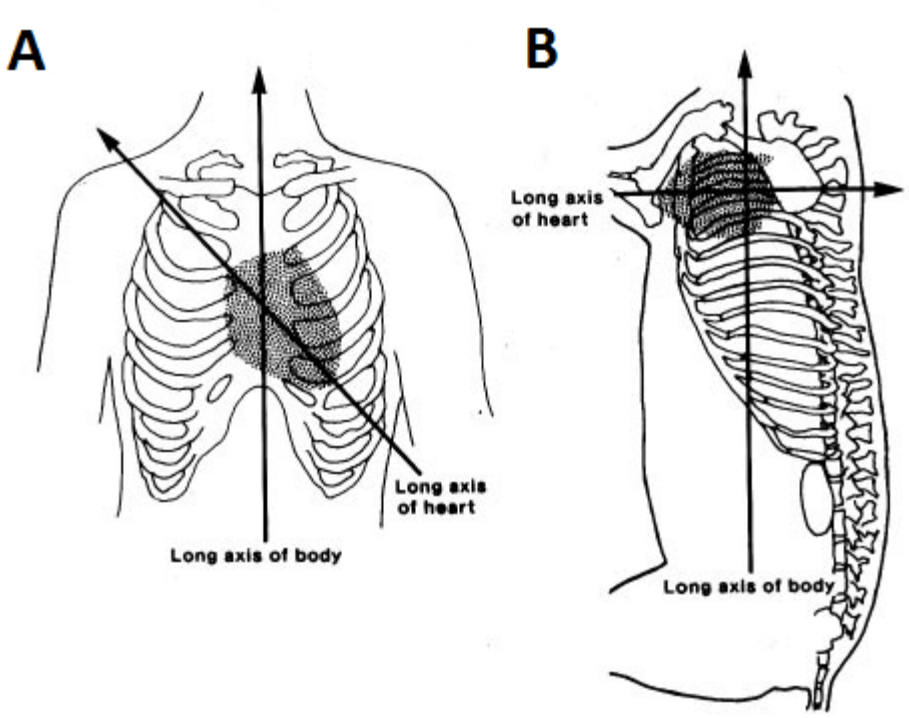

Figure 7-1: Heart orientation comparison between humans and pigs. In humans (A) the long axis of the heart is closer to parallel with the long axis of the body. In pigs however (B), the long axis of the heart is nearly perpendicular to the long axis of the body.

This orientation results in the best acoustic window to the atrial septum in the human heart being subcostal, below the ribs, aimed up into the heart through the liver. Through this window, the septum is nearly perpendicular to the ultrasound propagation, with only liver and heart in the pre-focal path (Figure 7-2A), and the aorta, esophagus, and spine in the proximal post-focal path (Figure 7-2B, [5]).

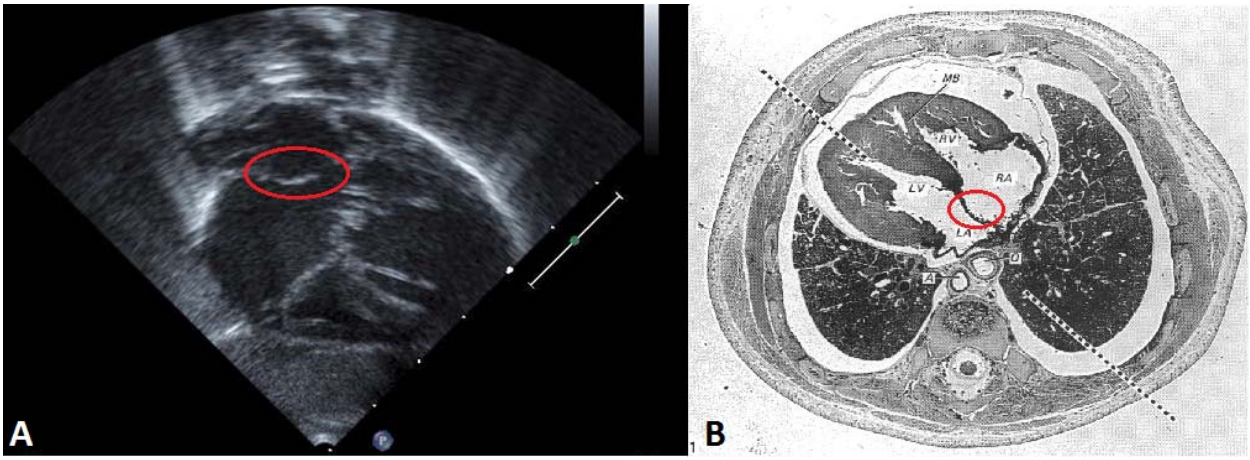

Figure 7-2: Panel A shows an ultrasound image taken in a human neonate through the subcostal with only liver and the heart in the ultrasound path to the atrial septum (circled in red), treatment would be from bottom to top. Panel B shows an image (image credit [5]) of a human newborn, with the pre- and post-focal regions of the atrial septum (circled in red) free from lung, therapy would propagate from the top to the bottom (also from below the image to above the image, since the slice is transverse).

To achieve a similar atrial septal orientation in the pig, treatment must come through a parasternal window through ribs, sternum and lungs Figure 7-3.

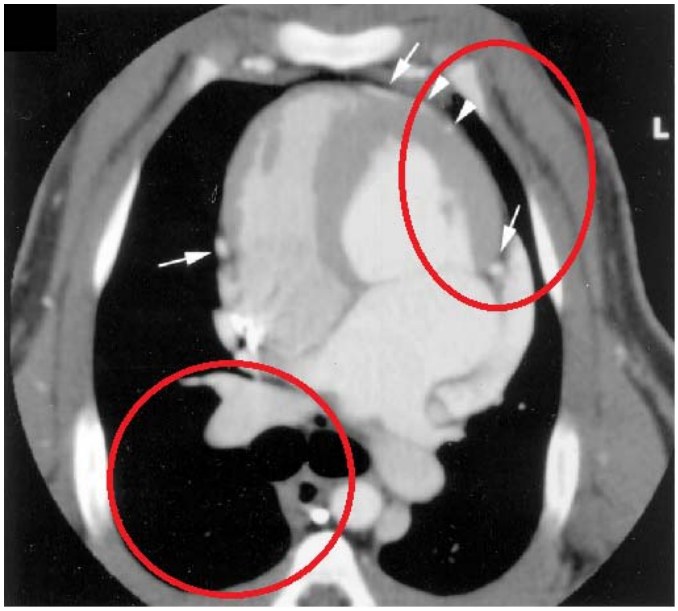

Figure 7-3: CT image of pig chest (disregard arrows, photo credit [6]), showing intervening lung in the pre-focal therapy field (circled in red, top right) and post-focal field (circled in red, bottom left). Therapy through the parasternal window would be applied from top right to bottom left.

Based on these results, the best route for proof of feasibility is to combine the results of testing in an augmented version of this model with *in vitro* testing in a human phantom. Augmentations to this model may include: the introduction of an artificial pleural effusion to displace overlying lung from the acoustic field, surgical removal of overlying ribs and lung tissue, and surgical implantation of a sound absorbing material to shield post-focal lung from ultrasound injury.

Since direct action will be necessary to spare lung damage in this animal model, it must be shown that those steps will not be necessary in the human neonate. To prove this, we plan to construct a model human neonate phantom. This model will be based on 3D reconstruction of the anatomy of the human neonate from MRI and CT datasets. From these datasets, thresholds can be assigned and different tissues segmented from others. A preliminary 3D reconstruction of the ribs (yellow), lungs (green), and heart (purple) is shown in Figure 7-4.

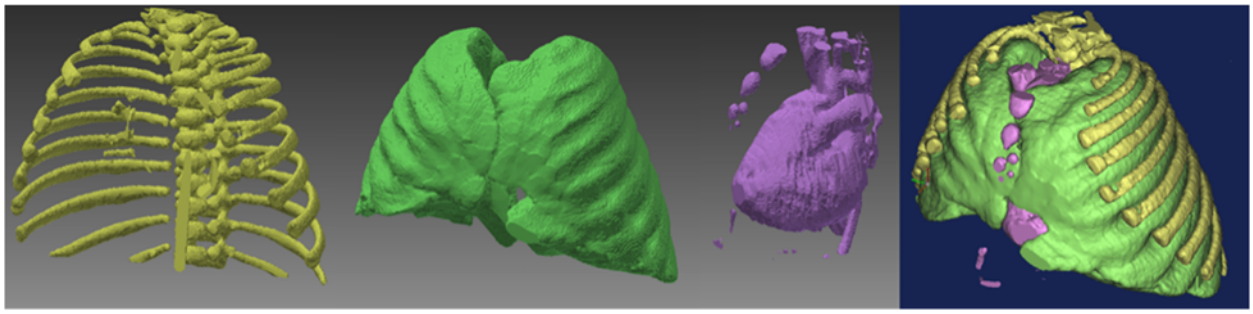

Figure 7-4: 3D reconstruction of the ribs (yellow), lungs (green), and heart (purple) of the human neonate from MRI and CT datasets.

Appropriate materials for each of these tissue types will need to be determined and the phantom constructed. 3D printing is a likely candidate for the ribs, to form the complex shape and strength of the ribs. Materials commonly used for commercial ultrasound imaging phantoms should be useful to mimic overlying tissue like skin, liver and muscle. A damage indicating phantom as sensitive to ultrasound damage as lung will need to be developed as well, to ensure that

histotripsy will not damage the lungs in the human neonate. A reusable cartridge to house excised porcine or human atrial septum tissue or phantom at the position of the atrial septum in the phantom will also be required.

7.2.2 Motion Tracking Extensions

Chapter 4 demonstrates the improvements in accuracy and efficiency with the addition of axial motion correction in histotripsy therapy. These methods are not limited to 1D motion however, as the algorithm actually already tracks the 2D motion of the target object in the ultrasound imaging plane. Since the therapy transducer was only capable of steering along the therapy axis and it could be aligned with the intended target *in vivo* such that the only significant motion was along that axis, only that component of motion was corrected for in that work. Should another application require it, extension to 2D motion correction is straightforward with the use of a 2D phased array therapy transducer, and should be evaluated.

Similarly, should full 3D motion correction be necessary, the extension of the techniques presented in this work to 3D is also possible. The first step in extending the current system to 3D is to adapt or acquire a 3D ultrasound imaging probe for use on the Ultrasonix SonixTouch imaging system. Several 3D imaging probes are compatible with this system, and should be evaluated for use in the desired application. With 3D image data available, the next step is to extend the motion tracking algorithm for 3D motion tracking. Extension of the key principles of our algorithm from the current 2D system to 3D motion tracking is straightforward. With ultrasound 3D volume data and a reference volume image of the target, a 3D block matching procedure would be very similar to the current 2D methods. The SAD metric, diamond search procedure, and Kalman filter all extend naturally for use on 3 dimensional data. Extending our

current 2D motion tracking algorithm to 3D necessitates faster 3D data collection than available with conventional 3D imaging transducers however, so as an alternative, two 2D images in orthogonal planes may be used to estimate 3D motion at a faster speed. In this case, extension would be much more straight-forward, since parallel implementations of the current algorithm could be run simultaneously on the two image planes with an additional weighted average between the redundant estimations of the axial component of motion from each image plane. In either case, increased computational complexity could potentially reduce frame rates. To combat this, processing hardware upgrades and computation parallelization should be explored to potentially offset these additional computation requirements.

7.2.3 Investigation into the Mechanism of Bubble-induced Color Doppler Feedback

The color Doppler feedback methods presented in Chapter 5 rely on bubble-induced motion after each histotripsy pulse at the therapy focus along the axis of propagation. The source of this motion is not fully understood at this time, though the experiments demonstrate that the phenomenon is consistent and reproducible. Several potential mechanisms have been identified, and should be fully investigated.

Acoustic radiation force is a tempting choice for the mechanism behind the type of push-rebound motions observed in this study, however the extremely short pulses (< 2 cycles) are not sufficient to generate the observed motion simply through absorption alone. Moreover, preliminary experiments using particle image velocimetry (PIV) of embedded 10 micron glass beads show no measurable focal velocity at slightly sub-cavitation threshold pulses (~28.7 MPa peak negative pressure) with large velocities comparable to those observed in this study for supra-threshold pulses (~38.6 MPa peak negative pressure).

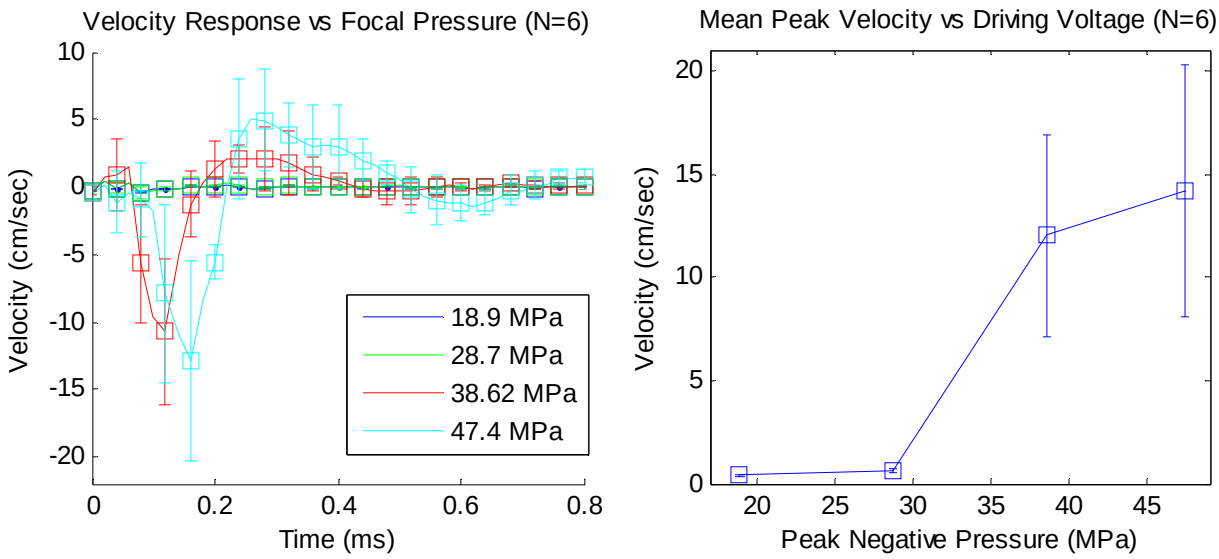

Figure 7-5: Velocity response measured using PIV for 4 peak negative focal pressures (left panel), and the mean peak velocity versus peak negative pressure from those measurements (right panel).

This does not completely eliminate acoustic radiation force however, as the presence of forming cavitation bubbles could greatly enhance the radiation force via reflection of subsequent acoustic energy. The effects of the acoustic energy after the primary negative half-cycle could be potentially isolated using frequency compounding techniques [7]. Using this transducer, a single cycle pressure waveform can be generated at the transducer focus with either the positive half-cycle after the negative half-cycle (Figure 7-6 left panel), or the positive half-cycle before the negative half-cycle (Figure 7-6 right panel). Comparing the resulting push velocity between the two scenarios should clarify the role of acoustic radiation force in generating this motion.

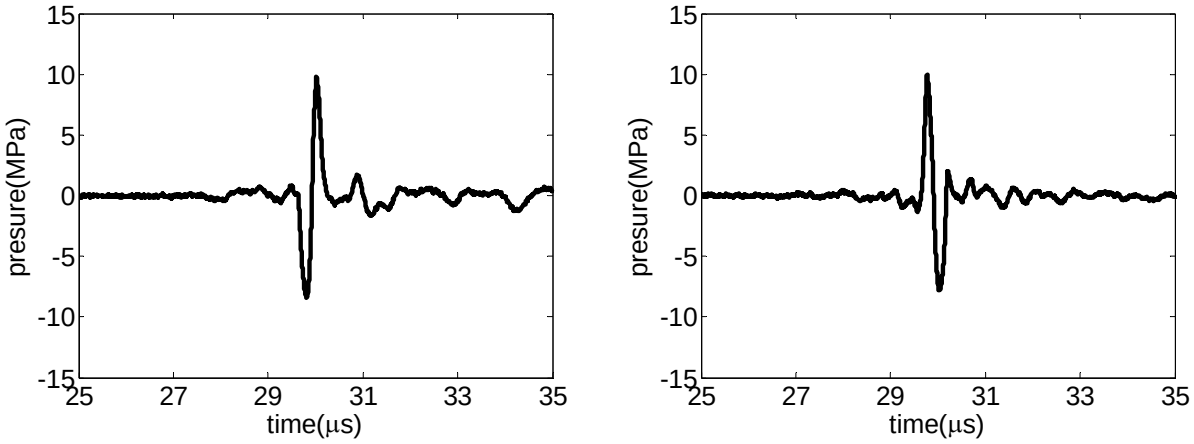

Figure 7-6: Synthesized pressure waveforms from the frequency compounding transducer with the positive half cycle after the negative half-cycle (left panel), or the positive half-cycle before the negative half-cycle (right panel).

Another potential mechanism is asymmetric expansion of the bubbles during the formation of the bubble cloud. Preliminary studies using ultra high speed imaging (5 MHz, 200 ns between frames) have shown that as the individual bubbles form, they grow more along the direction of propagation than back toward the therapy transducer. This is equivalent to a bubble moving through the medium, and thereby exerts a net forward force on the medium. Figure 7-7 shows a series of 16 images of a single bubble taken immediately following the arrival of the histotripsy pulse at the focus (therapy pulse traveled from top to bottom). This is most obvious in frames 2-5, were the bubble has clearly translated along the path of therapy propagation at very high speed (> 50 m/s).

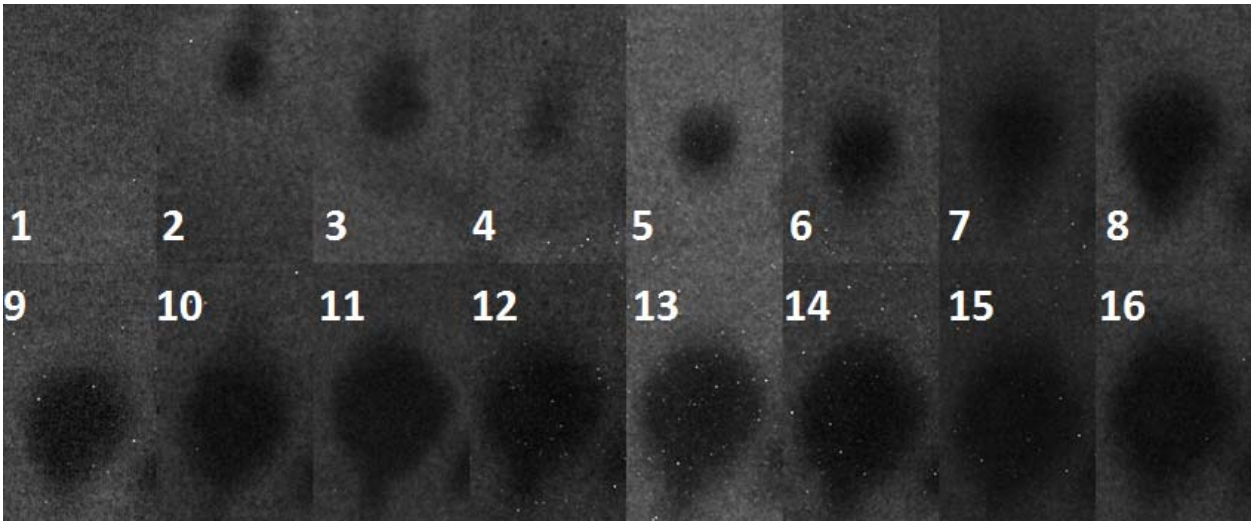

Figure 7-7: Ultra high speed images of a histotripsy bubble growth. These 16 images were acquired with 200 ns inter-frame delay (5 MHz) with 5 ns exposures. The spatial resolution is 0.85 micron/pixel.

The velocity of single bubbles in these images was computed by the change in position of the centroid, proximal and distal sides of bubbles from frame to frame divided by the inter-frame time. The average velocities of the centroid of the bubbles (left) and the proximal and distal sides of the bubbles (right) are shown in Figure 7-8. From the average velocity of the centroids, the bubbles appear to move rapidly away from the therapy, followed by damped rebound oscillations. From the plots of the velocity of the proximal and distal sides of the bubbles, the motion is more complicated. At the first time point, the distal side is moving rapidly away while the proximal side as nearly zero velocity. This is consistent with a bubble growing only forward. At the second time point, the distal side of the bubble is moving away from the therapy, but now the proximal side is moving away faster. This is consistent with a bubble shrinking in radius as it moves forward. For the next 2 time points, the distal side moves away and the proximal side has nearly zero velocity, consistent with the bubble growing forward again. Beyond this, there is

alternating shrinking and growing of the bubble on top of the average oscillatory motion of the bubble observed in the centroid motion plot.

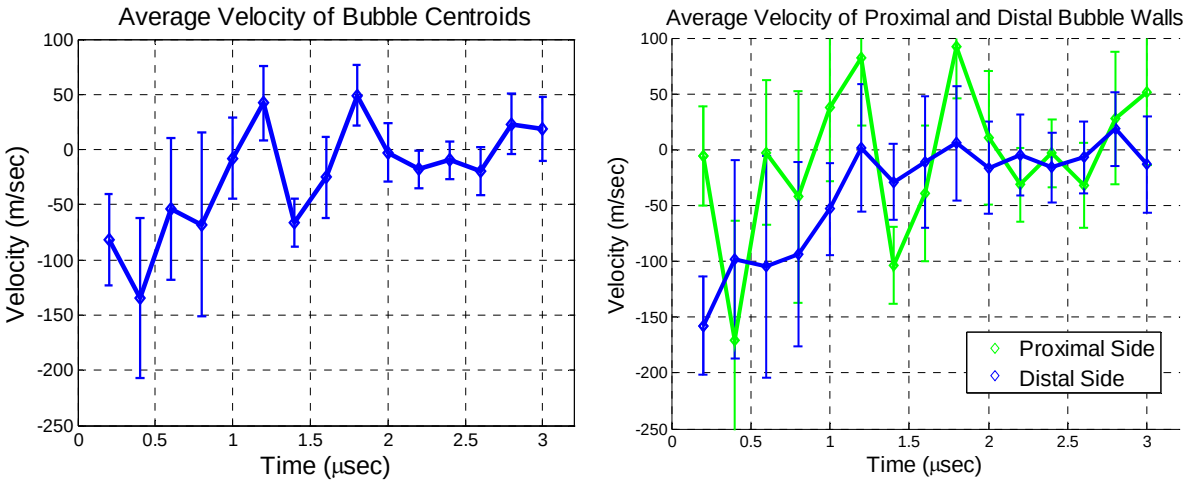

Figure 7-8: Average frame to frame velocity of the proximal and distal sides of the histotripsy bubbles. Negative velocity is down in the images, along the direction of therapy propagation.

The cumulative effect of this impulse-like push on all the bubbles could generate the motion observed in the color Doppler study. Additional work is necessary however, to link this motion during cloud formation to the motion detected after cloud collapse.

The violent collapse of the histotripsy bubble cloud is another potential mechanism that could generate the observed motion. The bubble cloud collapse certainly generates significant motion in the focal region, and this was observed in this study. This motion appeared inconsistent from pulse to pulse however, and is unlikely to cause the consistent and predictable push and rebound motion along the axial direction of the transducer. An experiment to test this decisively will need to be designed to be sure however. Some combination of these mechanisms is also possible, and a comprehensive study should be designed, based on these preliminary results to fully elucidate the mechanism behind this observed motion.

7.3 References

[1] Z. Xu, G. Owens, D. Gordon, C. A. Cain, and A. Ludomirsky, "Noninvasive Creation of an Atrial Septal Defect by Histotripsy in a Canine Model," *Circulation,* vol. 121, pp. 742-749, February 2010.

[2] Z. Xu, Z. Fan, T. L. Hall, F. Winterroth, J. B. Fowlkes, and C. A. Cain, "Size Measurement of Tissue Debris Particles Generated from Pulsed Ultrasound Cavitational Therapy – Histotripsy," *Ultrasound in Medicine & Biology,* vol. 35, pp. 245-255, 2009.

[3] S. Z. Child, C. L. Hartman, L. A. Schery, and E. L. Carstensen, "Lung damage from exposure to pulsed ultrasound," *Ultrasound in Medicine & Biology,* vol. 16, pp. 817-825, 1990.

[4] S. J. Crick, M. N. Sheppard, S. Y. Ho, L. Gebstein, and R. H. Anderson, "Anatomy of the pig heart: comparisons with normal human cardiac structure," *J Anat,* vol. 193 (Pt 1), pp. 105-19, Jul 1998.

[5] R. Walmsley and W. S. Monkhouse, "The heart of the newborn child: an anatomical study based upon transverse serial sections," *J Anat,* vol. 159, pp. 93-111, Aug 1988.

[6] A. Lembcke, T. H. Wiese, J. Schnorr, S. Wagner, J. Mews, T. J. Kroencke, C. N. Enzweiler, B. Hamm, and M. Taupitz, "Image quality of noninvasive coronary angiography using multislice spiral computed tomography and electron-beam computed tomography: intraindividual comparison in an animal model," *Invest Radiol,* vol. 39, pp. 357-64, Jun 2004.

[7] K.-W. Lin, T. L. Hall, R. J. McGough, Z. Xu, and C. A. Cain, "Synthesis of Monopolar Ultrasound Pulses for Therapy: The Frequency-Compounding Transducer," *IEEE Trans Ultrason Ferroelectr Freq Control,* accepted Jan. 2014.